THERMO-MECHANICAL FATIGUE INVESTIGATIONS ON NICKEL BASE SUPERALLOYS AND CREEP OF NIAL THIN FILMS

Ronny Mai

A dissertation submitted for the degree of Doctor of Philosophy

Heriot-Watt University

School of Engineering and Physical Sciences

June 2011

The copyright in this thesis is owned by the author. Any quotation from the thesis or use of any of the information contained in it must acknowledge this thesis as the source of the quotation or information.

Abstract

Supervisors: Dr. R.L. Reuben, Dr.-Ing. J. Hammer

In service, many components and structures of aero jet engines, are exposed to a complex superposition of varying mechanically and thermally induced forces. This cyclic loading is most pronounced during the start-up and the shut-down sequence of the engine, usually combined with high temperature transients, and is responsible for a serious reduction in lifetime, compared to isothermal operating conditions. A detailed knowledge of this interaction between varying temperatures and loads is of considerable importance for precise lifetime calculations. In order to characterise and scientifically describe the material behaviour under thermo-mechanical fatigue (TMF) exposure, laboratory experiments are performed under strictly defined conditions. The main challenge for experimental investigations is the precise temperature control required to simulate the fast thermal transients under operating conditions.

In any component, the lifetime behaviour is dominated by three different damage mechanisms: fatigue, oxidation and creep. In order to protect the component surface against oxidising atmosphere in gas turbines the substrate material is coated with different protective coating systems.

This work compares the thermal mechanical fatigue behaviour of two different substrate materials, Nimonic 90 as the "classic" matrix and PM 1000, an oxide dispersoide strengthened powder metallurgical superalloy under TMF loadings. Additionally, the creep behaviour and the lifetime analysis of a $\beta-$nickel aluminide diffusion coating system is described.

to

my family

ACADEMIC REGISTRY
Research Thesis Submission

Name:	Ronny Mai		
School/PGI:	Heriot Watt University, School of Engineering and Physical Sciences		
Version: *(i.e. First, Resubmission, Final)*	Final	Degree Sought (Award **and** Subject area)	PhD

Declaration

In accordance with the appropriate regulations I hereby submit my thesis and I declare that:

1) the thesis embodies the results of my own work and has been composed by myself
2) where appropriate, I have made acknowledgement of the work of others and have made reference to work carried out in collaboration with other persons
3) the thesis is the correct version of the thesis for submission and is the same version as any electronic versions submitted*.
4) my thesis for the award referred to, deposited in the Heriot-Watt University Library, should be made available for loan or photocopying and be available via the Institutional Repository, subject to such conditions as the Librarian may require
5) I understand that as a student of the University I am required to abide by the Regulations of the University and to conform to its discipline.

* *Please note that it is the responsibility of the candidate to ensure that the correct version of the thesis is submitted.*

Signature of Candidate:		Date:	10/10/2011

Submission

Submitted By *(name in capitals):*	
Signature of Individual Submitting:	
Date Submitted:	

For Completion in the Student Service Centre (SSC)

Received in the SSC by *(name in capitals):*			
Method of Submission *(Handed in to SSC; posted through internal/ external mail):*			
E-thesis Submitted ***(mandatory for final theses)***			
Signature:		Date:	

Please note this form should bound into the submitted thesis.

Updated February 2008, November 2008, February 2009, January 2011

Contents

List of Tables

List of Figures

Glossary

α	Thermal elongation coefficient (m/K)
$\dot{\varepsilon}_s$	Steady creep rate (1/s)
σ	Stress (MPa)
σ_{eff}	Effective stress (MPa)
ε	Strain (mm/mm)
ε_{el}	Elastic strain (mm/mm)
ε_m	Mechanical strain (mm/mm)
ε_{pl}	Plastic strain (mm/mm)
ε_{th}	Thermal strain (mm/mm)
ε_{tot}	Total strain (mm/mm)
ΔT	Temperature difference (K)
A_0	Cross section area (m^2)
BC	Bond coat
bcc	Body-centred cubic

BSE	Backscattered electron detector
CC	Conventional cast
CCD	Counter-clockwise diamond cycle
CD	Clockwise diamond cycle
CoP	Code of practise project
CVD	Chemical vapour deposition
DAQ	Data acquisition
DBTT	Ductile-brittle transition temperature
E	Young's modulus (GPa)
EDS	Energy dispersive X-ray spectroscopy
F	Force (N)
f	Frequency (Hz)
fcc	Face-centred cubic
GUI	Graphical user interface
HCF	High cycle fatigue
HF	High frequency
I	Current (A)
IF	Isothermal fatigue
IP	In-phase cycling
L_0	Original length at room temperature of the parallel portion of the specimen ($L_0 > l_0$) gauge length (mm)

l_0	Gauge length (mm)
LCF	Low cycle fatigue
LVDT	Linear Variable Differential Transformer
N	Cycle number
N_f	Cycles to failure (TMF Life)
ODS	Oxide dispersoide strengthened
OP	Out-of-phase cycle
PM	Powder metallurgy
PVD	Physical vapour deposition
Q	Activation energy
R	Gas constant
R_ε	Strain ratio between minimum and maximum strain
R_z	Surface roughness
SC	Single crystal
SE	Secondary electron detector
SEM	Scanning electron microscope
SN	Stress-number curve
T	Temperature (°C)
T_m	Melting temperature (°C)
t_m	Rupture time (h)
TEM	Transmission electron microscope

TGO	Thermally grown oxide
U	Voltage (V)

1. Introduction

1.1. High Temperature Alloys

During the past 50 years, the continuous demand for higher performance and improved efficiency in terms of reduced fuel consumption of power-producing gas turbines and aircraft engines has involved an increase in operating temperatures and mechanical loading conditions, respectively. Any optimisations of the operating performance and efficiency of gas turbines have been, up to now, directly related to the development and availability of appropriate high temperature materials, figure 1.1.

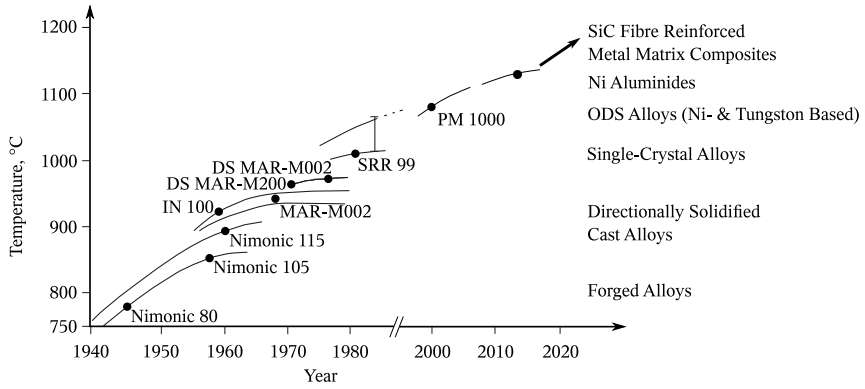

Figure 1.1: High temperature material development during the past 50 years. The points mark the industrial introduction. Recharged on the basis of Hammer [1].

Thus, most technological efforts are still focused on the high temperature capability of these alloys in terms of high temperature mechanical properties and oxidation resistance. The severest conditions in a turbine are encountered in the first turbine stage guide vanes and rotating blades immediately after the combustion chamber. The material of these sections has to resist three different "load" types: mechanical, thermal and oxidative. The annual increase of 4 K in operation temperature has only been possible during

the past five decades by the consequent development of high temperature super alloys and protective coating systems, respectively. Nimonic 75 [2–5] is the basis for all of these developments. This single-phase material has been constantly modified, e.g. by precipitation hardening with a second, coherent phase and later on as complete single crystal structure. Intermetallic alloys or metal-matrix-composites to increase the operating temperatures are not realisable technologically in the near future.

A secondary objective has been the development of thin thermal barrier and diffusion coatings. Commonly used thermal barrier systems are double layer systems with a corrosion and bond coating (BC) as well as a ceramic thermal barrier coating (TBC). The bond coatings act as an oxidation protector and a binder between the ceramic TBC and the substrate material.

Mechanical loads, usually caused by centrifugal forces due to the high rotational speed of internal components, are typically superimposed by monotonic bending forces due to the mass flow out of the combustion chamber. Furthermore, creep damage also occur depending on the operating temperature range. Due to the fact that most mechanical loadings are in the high temperature range, the material has to bear immense total stresses during temperature changes, especially during start-up and shut-down cycling, which lead to rapid thermal transients. Both loading types are combined in *Thermal Mechanical Fatigue*, which represents the most common loading type for hardest-worked turbine blades in the hot gas section.

In order to design turbine blades for these environmental conditions, reliable material property data are required. The improvement of the acquisition of these data as well as their reliability under laboratory conditions has led to the new ISO Standard for strain-controlled Thermal-Mechanical Fatigue (TMF) testing, which is currently in preparation and should solve the non-reproducibility and the lack of comparability of future TMF test data [6].

1.2. Focus of this Work

In many cases, critical component volumes, subjected to thermally-induced strains, have been designed based on results of uniaxial isothermal low cycle fatigue tests. These experiments have been carried out on the expected maximum operating temperature. The idea has been to the simulate the material's "worst case" conditions, resulting in a conservative estimate of fatigue life. However, these tests do not represent the damage mechanisms during transient thermal and mechanical loading and their superposition. Due to the requirement for high-quality material data and improved reliability a new type of test equipment has to be designed and realised. To simulate real working conditions accurate thermal measurement and control as well as precise strain control test facilities are required to ensure that standardisation of the method is possible.

The literature reports on the lifetime behaviour of precipitation hardened nickel base superalloys indicate that coherent particles will reorganise under different stresses, resulting in an unstable microstructure. This reorganisation reduces the precipitates' resistance to being cut by dislocations leading to a decreased hardening effect during the lifetime. In order to avoid the complication of changing material properties with time, and also in order to follow the moste recent material developments, this study deals with two different nickel based superalloys. Nimonic 90 has been chosen for the TMF investigation of the pure matrix material. Due to the fact that this material is well investigated in the literature it was used in this work as a benchmark test. As a more highly developed material PM 1000 has been chosen as an oxide dispersoid strengthened alloy, which is thermally very stable and does not rely on interactions between the oxides and dislocations. The characteristic phase shift of $\varphi = -135^\circ$ between cycling of temperature and mechanical strain, was used to simulate the operating conditions during start-up and shutdown. The TMF lifetime behaviour under near service conditions was determined for both materials, and results compared with those reported in the literature using "worst case" simulations.

Under real operating conditions the complete blade/coating system is exposed to the aforementioned high loadings. Creep has been identified as one of the important

damaging factors in such a system. Hence, a separate study of the intermetallic binder material Ni_3Al as thin film specimens has also been carried out using the equipment developed for the main study.

The separate investigation of TMF lifetime of the blade material and creep behaviour of its diffusion coating leads to a better understanding of the different damage mechanisms. This work therefore divides the complexity of the lifetime behaviour of coated TMF-life specimens into two thermally influenced mechanisms, the TMF-behaviour of two different substrate materials and the creep behaviour of a typical diffusion coating. In phenomenological terms, the creep lifetime of the pure coating limits the time for crack initiation for the substrate-coating system, whereas the uncoated substrate material is usually limited by TMF cycling.

Summarising, the work focusses on thermal mechanical fatigue investigations of two different nickel base superalloys with very different microstructural arrangements and also creep of the binder part of a thermal barrier coating. The main contribution to knowledge is the effect that testing under near-service conditions has on the appeared creep and TMF properties and hence the implications for the hot-end turbine design.

2. Literature Review

This review covers three main aspects of the engineering science relevant to the design of components for the hot-end turbine applications, namely service loadings, alloy developments and coating development.

2.1. Loadings under Service Conditions

The term "service loadings" is here interpreted as the variables (time, temperature and stress) which give rise to the main life-limiting damage phenomena. These phenomena, in order of presentation are: low cycle fatigue, thermal mechanical fatigue, creep and oxidation.

2.1.1. Low Cycle Fatigue

Besides the aforementioned three main loadings (fatigue, creep and oxidation), jet engine rotors face a number of other life-limiting criteria, such as vibrations and bearing wear, which can lead to complete component failure due to strain-based modification of the thermal loadings. One of the central issues is the failure due to low cycle fatigue, commonly referred as LCF, relevant for structures and subjected to a small number of load cycles in their economic life [7]. On a macroscopic scale a contribution to damage occurs in every cycle due to plastic deformation and a characteristic of LCF is the the existence of stresses above the yield stress elsewhere than at the crack tip. In contrast to the stress based life time approach of Basquin the nature of the loading is described as cyclic strain

rather than cyclic stress as thermal stresses are enforced by thermal expansion differences at the elevated temperatures [8].

Usually all rotating components have an idle (low centrifugal stresses) and an operating speed (high centrifugal stresses), alternating between the two. Impurities or pores in the material volume and inevitable design stress concentrations can be identified as indicators for LCF failures. An LCF cycle represents one shift from low to high speed and return.

A chronological mechanism of fatigue damage has been described by Mughrabi [9]. His main concept is a differentiation between cyclic deformation and the resulting fatigue damage, figure 2.1. Cyclic plastic deformations are attributed to dislocation mechanisms and include hardening/softening effects as well as saturation. The final strain localisation is a change-over from dislocation mechanisms to damage mechanisms, continuing with crack initiation and accelerated crack growth.

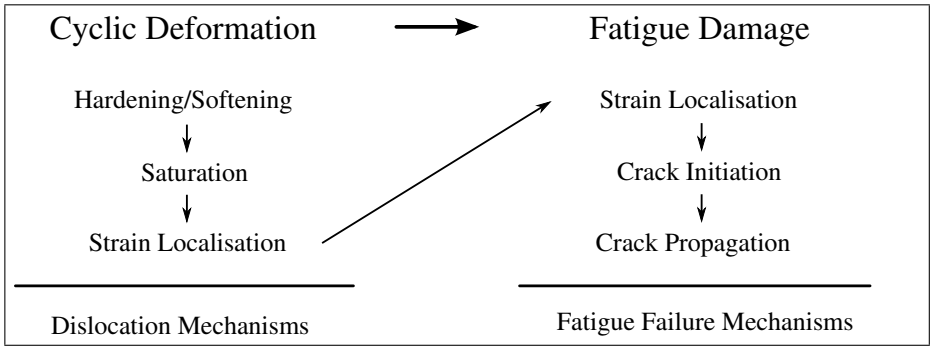

Figure 2.1: Main stages of cyclic deformation and fatigue damage, according to Mughrabi [9].

The classification of figure 2.1 provides a mechanistic schedule for "global" events (cyclic deformation and fatigue damage) in the whole material structure during the low-cycle fatigue life. Summarising, fatigue occurs as a result of cyclic loading and is a process of strain accumulation, localisation, crack initiation and growth.

The damage parameters for any kind of fatigue test have been categorised by Christ [10] as follows:

- Material conditions (grain size, texture, precipitates, ...)

- Loading conditions (load cycle shape, mean load, frequency, ...)
- Manufacturing conditions (surface quality, residual stresses, ...)
- Environmental conditions (air, vacuum, corrosive media, temperature, ...)

In general, all assessments of life time should be considered with respect to possible differences between experimental conditions and material related influences and those in the actual design. To simulate LCF cycles under laboratory conditions strain controlled tests are typically performed using the parameter R_ε:

$$R_\varepsilon = \frac{\varepsilon_{m,\,min}}{\varepsilon_{m,\,max}} = -1 \tag{2.1}$$

i.e. with a mean strain of zero.

Generally, the cyclic deformation process is divided into a transient regime, characterised by cyclic softening/hardening during the first few load cycles, in the literature [11–13] followed by cyclic saturation with a stabilised structural response to each applied loading cycle. In general, the final failure concentrates on areas of high plastic deformation and therefore high localised cracks. S-N (Woehler) curves are traditionally used to analyse the fatigue lifetimes, based on the relation between the applied stress amplitude ($\sigma/2$) and the number of cycles to failure (N_f) first identified by Basquin [14]. Fatigue properties can therefore be quantified using equation 2.2 with the parameters, σ_f, the Basquin strength coefficient and B the Basquin exponent.

$$\frac{\Delta\sigma}{2} = \sigma_f \left(2N_f\right)^B \tag{2.2}$$

σ_f ... Fatigue strength coefficient
B ... Basquin exponent

For the description and prediction of the lifetime behaviour under the strain controlled testing conditions more typical for the low-cycle fatigue, Manson [15] and Coffin

[16] established a relationship (2.3) between the applied plastic strain amplitude ($\Delta\varepsilon_{pl}/2$) and the cycles to failure (N_f) for a defined temperature, where ε_f represents the fatigue ductility coefficient. The parameter C, commonly known as the "Coffin" lifetime exponent, stands for a material property which indicates the slope in the double logarithmic plot of $log\ \Delta\varepsilon/2$ versus the cycles to failure $log\ N_f$, figure 2.2.

$$\frac{\Delta\varepsilon_{pl}}{2} = \varepsilon_f (N_f)^C \tag{2.3}$$

ε_f ... Fatigue ductility coefficient
C ... Fatigue ductility exponent

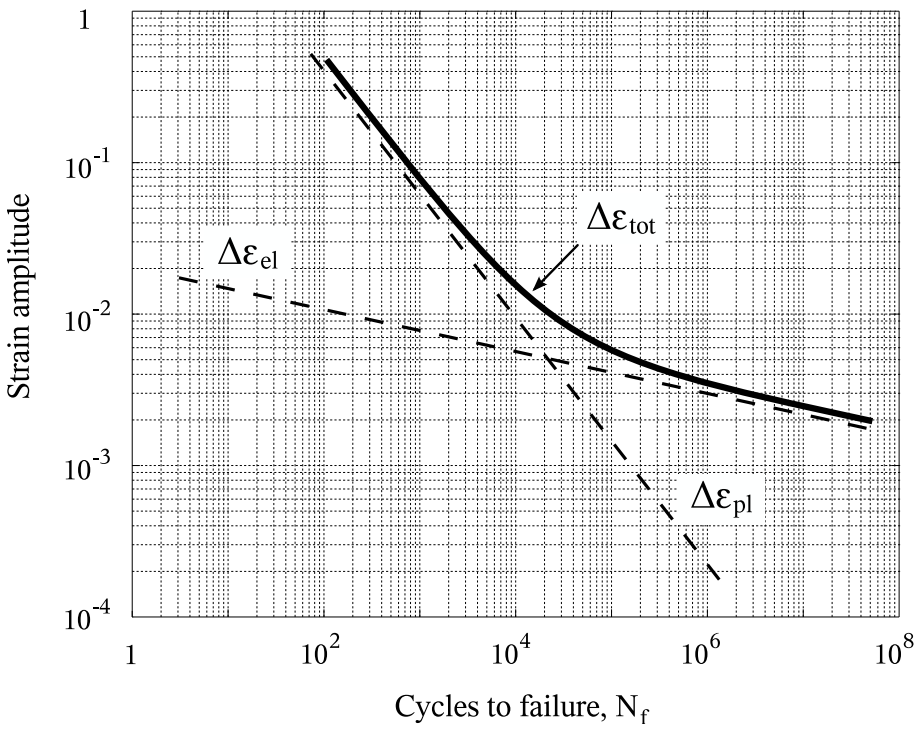

Figure 2.2: The strain based lifetime diagram shows the superposition of the plastic and the elastic strain amplitudes.

Figure 2.2 additionally illustrates one of the key differences between low-cycle and high-cycle fatigue, which is that low-cycle fatigue is characterised by strain amplitudes that are predominantly plastic. Based on these principles, to interpret cyclic life time and

plastic deformation, strain controlled tests have to be supplemented by an additional damage factor, the temperature. The superimposed thermal strains corresponding to particular operating temperatures can be realised in isothermal fatigue (IF) tests, and many different investigations have been carried under these testing conditions [17–19]. The more complex thermal cycling, associated with start-up and shutdowns and fluctuations in operating conditions, as well as the mechanical LCF, leads to the special case of thermal mechanical fatigue which is considered as more realistic for technical applications [20–24].

2.1.2. Thermal Mechanical Fatigue

Due to the small numbers of on/off cycles in the design life of an aircraft engine and the resulting significant thermal stresses, LCF tests should usually be considered. Unlike the vast majority of isothermal fatigue tests, figure 2.4a, TMF investigations focus on controlled thermal and mechanical cycling, figures 2.4b to 2.4f. The general strain relation, the superposition of thermal and mechanical loadings is symbolised by equation 2.4.

$$\varepsilon_{tot} = \varepsilon_{th} + \varepsilon_{m} \tag{2.4}$$

The error in temperature measurement during the cycle induces high additional stresses, particularly at the peak temperatures, and this system is designed to reduce these deviations to a minumum. Kühn et al. [26] limited the technically feasible temperature deviation to $\pm 5\,\mathrm{K}$ for temperature transients of $5\,\mathrm{K/s}$. They investigated both types of thermal strain compensation, namely *time-based* and *temperature-based*. Time based thermal strain compensation leads to a system whose response is very sensitive to nominal temperature errors. Another reason why this type of system is not preferred for accurate TMF investigations is the additional mechanical strain amplitude error. This has a large influence on the cyclic deformation behaviour and, ultimately, on the lifetime. Furthermore, Kühn et al. [26] pointed out that temperature based thermal strain compensation is the better system type to ensure no additional strain error. They conclude that a temperature deviation of $\pm 20\,\mathrm{K}$ is acceptable for these types of systems under TMF conditions. Both types of

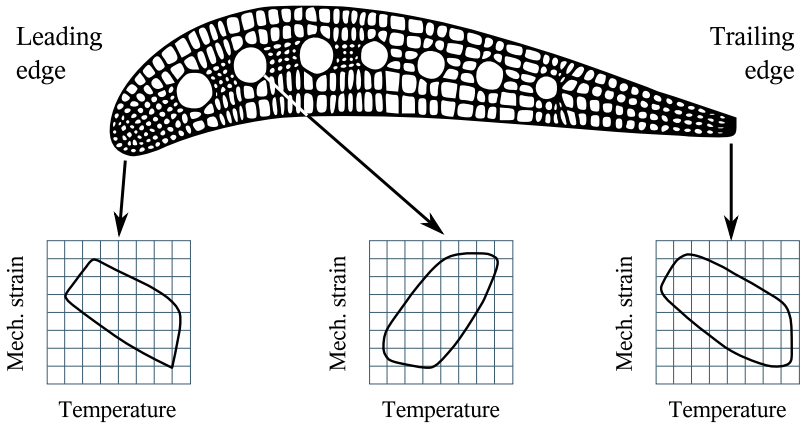

Figure 2.3: Typical TMF load cycles of a turbine blade; The phase shift of $\varphi \approx$-135° is just observable for leading and trailing edge, where cracks are typically initiated. The volume loading leads to a completely different cyclic behaviour. Re-drawn with kind permission of Affeldt [25].

thermal strain compensation were implemented in the TMF-Standard project [2, 27–30], but no suggestion for the type of compensation was given. Based on this information, it was decided that this work should focus on the minimisation of additional applied strains during TMF cycling. Further details are explained in section 4.1ff and the exact datum to which this work can be measured is the *Zero-Stress-Test*, described in section 4.2.1.

The decoupling of the temperature and applied mechanical strains with a phase shift φ between both variables make these kinds of test extremely versatile. However, it should be considered that this additional degree of freedom generates an enormous number of potential test combinations, whilst only a limited number of combinations are useful for experimental approaches [2, 27–29, 31–34]. Thermal strains in the heated outer walls are constrained by the cold inner material resulting in compressive stresses. The laboratory simulation for this kind of TMF damage is the out-of phase (OP) TMF ($\varphi = 180\,^\circ$) cycling. Equilibrium of stresses results in tensile loadings of the cold inner material. This situation is simulated by in-phase (IP) TMF ($\varphi = 0^\circ$ characterised by maximum mechanical strain coinciding with maximum temperature. Other cycling types, e.g. with a phase shift of $\varphi = \pm 90^\circ$, known as the clockwise diamond (CD) or the counter-clockwise diamond (CCD) type, figures 2.4e, 2.4d are in between these limits. The importance of this phase shift was first indicated by Skelton [35]. The most heavily stressed regions, and

hence crack initiation zones, of a turbine blade are typically the leading and trailing edges during start-up and shutdown. Therefore it is important to perform TMF tests for in-phase and out-of-phase cycling to measure the material lifetime limitations and the phase shift ($\varphi = -135°$), represents a realistic stress situation for a blade during such high temperature transients [5, 11, 27, 36]. For this study, a phase shift of $\varphi = -135°$ (Figures 2.3 and 2.4f) was therefore applied in addition to the IP cycling according parameters defined in the literature [2, 18, 21, 37, 38].

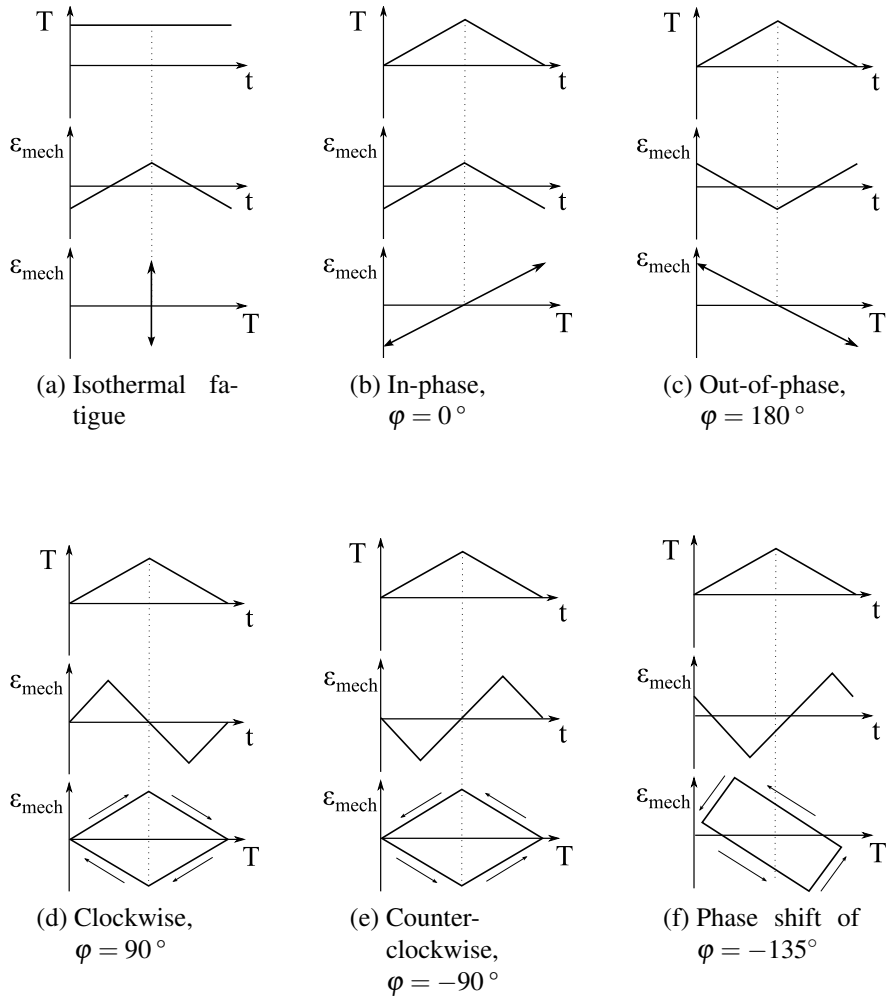

(a) Isothermal fatigue

(b) In-phase, $\varphi = 0\,°$

(c) Out-of-phase, $\varphi = 180\,°$

(d) Clockwise, $\varphi = 90\,°$

(e) Counter-clockwise, $\varphi = -90\,°$

(f) Phase shift of $\varphi = -135°$

Figure 2.4: Special cases of phase shifts in TMF experiments.

The literature indicates a lifetime reduction on TMF tests versus isothermal fatigue tests [18, 34, 35, 39–46]. An initial requirement for similar lifetimes is that the maximum TMF temperature corresponds with hold temperature of the isothermal test. Even

than, a valid life time prediction based on isothermal tests is only possible for similar microstructural behaviour and damage mechanisms between both test types [47]. For example, Nickel based superalloys have distinct isothermal high and low temperature fatigue mechanisms. Under TMF conditions such alloys exhibit a combination of both and this effect may be enhanced by fast applied temperature cycling.

In the case of isothermal fatigue of nickel-based superalloys at lower temperatures, the deformation behaviour mainly consists of plenary slip in the matrix and the cutting of γ' particles. At higher temperatures, the behaviour changes to a transverse glide and climb of dislocations and the formation of dislocation network areas at the γ - γ' interfaces. The crack formation behaviour is also distinctive. At lower temperatures, crack formation starts on surface defects, such as pores or striations, which usually result in high local stresses. At higher temperatures, oxidised surface carbides are the most common areas of crack initiation [11]. Under TMF conditions, only the crack initiation is similar to the isothermal high temperature case, starting at oxidised carbides and surface pores. The dislocation movements which dominate the crack growth of isothermal fatigue at high and low temperatures are combined in TMF and work in parallel [48]. Additionally, the oxidation, deformation and damage mechanisms may interact, so that an accelerated oxidation layer growth under cyclic mechanical loadings in TMF conditions can occur. Oxidation is commonly considered to be the vital factor for crack initiation and crack growth in TMF loadings. A detailed knowledge of the oxidation behaviour is the basis for life time estimations and damage behaviour. For calculating life times under TMF, oxidation is not merely a parameter which limits the life time, but it is more an independent mechanism interacting with both the others, namely creep and fatigue [48–51].

A number of authors have observed a surface crack initiation in TMF [48, 49, 51, 52]. Oxides are formed in the high temperature segment of the TMF cycle at locations of preferred oxidation, such as surface carbides. In the lower temperature part of the cycle and at very small stresses these oxides undergo brittle fracture. Oxygen can reach the pure metal and the oxidation and crack process starts again, and, in this way, a crack will be gradually penetrate the material. If a critical crack length is reached the crack

propagates by fatigue, enhanced by continued oxidation [51]. Another accelerating factor for TMF damage is microstructural change during the test. At higher temperatures the loss of oxide-forming elements (Al, Cr) in the outer surface zones partly denude the structure of γ'-phase and lead to a local reduction in strength [49–51]. At longer times and higher temperatures the γ'-phase can coarse, which leads to a dramatic reduction in the crack growth resistance of the material [51]. Another important parameter is the cycle shape. Under in-phase conditions a polycrystalline structure produces intercrystalline cracks [50], whereas under out-of-phase conditions, the crack grows only along the crystallographic {111}-planes [49, 50, 53]. With other TMF-cycle shapes (CD, CCD and $\varphi = -135°$) cracks are mostly transgranular [51, 52].

An order of severity of different cycle shapes has been found by systematic research on nickel base superalloys. The shortest lifetimes are encountered in OP cycling, caused by the opposite direction of the thermal and the applied mechanical strains, with the highest stresses coinciding with these extrema [51]. IP cycling is considered to be the least aggressive test shape, where creep is the dominant damage mechanism. The diamond cycles (CD, CCD) are between both other cycling types and have a lower damage factor, caused by the non-coincidence of thermal and mechanical peak loads [49, 52, 53]. An increase in maximum temperature always reduces the lifetime in all cycling types [50, 51]. Small initial secondary cracks grow to produce one final crack through the specimen [52]. Most of these tests were carried out under argon atmosphere, where oxidation growth is reduced and fatigue is the primary damage. Ngala et al. [18] report a different behaviour under air atmosphere, where oxidation is one of the main contributors where IP cycling reduces the lifetime compared to out-of-phase. This is attributed to environmental and time dependent damage mechanisms, where induced cracks are opened at high temperatures leading to rapid crack nucleation and an accelerated propagation rate due to the large plastic strains imposed at high temperature. Oxidation and creep activity are favoured under IF and IP TMF cycling with crack opening at high temperatures.

2.1.3. Creep

Creep behaviour describes a time-dependent plastic deformation of crystalline materials under isothermal temperatures of $T \geq 0.4T_m$ and homogeneous loadings, e.g. stresses [54, pg. 95]. It is influenced by the applied stresses, the matrix internal interactions with alloying elements and particles and their interactions with the dislocation structure [1] involving similar mechanics to those described earlier for plastic deformation during high temperature fatigue. To investigate the creep behaviour of metallic materials, the resulting strain is continuously measured under constant temperatures and mechanical stresses until fracture. In general, a creep curve (plot of creep strain vs. time) can be divided into three characteristic sections, primary creep, secondary creep and tertiary creep, figure 2.5a. Primary (transient) creep of high strength materials is, in most cases, characterised by a creep rate $\dot{\varepsilon} = \frac{\partial \varepsilon}{\partial t}$ which decreases with time. Secondary, or steady, creep has a constant creep rate $\dot{\varepsilon}_s$. Tertiary creep has a higher, and accelerating, creep rate due to the specimen wasting and an increasing formation of pores, and is followed by final failure [54, 55]. The schematic plots in figure 2.5 show the creep response under constant temperature and loading. The solid lines denote constant stress and the dashed ones are used for constant loading. Figure 2.5a shows the resulting strain plotted vs. time, and figure 2.5b shows the derivative (creep rate) vs. strain, commonly used to identify the three different creep stages. It should be mentioned that these relations are only valid for a stable microstructure during the test. As most technical high strength, high temperature materials exhibit microstructural changes during their creep life, a minimum in the creep rate is observed. For these cases and for creep tests under constant loading, the steady state creep rate is replaced by the minimum one for design purposes [56]. The primary, secondary and tertiary creep at given temperature and stress can be described phenomenologically using a single continuous equation of the form:

$$\varepsilon = \beta t^{1/3} + \gamma t + \delta t^3$$

where the parameters β, γ and δ are all functions of temperature and applied

stress [57].

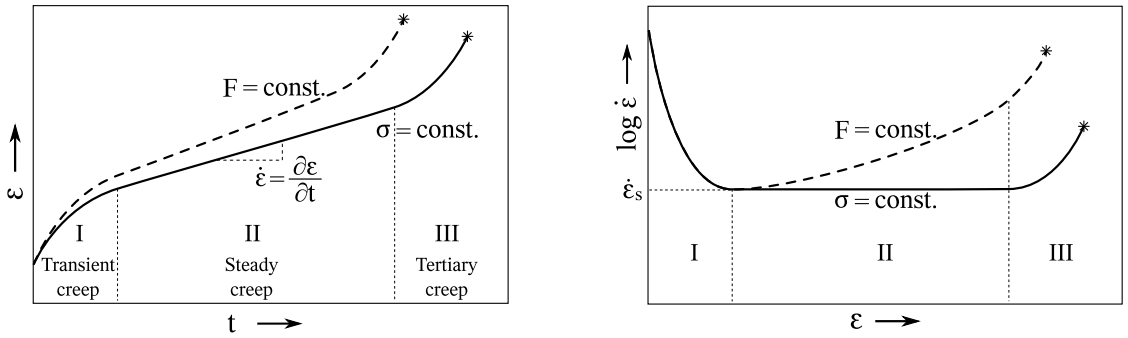

(a) Creep curve, strain development during the test, $\varepsilon(t)$.

(b) Differentiated creep curve $\dot{\varepsilon}(\varepsilon)$ for constant stress and loading.

Figure 2.5: Schematic creep curves with a constant stress (solid line) or load (dashed line), showing the three typical stages [55].

The steady creep behaviour of most technical materials under medium or high stresses can be described by the Norton creep law, equation 2.5, [1, pg. 36], where three parameters A, n and Q are the characteristic of the material and its condition. The temperature dependency is realised by the Arrhenius term $exp\left(-\frac{Q}{RT}\right)$, where Q is the activation energy, usually that for self-diffusion of the metall matrix and is associated with dislocation climb and vacancy migration. The Norton law has limited validity at high stresses due to the breakdown of the power [54].

$$\dot{\varepsilon} = A\sigma^n \cdot \exp\left(-\frac{Q}{RT}\right) \tag{2.5}$$

A ... Constant, f(material and its conditions)
n ... Creep exponent
R ... Gas constant
Q ... Activation energy

The creep exponent n can be determined on linear correlation in a double logarithmic isothermal plot of stress vs. creep rate, figure 2.6 and equation 2.6. A typical correlation between steady creep rates and applied stresses at a constant temperature for a single phase material is given by the schematic plot in figure 2.6a. The stress exponent n

has typical values for pure metals of $n \approx 4-5$. Multiphase alloys usually have exponents up to $n \approx 40$.

$$n = \frac{\Delta \log \dot{\varepsilon}}{\Delta \log \sigma} \tag{2.6}$$

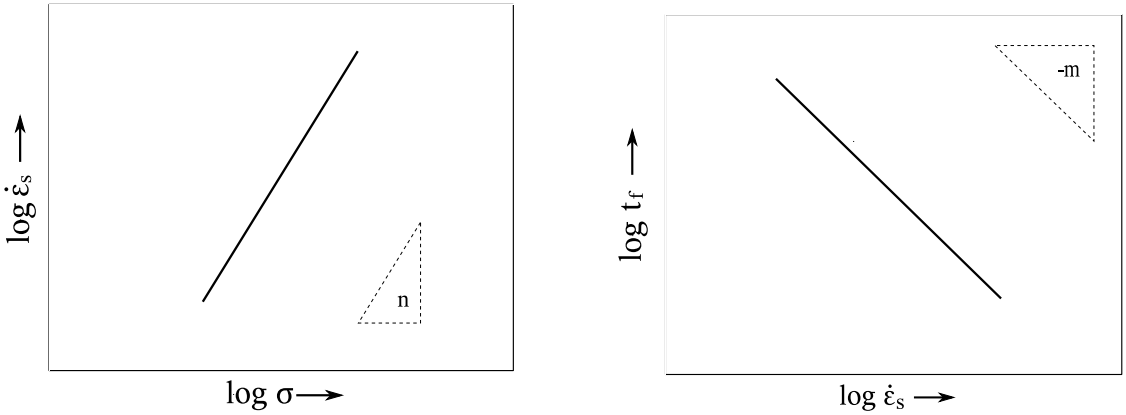

(a) Creep rate vs. applied stress, $\dot{\varepsilon}_s(\sigma)$ and resulting creep exponents n.

(b) Relation between time to failure and minimum creep rates, $t_f(\dot{\varepsilon}_s)$.

Figure 2.6: Schematic relation between creep rates, stresses and time to failure.

Monkman and Grant [58] have observed a strong inverse correlation between the time to rupture (t_f) and the minimum (or steady) creep rate ($\dot{\varepsilon}_s$). Figure 2.6b shows schematically the lifetime dependency on minimum creep rate. This relation (equation 2.7) is typically used for calculating estimated lifetimes of pure metals and solid solution alloys [54, 58–62]. An increase in the test temperature can reduce the experiment duration, to predict real lifetimes under relevant operating temperatures from short high temperature laboratory tests, without the loss of confidence in lifetime extrapolations.

$$t_f = \frac{C_{MG}}{\dot{\varepsilon}_s^m} \quad \text{or} \quad \dot{\varepsilon}_s^m = \frac{1}{t_f} \cdot C_{MG} \tag{2.7}$$

C_{MG} ... Monkman-Grant constant
m ... Constant, in most cases ≈ 1 [54, pg. 174]

The relation between the creep rate and the time to failure can be described by

$$\dot{\varepsilon}_s \sim \frac{C_{MG}}{t_f} \tag{2.8}$$

for the most cases.

2.1.4. Oxidation

Protective oxide coatings grow on metal surfaces slowly, at full density and more or less without defects. Ideally, in the absence of a superimposed mechanical loading, the result is a thin, coherent layer, which separates the reacting components metal, and oxygen. In this idealised case, additional oxidation is only possible if diffusion takes place through this layer. Depending on the diffusion velocity of metal cations and oxygen anions through this oxide layer new oxide can grow on the oxide surface or at the metal/oxide interface. Besides these volume oxidation mechanisms diffusion through oxide grain boundaries or micro cracks in the layer has been investigated by Kofstad [63]. The resulting loadings of the oxide layer system can be calculated with a total stress $\sigma_{ox,tot}$, equation 2.9, although this analysis disregards plasticity and creep effects and assumes elastic isotropy for calculating internal stresses.

$$\sigma_{ox,tot} = \sigma_{ox,ext} + \sigma_{ox,th} + \sigma_{ox,gs} + \sigma_{ox,relax} \tag{2.9}$$

$\sigma_{ox,ext}$	Stress due to external loading
$\sigma_{ox,th}$	Stress due to differential thermal expansion in composite system
$\sigma_{ox,gs}$	Growth stresses
$\sigma_{ox,relax}$	Stress reduction (creep, crack formation)

2.2. Nickel Base Superalloys

Nickel based superalloys are currently the most important materials for increasing operating temperatures to achieve improved efficiency in turbines. The combination of mechanical, chemical and machining properties of the base metal Ni is the reason for widespread acceptance for such applications. These alloys exhibit a heat resistance to up to 85 % of their absolute melting point. This is usually achieved by a combination of the hardening effects of carbides and γ' precipitates. Bürgel [54] has summarised the essential features of the nickel γ-matrix as follows:

- For the complete temperature range up to the melting point nickel has an fcc structure. Nickel has a high solubility for other materials e.g. chromium, cobalt or molybdenum. It forms a solid solution microstructure without any phase instability. The close-packed face-centred cubic structure has an inherently lower self-diffusion coefficient than the bcc lattice.
- Corrosion protection for higher temperatures is easy to realise with moderate amounts of Cr and Al. The ease with, which Ni-materials may be coated allows an additional protection in contrast to other refractory alloys. The presence of Cr_2O_3 and Al_2O_3 layers retards the outward diffusion of metal atoms and the diffusion of destructive elements into the volume.
- Nickel is the only base element which allows an increasing strength at higher temperatures by alloying, achieved through precipitation hardening with a high volume fraction of γ'-phase.

There are two main limitations to the application of these materials. First is the relatively low melting point of Ni (1455 °C) further reduced by alloying elements. Secondly, the low thermal conductivity of Ni in combination with a high thermal expansion coefficient results in susceptibility to thermal fatigue on cycling to high temperatures.

The γ' intermetallic precipitates are characterised by an fcc $L1_2$-structure (figure 2.7b) with the chemical composition of $Ni_3(Al, Ti)$ and the coherency arises from

the similar positions of Ni atoms in this structure. The alloying concept is to increase the volume fraction of particles (up to 70 %). The coherency of the particles produces dislocation interaction which is the main factor causing the high strength of these nickel based materials [64].

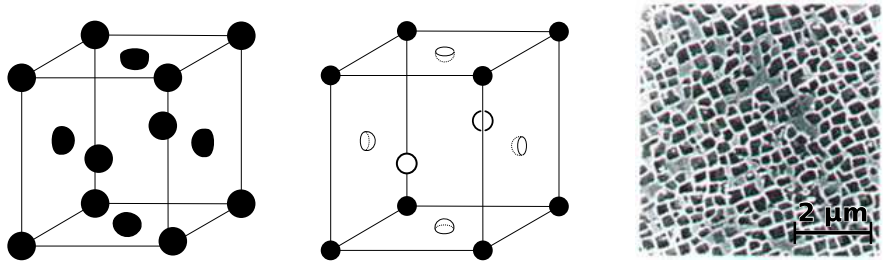

(a) Crystal structure of γ matrix with Ni or Al atoms [65].

(b) Crystal structure of γ' precipitates, black stands for Al or Ti, and white for Ni [65].

(c) Microstructure of γ-γ' combination.

Figure 2.7: Crystal structure of the matrix (γ), the precipitates (γ') and the typical microstructure of this combination.

The small mismatch the γ and γ' lattices is the key to this strengthening. Firstly, when combined with the cube-cube orientation relationship, it ensures a low γ/γ' interfacial energy. The ordinary mechanism of precipitate coarsening is driven entirely by the minimisation of total interfacial energy and so the γ' precipitates are resistant to coarsening, remaining small and highly dispersed. The presence of a coherent or semi-coherent interface is responsible for interfacial matrix-precipitate-stresses and -strains, which stabilises the microstructure in elevated temperature applications and maximises dislocation interaction. The strength of most metals decreases as the temperature is increased, simply by virtue of thermal activation, which makes it easier for dislocations to climb obstacles. Hence, it is the presence of the very high volume fractions of γ' which is responsible for the strength of nickel based superalloys being insensitive to higher temperatures. The close match of the matrix/precipitate lattice parameter (δ) combined with the chemical compatibility allows the γ' particles to precipitate homogeneously throughout the matrix and have long-time stability.

The aspects of microstructure affecting mechanical properties of high temperature alloys are dislocation- and twin density, grain size and distribution, type and concentration of alloying elements as well as precipitates. The surface condition, the applied strain amplitudes and the environment can have local effects on the microstructure and, ultimately the lifetime. Microstructural changes after thermal mechanical loadings depend very much on the damage mechanisms occurring during cycling. A typical microstructure, comparable to isothermal fatigue tests, can be reached with a temperature range where only interior subgrain gliding processes are active, leading to a quasi-stationary dislocation structure after a few cycles. The mechanical properties of most Ni-based superalloys depend on carbide formation and precipitate structure, and their influence on dislocation movement [11, 25, 66, 67].

2.2.1. Nimonic 90

Nimonic 90 is characterised by high stress-rupture strength and creep resistance at higher temperatures ($\approx 920\,^{\circ}\mathrm{C}$). The resistance to high temperature corrosion and oxidation is excellent. Nimonic 90 is a 60 % Ni, 20 % Cr, 15 % Co alloy with minor additions of Fe, Ti and Al. The chemical analysis of the particular example used in this work has been carried out by BAM, Germany and has been reported in the TMF-Standard Project, Workpackage 2 [68] and can be found in table 3.1. The material used in these investigations was nearly precipitate free, so that a direct comparison in the TMF behaviour between the matrix material and the strengthening effect of the ODS alloy could be made.

The main alloying elements Cr and Co are very important for the non-precipitate related strength, creep resistance and corrosion resistance. In general, chromium produces solid solution hardening and forms a Cr_2O_3 oxidation layer and also supports the generation of Al_2O_3 as an additional protective coating. Cobalt reduces the γ'-solution annealing temperature and stimulates the formation of cubic γ' precipitates. Due to this reduced temperature irregular γ'-particles will be suppressed. The Al and Ti solubilities are is also lowered, which results in substantial amounts of γ' at medium temperatures.

Furthermore Co reduces the stacking fault energy of the matrix and so increases the creep resistance [54].

2.2.2. Oxide Dispersion Strengthened Alloy PM 1000

The superalloy PM 1000 contains a dispersoid phase Y_2O_3, which also contributes the above mentioned heat resistance. Hence, it is called an oxide dispersoide strengthened (ODS) superalloy and exhibits an excellent corrosion, fatigue, creep and oxidation resistance at temperatures up to 1000 °C. The Y_2O_3 is present in the form of isolated particles with a mean diameter of 14 nm and an average planar centre to centre spacing of 100 nm [21, 69]. The matrix phase is 75 % Ni, 20 % Cr, 3 % Fe with much smaller amounts of Ti and Al than Nimonic 90. This kind of alloy is manufactured by mechanical alloying techniques. Figure 2.8 presents roughly the different manufacturing steps. One of the main stages is the refining of elementary or alloyed metal powders by high-energy milling, where powders of extremely fine-grained structures are produced. In this way, the incoherent oxide particles are uniformly distributed throughout the matrix allowing them to interact with lattice dislocations [70]. A fully dense material is produced by means of hot compaction of the alloyed powder. The rolling processes give the material a strong texture in longitudinal direction, responsible for the high temperature creep and fatigue strength. The effect of texture on mechanical behaviour is presented by Müller et al. [23] and earlier literature has addressed the isothermal low-cycle fatigue behaviour [21, 23], creep [69] and oxidation behaviour [71]. Other work deals with TMF behaviour of this superalloy under both, IP and OP conditions [18]. The specification with a phase shift of $\varphi = -135^\circ$ representing the operating conditions of the leading and trailing edges of a blade has not been investigated and should be compared with the results of the IP and OP cycle shapes.

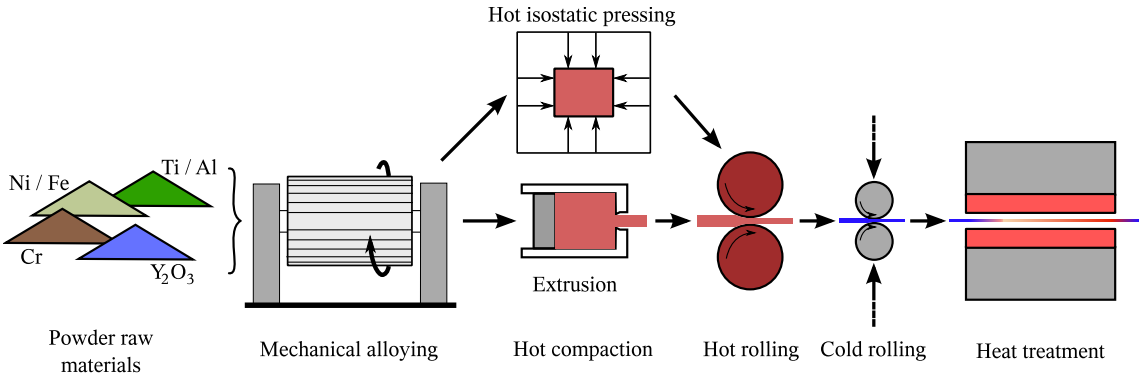

Figure 2.8: Manufacturing of semi finished products from ODS alloys [72].

2.3. Protective Coatings

One of the most important aluminide coatings applied to turbine blades is $\beta - \mathrm{Ni\,Al}$ because of its excellent mechanical properties as well as its lower density than nickel and its significantly higher melting point at 1638 °C compared with 1453 °C for nickel and 660 °C for aluminium [73]. The aluminium oxide zone formed on the coated surface at lower temperatures is stable at higher temperatures and is impermeable to oxygen, which is the reason for using this compound in coatings for engine blades or automotive engine components.

Coatings protect the surface of turbine blades from damage caused by high temperature corrosion and preserve the structural material and the mechanical properties for the service life. Many authors have presented experimental studies of fatigue strength and thermal fatigue of coated superalloys [11, 74–81], but the connection between the physical and mechanical properties of protective coatings and the effect on mechanical properties of superalloy blades has not been studied sufficiently yet. For thin diffusion coatings, this can be explained by the complexity of the task of reproducing the exact composition and in testing the coatings separately from the alloy [82]. However, information on the physical and mechanical properties of these coatings are essential for their improved future application and for accurate assessment of the service life of coated blades.

Grube et al. [74] describe the fatigue behaviour of a platinum modified aluminide-

coated mono-crystalline Ni-base superalloy under TMF-conditions and discuss the influence of the coating on the superalloy [11]. The microstructural research of Zhang et al. [75] revealed the influence of TMF tests on the coating and its influence on the substrate material. Isothermal fatigue tests were carried out by Xu et al. [76] to determine the hot fatigue behaviour of coatings produced with an electron beam physical vapour deposition manufacturing process.

Coatings affect the mechanical properties of superalloys in several ways. Firstly, the deposition of the coating alters the superalloy's surface stress, so that later it can be damaged under the action of static or alternating stresses. Cracks in the coating may accelerate the base material damage process. The mechanical properties of superalloys may be affected by the thermal cycle of the coating deposition, and the surface layer microstructure of the superalloy is changed by the coating, and this effect is intensified by high temperature exposure. The efficiency with which information on the influence of coatings on superalloy properties depends very much on the test methods used. Internally cooled blades are thin-walled components where the effect of the coating on the mechanical properties of the component is significant. For mechanical testing, the ratio of coated cross section to overall specimen cross section should be close to that of the blades in use. Aluminide properties themselves such as yield strength, ultimate strength and elongation depend very much on their structure, which is determined by the specimen fabrication process and heat treatment. Table 2.1 presents test results from one of the earliest publications on aluminide mechanical properties.

As is typical of all body-centred cubic lattices aluminides exhibits a ductile-brittle transition at a certain temperature depending on the particular Ni Al compound. Research on the high temperature strength of Ni Al and has revealed that the high temperature strength of superalloys is generally much higher than the strength of the coating.

In coatings obtained by aluminising nickel alloys in media containing aluminium and its compounds, the following aluminides can be formed: $NiAl_3$, Ni_2Al_3, Ni Al and Ni_3Al. Relevant physical and mechanical properties can be found in appendix table A.5. There are many important factors which influence the formation of diffusion coatings on

Table 2.1: Properties of Ni_3Al and NiAl intermetallic-base cast alloys at tensile tests at room temperature [83]. For the chemical composition (Al content of 35 wt %) no data are available.

Aluminium content, wt %	Ultimate strength (σ_B), MPa	Yield strength ($\sigma_{0.2}$), MPa	Elongation (δ), mm/mm
13.3	205	86	0.011
14.0	280	110	0.010
25.0	163	...	0
30.0	103	...	0
31.5	102	...	0

superalloys, such as the aluminising temperature, the thermodynamics of the aluminide formation reaction, the kinetics of the diffusion process, the chemical and phase composition of the base superalloy and the activity of the medium used for aluminising. The phase composition and the initial structure of overlay coatings are highly dependent on the chemical and phase composition of the alloy, the surface temperature upon which the deposit is condensed and the state of aggregation of the substance transferred.

2.3.1. Technology and Microstructure

The mechanical properties of coatings vary with the manufacturing processes as well as the formed microstructure and the grain-sizes and their distribution. The reproduction of aluminide compositions identical to diffusion coating modifications is a very difficult tasks in material sciences, because the sample thickness is usually comparable to the coated blades. First, the coating must be separated from the substrate material to avoid influences to the material properties and second it is very expensive to cut samples out of a final blade. The ductile-brittle transition temperature (DBTT) of the diffusion coating should be matched to its service life criterion under static and cyclic loading, because this transition plays a vital role for many characteristics of the coatings as well as the way it affects the superalloy properties. The DBTT is usually determined by four point bending tests over a defined temperature range.

Typical oxidation protection layers are categorised as deposition or diffusion coat-

ings, depending on the production process. *Deposition coatings* are usually made by applying coating material to the surface with PVD or plasma spraying techniques. For the complex geometries of turbine blades these methods are not always the ideal way, since the very small air cooling holes and channels inside the blade can be blocked by the applied coating material. For these geometries the CVD technique realises a complete and consistent coating including all holes. Riethmüller [84] describes the detailed process of the coating formation as follows. A chemical reaction allows non-volatile elements to be released from the bulk as compounds and transported by the vapour phase to the coating surface, where these volatile compounds firstly are adsorbed and then dissociate. The deposited material diffuses into the volume and, in combination with the substrate, forms the coating phases. Hence, the final coating is an interdiffusion layer between substrate and deposited material.

Broadly speaking, there are three different production processes for making the coatings alone without the help of a base material:

- pulverising
- gas phase condensation
- wet chemical process

Bönnemann et al. [73] describe a production process of NiAl based on pulverising of the two elemental components. Conventional coarse-grained material with a diameter > 1 µm, produced by pulverising at temperatures between 800 and 900 °C with the mechanical alloying process is usually very brittle on room temperature. By decreasing the grain size to a few nanometres the ductility, rupture strength and the hardness can be increased. Mechanical alloying has two main disadvantages. Firstly, particles have a tendency to agglutinate easily at higher grinding temperatures to larger units, and secondly much of the base Ni as well as Al is not completely mixed, so unalloyed material exists in the compound.

Nano crystalline NiAl, produced by gas phase manufacturing, has a significantly higher micro hardness than pulverised materials. The specimens used for these experiments were produced by gas phase condensation in an alitising reactor, containing a granulate of Al, Cr and an activator. The reactions take place at $\approx 1100\,^{\circ}\mathrm{C}$ in 20 – 30 hours.

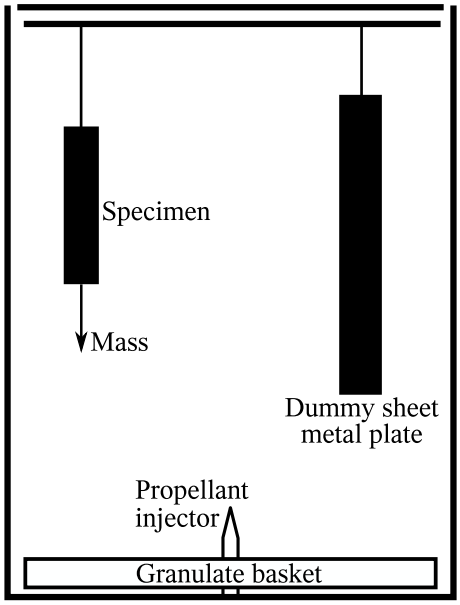

Figure 2.9: Schematic reactor design for gas phase alitising. The basket is filled with a granulate of Al, Cr and an activator [25, 84].

The intermetallic phase β-NiAl

The intermetallic phase β-NiAl is the basis of all modern NiAl coating systems and plays a vital role in the mechanical stability of blade coatings.

The regularly oriented crystalline structure of β-NiAl consists of two interpenetrating cubic basic lattices, consists of Ni and Al atoms, respectively. The result is a body-centred cubic CsCl-type structure, commonly known as B2-structure.

Interesting for high temperature applications are the following properties, investigated by Miracle [86]:

- the high melting temperature ($T_m = 1638\,^{\circ}\mathrm{C}$).

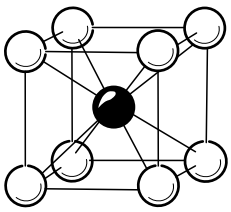

Figure 2.10: B2-crystallographic structure of β-NiAl, white symbolises Ni and black Al atoms [85].

- high strength
- high oxidation resistance
- good plasticity at elevated temperatures
- low density

The binary system Ni-Al (figure 2.11) is characterised by many intermetallic phases. As can be seen the regular structure of the β-NiAl phase is stable over the complete temperature range until the melting point. Also, NiAl has a wide phase field which means that variations in the stoichiometric composition of a few at% do not influence the phase stability. Nickel rich NiAl can contain as much as 65 at% Ni, while the Al rich NiAl can contain as much as to 55 at% Al. These limits remain even if some of the Ni or Al are replaced by different elements although it might be noted the melting point of the compound drops of quite sharply at the side of the stoichiometric ratio, particularly on the Al-rich side. In general, the crystallographic structure influences the resistance to movement of any lattice imperfections whether they be vacancies and dislocations or grain boundaries. On the one hand, the difficulty of dislocation movement can be cited as the reason for the high strength of NiAl, although, on the other hand, this also results in fairly poor ductility at temperatures below the ductile-brittle transition temperature (DBTT), depending on the exact chemical composition (300 °C $< T_{DBTT} <$ 500 °C) [86].

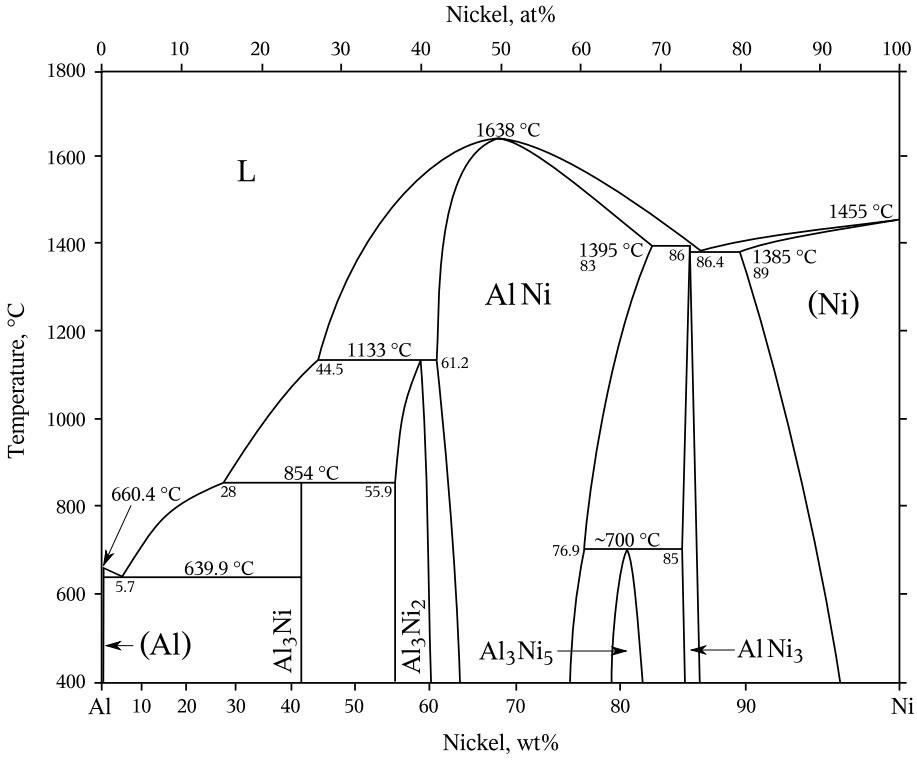

Figure 2.11: Phase diagram of the intermetallic compound NiAl [87].

2.3.2. Deformation Behaviour

In service, thermal coatings have to resist a range of varying types of loading, which lead to totally different damage behaviours. In principle, if a material damage parameter is exceeded by actual local loads, damage will commence. This behaviour is not comparable to the Nickel based. At high temperature environmental loadings the capacities of materials develop in opposite directions, resulting in a finite lifetime. The final failure of a coating can be defined as the de-lamination of the ceramic topcoat during the cooling cycle. Three types of de-lamination can appear, black failure for damage initiation at the interface of between the barrier coating and the thermally-grown oxide, white failure for a location inside the ceramic topcoat and mixed mode failure for a combination and rippled surfaces [88–91]. Isothermal tests are dominated by mixed mode failures, whereas white failures are the main mode under thermo mechanical testing conditions. Three main time- and temperature dependent factors, oxidation, sintering and geometrical factors, influence

the preceding damage. *Oxidation*, includes the following mechanisms:

- growth of a TGO as an additional part of the coating system with its separate mechanical properties, which influence the local stress state of the layer system
- formation and augmentation of physical defects inside and at interfaces with the TGO, which boost crack initiation
- volume oxidation, starting at precipitates which contain reactive elements and the resulting stress concentration
- stress-reducing visco-plastic effects
- reduction of aluminium level in surface areas of the substrate material with a resulting change of mechanical properties
- diffusion processes on all interfaces with possible formation of porosity, also resulting in a changed mechanical behaviour

Sintering defines time and temperature dependent densification of the ceramic coating with the following effects:

- increase in the Young's modulus
- change in plastic properties
- increase in thermal conductivity

The *Geometrical factors* can include:

- surface roughness of any interface and the related stress localisations inside the coating system
- (time dependent) global stress development at curved specimen geometry, geometrically induced developmental stresses inside the TGO
- stress- and strain singularities at boundaries

3. Materials

This chapter describes the materials and sample preparation used for this investigation. First, the compositions and microstructure of the superalloys are described, followed by the intermetallic layer material.

The chemical composition of the particular preparations of nickel base superalloys investigated here is shown in table 3.1.

Table 3.1: Chemical analysis of the used nickel based superalloys, Nimonic 90 [68, 92] and PM 1000 [72] and the coating layer NiAl [84, 93].

	Chemical composition, wt.%											
	Ni*	Cr	Co	Fe	Ti	Al	Si	Cu	Mn	Zr	Mo	Y_2O_3
Ni 90	59.6	19.08	15.07	0.97	2.46	1.31	0.32	0.11	0.09	0.06	0.86	-
PM 1000	75.6	20.00	-	3.00	0.50	0.30	-	-	-	-	-	0.6
Ni Al	64.2	2.9	7.5	0.04	traces	23.2	-	0.55	0.09	-	-	-

* Nickel proportion calculated as the remainder with all other components subtracted from 100 %.

3.1. Sample Preparation and Microscopy

The metallographic samples were prepared as follows. To avoid thermal influences on the microstructure all specimens were cut with a low speed saw using a special cutting fluid. Figure 3.1 shows the cutting planes used. The samples were mounted in warm embedding resin which was electrically conductive for SEM analysis. Abrasive papers with grit sizes of 320, 600, 800 and 1200 were used for grinding. The specimens were then polished with diamond suspension of particle sizes 6 µm, 3 µm and 1 µm, followed by etching with different solutions. To visualise grain boundaries as well as pores the colour etchant Bloech & Wedl II [94] was used. For detecting fatigue bands, samples

were electrolytically etched with chromic acid and, for the visualisation of carbides, the Murakami [95] etchant was used. More details e.g. used current, detailed compositions, etc. are given in appendix B.1.

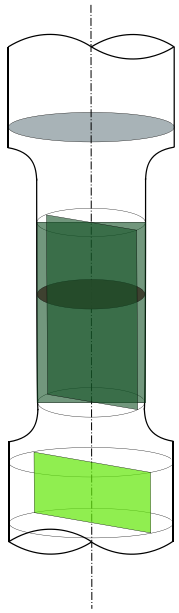

Figure 3.1: Specimen section planes. The gauge length was first separated from the fixation length and then cut longitudinally and transversely in the heat affected zone. The ends of the gripping volume were also sectioned for differential microstructural analysis. Re-drawn with kind permission of Kliemt [96].

3.1.1. Optical Microscopy

For macro photography, a stereo microscope (Olympus SZX 12 in combination with a digital camera ColorView12) was used on prepared and unprepared surfaces. Macroscopic images were made by a desktop visualiser (WolfVision VZ 9). Higher optical magnifications (up to 1000x) were obtained on polished surfaces with an Olympus BX 51 reflection microscope, also equipped with a digital camera ColorView II and a wide range of image treatment, such as bright- and dark field, polariser and interference contrast.

3.1.2. Scanning Electron Microscopy

A SEM (LEO 1455VP) was used to investigate the crack surfaces as well as the internal specimen structure after the TMF tests. The SEM was equipped with a secondary electron (SE) and a backscattered electron (BSE) detector for detailed information on the material and its chemical nature. The acceleration voltage could be varied from 0.5 kV to 30 kV. Finally, the pressure of the vacuum could be varied for better investigation of embedded specimens without gold sputtering.

3.2. Nimonic 90

Figure 3.3 shows the dog-bone shape design, used for the Nimonic 90 TMF investigations. The material was supplied by the CoP-project[1] batch, produced by Special Metals Wiggin, UK. Bars of 20 mm diameter were solution heat treated at 1080 °C for 8 hours, water quenched and aged at 850 °C for 5 hours. This temperature/time combination was selected to take the material beyond the peak hardness to its softest condition. In this project, the aim was to get a material not at its best condition, but rather under most stable conditions to minimise any start-up effect and with minor aging impacts to the hot-temperature exposure time [68]. The final design was prepared by CNC-machining and, additionally, the gauge length was polished to a surface roughness of $R_z = 1\,\mu m$ to avoid premature crack initiation. The hardness at initial conditions and room temperature was measured to 342 ± 15 HV. The detailed locations are shown in figure 3.2 and the results are listed in table 3.2, respectively. Due to the homogeneity, the values were reduced to an amount of three. The flattend gauge length design is an result of the specimen machining, out of a flattend test bar. To get the correct diameter-length ratio, the diameter reduction was limited. The second important limitation of the specimen design is the application volume, e.g. extensometer, thermo couple, grips.

[1] CoP-project: The *Code-of-Practise project* was founded for a European wide standardisation of TMF test procedures and result interpretations.

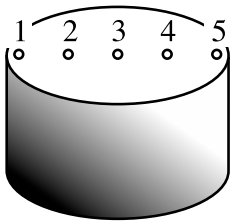

Figure 3.2: Hardness testing locations at the cross section of a specimen.

Table 3.2: Measured hardness of three Nimonic 90 specimen.

Test positions						
1	2	3	4	5	Mean	RMS deviation
358	337	320	339	347	340	14
363	332	325	334	360	343	17
361	344	322	336	359	344	16

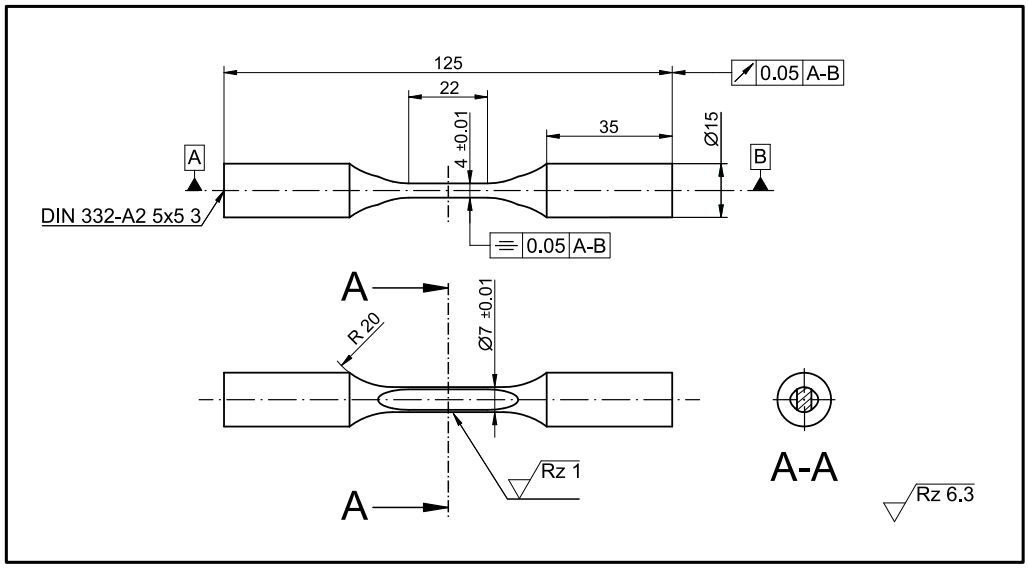

Figure 3.3: Nimonic 90 TMF specimen with flattened gauge length to reduce thermal transients in the volume during heating. (dimensions in mm)

Microstructural Analysis

To investigate the microstructure before and after TMF testing a range of standard procedures were used: macrophotography for documentation of the surface crack propagation behaviour, and optical and scanning electron microscopy (SEM) for the analysis of microstructural effects. Microstructures are discussed in more detail in Chapter 5, but figure 3.4 shows the characteristic structure of the initial material with twinned, equiaxed γ grains of around 250 µm size. The precipitations are not observable at this magnification with optical microscopy.

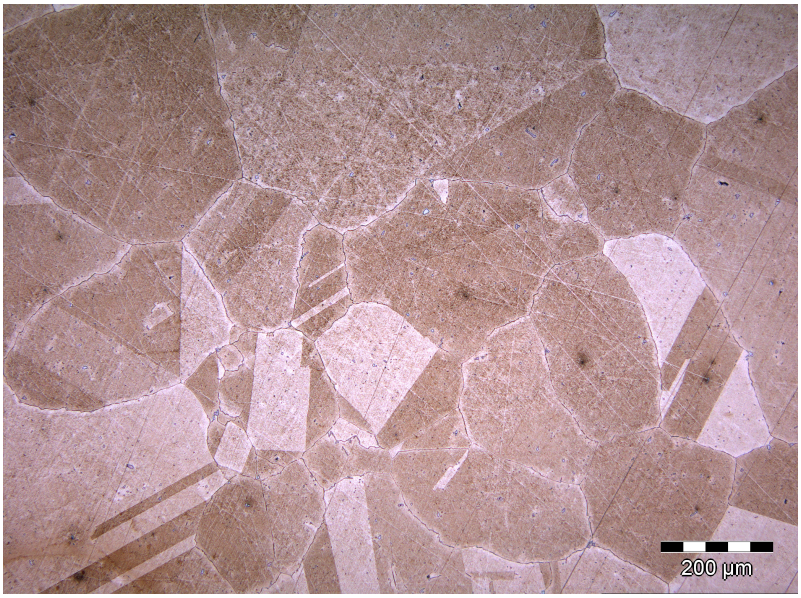

Figure 3.4: Initial microstructure of Nimonic 90.

3.3. PM 1000

This material was produced by Plansee GmbH, Reutte, Austria and has the trade name PM 1000. According to DIN 17742:2002 the designation of this alloy is NiCr8020 with the material number 2.4869 [72]. This solid solution strengthened nickel base superalloy has a chromium content of 20 wt.% and lesser amounts of aluminium and titanium. The detailed metallurgy is described in section 2.2.2, chapter 2 and in [21, 23]. Hardness was

measured at 298±8 HV at room temperature. The indentation procedure and locations are comparable to figure 3.2 of section 3.2. Table 3.3 gives the measured values. The material data sheet of the producer gives a value of 300 HV. In PM 1000, fine yttrium oxides are embedded into the matrix by mechanical alloying, figure 2.8. The resulting dispersion strengthening and the production of a directionally recrystallised coarse grain structure are responsible for the high tensile and creep rupture strength at elevated application temperatures as well as the reduction of grain boundary sliding offered by the coarse elongated grain structure, see figure 3.7.

Therefore other orientations than longitudinal, has to resist only a small portion of elastic strain during the loading. The main part is the plastic strain, developed under thermal fatigue conditions, and leading to a high reduction of fatigue life.

TMF tests were performed with a cylindrical specimen geometry with a gauge length diameter of 6 mm. The design is shown in figure 3.5 and differs from the Nimonic specimen with in that the gauge length to diameter ratio was high. The specimens were also CNC-lathered and polished in the gauge length. Due to the fact that the base material was completely round without any flattend sides like the Nimonic ones, there was no need to use a modified gauge length design.

Table 3.3: Measured hardness of three PM 1000 specimen.

Test positions						
1	2	3	4	5	Mean	RMS deviation
305	298	282	289	297	294	9
312	299	287	290	302	298	10
299	304	292	301	308	301	6

Microstructural Analysis

An optical micrograph of the alloy in the initial condition is shown in figure 3.7. The material consists of coarse elongated grains through out the microstructure. The grains measure 2 mm on average in the longitudinal direction and 0.2 mm in the transversel di-

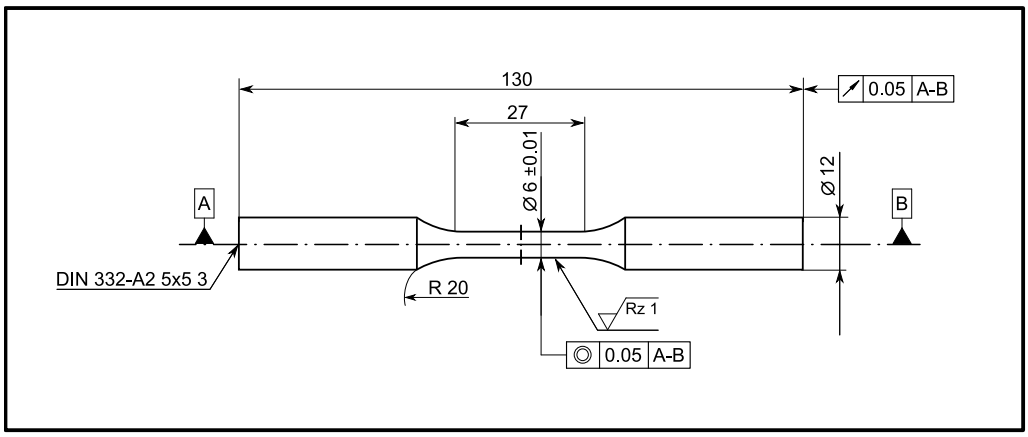

Figure 3.5: PM 1000 TMF specimen, round type without flattened gauge length. (dimensions in mm)

rection, approximately the same as the equiaxed structure of the Nimonic 90. Due to the small grain boundaries areas in transverse direction, these are the weak areas in high temperature deformation, figure 3.6.

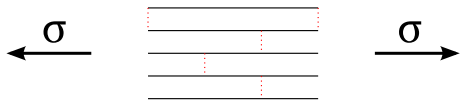

Figure 3.6: PM 1000; The transverse grain boundaries are the weak areas in high temperature deformation.

3.4. NiAl

This study uses $\beta - \mathrm{Ni\,Al}$ specimens with an Al content of $\approx 35\,\mathrm{wt\%}$ and Ni with $\approx 64\,\mathrm{wt\%}$. Thin foils were produced by MTU-Aero Engines GmbH, Munich, Germany using a gas phase condensation process, including heat treatment leading to oxidation of the outer surfaces and therefore to constant deformation behaviour inside the specimen and a well-defined coating system component. The absence of separate phases, e.g. surface oxidation or ductile base material, are the basis for unaffected deformation results. Due to the heat treatment and the thickness of 0.1 mm, the specimens were very wavy, without an exactly definable geometry, and the nominal dimensions are shown in figure 3.8. The chemical composition are summarised in table 3.1.

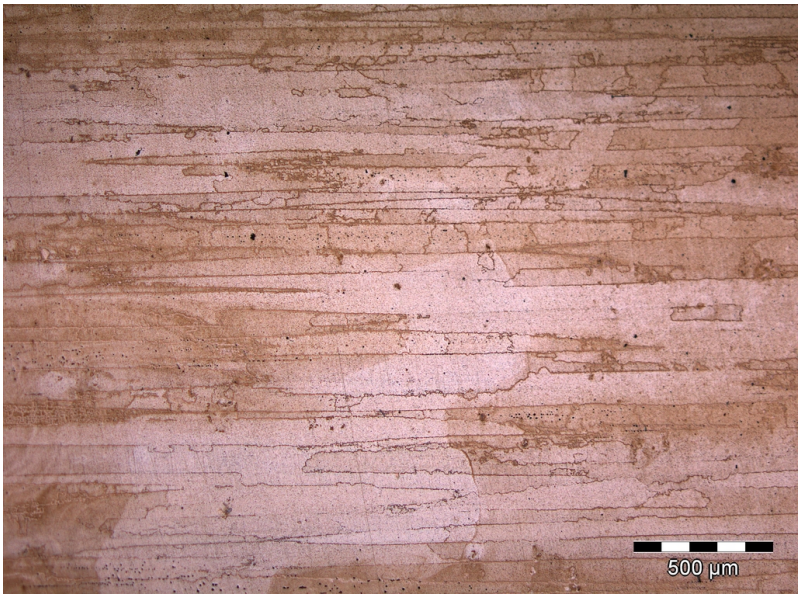

Figure 3.7: Optical micrograph of the longitudinal section under initial conditions of PM 1000 in initial state, corresponding the literature specimen from Ngala et al. [18]. At this magnification dispersoids are not detectable.

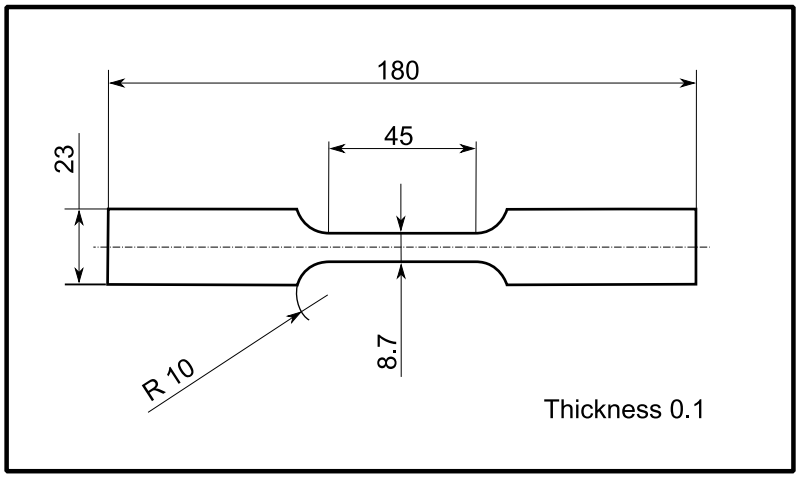

Figure 3.8: Technical drawing of NiAl specimen. (dimensions in mm)

The surface of the specimen is characterised by a rough grain structure, figure 3.9. The grains can be identified without any etchant and have a size of 180 µm in average. Due to the heat treatment during the production, aluminium oxides will be formed much more at the grain boundaries, resulting in the observed widened grain boundary structure. Riethmüller [84] observed an enhanced Al content at the grain boundaries. The effect of this irregular Al content leads to different oxidation and therefore to an inhomogeneous surface structure. Figure 3.9 shows the initial state before creep. Large oxidation zones at the grain boundaries are observable.

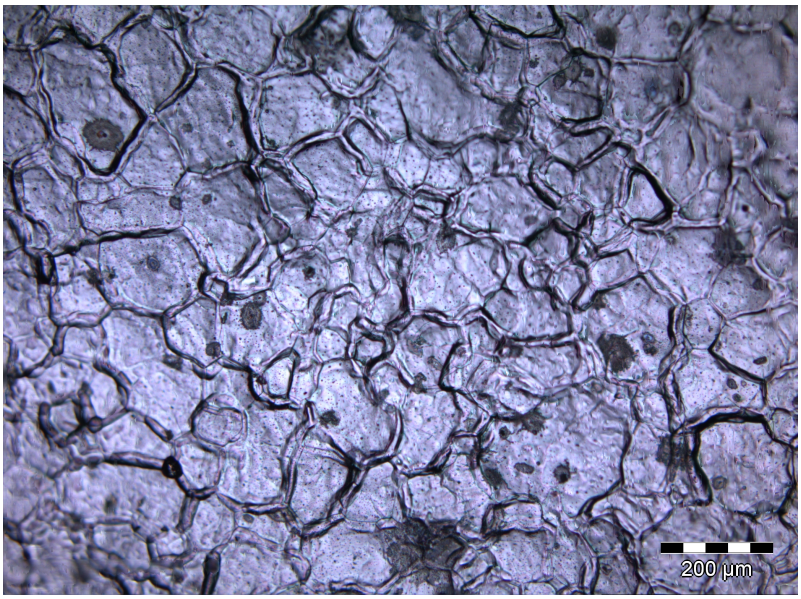

Figure 3.9: Initial NiAl specimen surface micrograph. Irregular, coarse grains dominate this surface. This picture was taken without any specimen etching.

4. Experimental Methods

A significant proportion of the innovation in the current work lies in the development of a new technique for mesuring the TMF behaviour of trubine blade alloys. Hence, the first part of this chapter is devoted to a description of the principle control issues in TMF testing and how the technique addresses there. The remainder of the chapter describes the application of the technique for the two superalloys studied, and also its application to the challenge of creep testing of Ni Al thin films.

4.1. Experimental Set-up

The experimental varieties in TMF, in particular the effects of temperature controlling equipment and the temperature error achieved, has been investigated by Marchionni et al. [37]. A correction of the thermal strain component in equation 2.4 influences the complete TMF test, i.e. the resulting stresses and, accordingly lifetime data. There are two different options in practise, time- and temperature dependent correction [97]. The elimination of control deviations is easier with a time-dependent correction of ε_{th} and, this is used in most laboratories [28]. This controller type stores the measured thermal strain in an array with constant time increments. The actual applied thermal strain is taken from this array depending on the actual cycle time. A reduced long-term stability is one of the main disadvantages of this approach, because it ignores changes of the specimen surface such as the growth of oxidation layers or other environmental temperature deviations, i.e. air turbulences.

Another solution is temperature based correction. The thermal strain is calculated

in real time from the actual measured temperature. Since this controller type cannot be influenced by a modified set point waveform, the need for exact temperature data is evident. In the end, this method is less sensitive to any drift errors in temperature control.

Kühn et al. [26] compared these two control systems using a predefined temperature error, as an indication of the accuracy and stability of the temperature cycles during the complete test, and measured the resulting hysteresis. As a reference cycle they took the hysteresis without any temperature error, and, by changing the error to an overshoot or a reduction the tendency of the resulting energy was analysed. A typical set of σ-ε_m hysteresis curves for varying error is shown in figure 4.1.

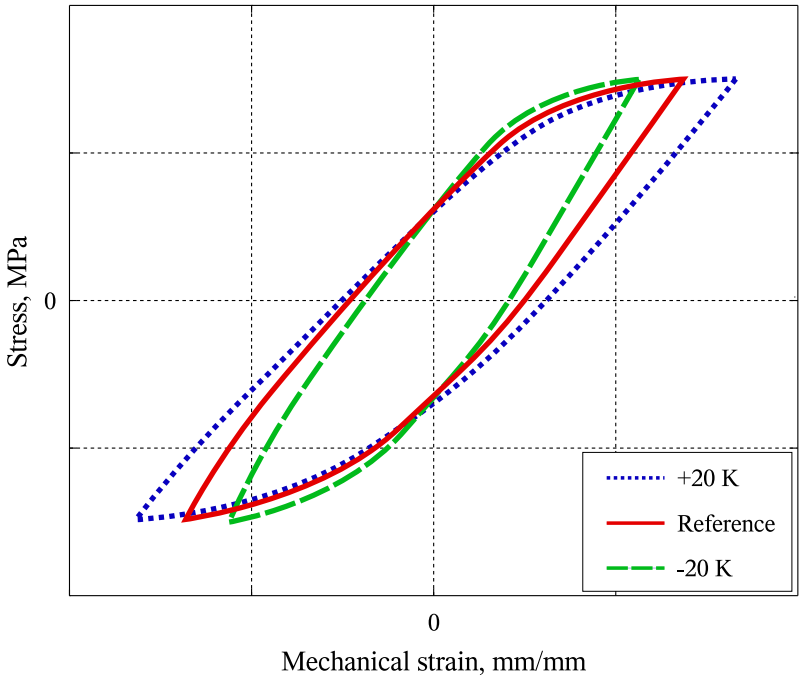

Figure 4.1: Typical stress vs. mechanical strain plot with varying temperature errors, replotted with kind permission of Kühn et al. [26].

A verification of the temperature-based thermal strain correction controller is presented by Kühn et al. [26]. They conclude a high sensitivity for temperature-based tests in nominal thermal errors[1]. The whole system is influenced by the temperature sensitivity of the test material and the superimposed mechanical strain amplitude deviation and addi-

[1] *Nominal thermal error*: A small error in temperature achieved at a defined time

tionally the cyclic deformation and the lifetime. The obvious dependence of temperature instabilities and the resulting hysteresis energy for both types of testing systems can be found schematically in figure 4.2. Clearly, temperature-based tests are less sensitive to temperature errors, and the thermal strain compensation is directly related to the temperature signal, so that no additional mechanical strain error can appear. Kühn et al. [26] performed the tests at a special procedure, not to observe lifetime data, just to investigate the correlation of the temperature deviation to the material stresses. The overall aim of this study was to analyse the required accuracy under a few thermal transients and describe the resulting temperature deviations with repsect to the temperature error. They observed an acceptable thermal accuracy of <20 K for small transients (5 K/s). Furthermore, they conclude that for these small transients the limit of the technical feasibility for T_{max}/T_{min} under TMF conditions is currently at $\pm$5K. To investigate higher thermal transients of more than 5 K/s for more realistic data, a significant higher accuracy is mandatory. Due to the typical operating conditions of turbine blade with transients of $\approx$100 K/s during the engine start, the test equipment was designed especially for higher transients (>5 K/s) in combination with higher accuracy. The limitation of this set-up can be fixed by rates of >35 K/s. Beyond this limit the sampling and calculation rates are not as high as required to perform tests with such an accuracy.

The used test rig developed for this work is shown schematically in figure 4.3. It consists of a conventional mechanical set-up and a purpose-designed software based temperature controller. Incoming signals are listed on the left side, necessary for the TMF cycle description, e.g temperature and strain behaviour and the corresponding transients. The basic inputs for staring the test are marked in red. Other input signals for running the "main" lifetime investigations are marked in green, e.g. temperature dependent thermal strain and Young's modulus of the test material. These values are measured and analysed at the "Pretest" procedure and provided to the main test software. The *temperature inputs* T_1 to T_5 can be used for analysing temperatures at different positions of the specimen to get a temperature field. Digital trigger lines were used to release the image acquisition at special "cycle events", e.g. at peak temperature, peak stresses, reaching a certain stress

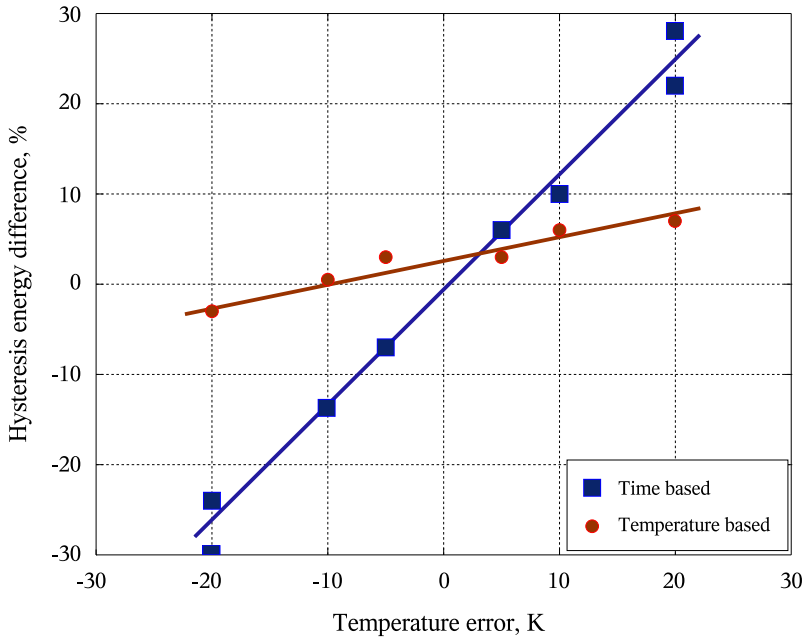

Figure 4.2: Correlation between time- and temperature-based thermal strain correction, re-plotted with kind permission of Kühn et al. [26].

level, etc. *External signals* were used to measure additional signal, e.g. external extensometer for calibration and final shutdown for the creep tests, or the digital data of some image points during the thermographic observation. All of these signals are included in the final data file with the advantage of having the same time base. The actual heating generator data, like output voltage (U), current (U), power (P) and frequency (f), are also measured for further use, especially to optimise the induction coil design. These values present the heating efficiency. Force, displacement, total strain as well as the safety checks (F, s, ε) are signals in both ways. They were provided to the test machine and the specimen's response is measured and analysed simultaneously. All transfered data are not influenced by additional software to avoid interferences or delays. Safety checks are required for a defined test end without specimen destruction as well as for the general safety. Another feature of the system is the opportunity to superimpose the setpoint temperature-strain signal with a small strain amplitude at high frequency (in relation to the cycle frequency) to simulate the oscillating stresses in a turbine blade. The overall result (stress as function of cycles to failure, $\sigma(N_f)$) is shown on the right side in this graphic.

Figure 4.4 shows the actual main components viewed from the front.

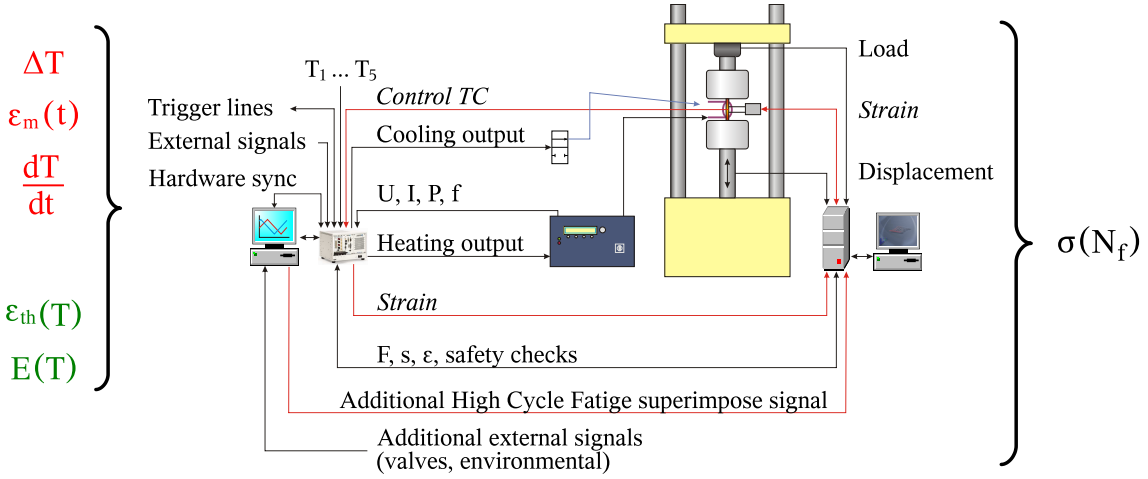

Figure 4.3: The TMF system scheme including input signals and measured ones. The arrows symbolise the signal paths. The red lines symbolise the control signals.

Based on the complexity and the lack of standardisation of TMF-experiments the approach of this work has been to design an improved test rig and to validate the rig by carrying out thermal-mechanical fatigue experiments on the well characterised nickel base superalloy, Nimonic 90. While the control of the mechanical strain signal ε_m can be regarded as sufficiently precise using current experimental practise, the contribution of the thermal strain ε_{th} can only currently be calculated indirectly on the basis of the actual measured temperature data. Therefore, a major feature of the experimental set-up was the highly accurate measurement and control of the temperature. Brendel et al. [39, 98] have demonstrated, how the thermal transient behaviour of an inductive heating element affects specimen lifetime and critical stress areas. These investigations suggest that thermal gradients of at most 5 K/s can be accommodated in a time-based thermal strain correction [2]. Under high rates of thermal ramping (heating rates in the order of 10 K/s) nonstationary temperature fields are set up within the volume of the gauge section of the specimen. These thermal gradients cause fluctuations in the actual thermal strain and thus generate thermal stresses which are superimposed to the induced mechanical stresses, according to:

$$\Delta\sigma = \Delta\varepsilon_m \cdot E \tag{4.1}$$

The implications in terms of poorly specified specimen damage and a misleading interpretation of the results are significant. In the case of a nickel base superalloy ($E \approx 180\,\text{GPa}$) a temperature deviation of $\Delta T = 10\,\text{K}$ at a mechanical strain of $\Delta\varepsilon_m = 2 \cdot 10^{-4}$ generates errors in resulting stresses in the order of $\Delta\sigma \approx 36\,\text{MPa}$, which would also correspond to a shift in the heating cycle of approximately 1 sec.

4.1.1. Thermal System

Thermocouples: An S-type thermocouple was considered suitable for temperature measuring [28]. It consists, on the positive side, of a platinum, 10 % rhodium alloy (Pt10Rh) and on the negative side of nearly pure platinum, both wires in this case having a diameter of 0.35 mm. The useful temperature ranges from 200 to 1500 °C. For detailed specifications of typical thermocouple material combinations see appendix table C.1. The result of every thermocouple measurement is a superposition of the measuring point's voltage and the cold junction voltage (equation 4.2). Other set-ups uses spot-welded thermocouples to a specimen for an ideal contact. This contact point increases the risk of crack initiation. Therfore, in these investigations, the thermocouples were made into a ribbon shape. Both wires were butt welded and compressed to a thickness of $\approx 120\,\mu\text{m}$ over a length of 60 mm and applied to the specimen using a small loading spring. Isothermal tests have shown a higher temperature signal for these thermocouple types (by 20 to 40 K), which indicates a lower heat flux from the specimen volume to the hot junction than occurs in spot welded types. The reason for this is the large contact area and therefore the reduced temperature gradients between specimen and wires, in contrast to the spot welded thermocouple types. Thermocouple aging is not relevant for the temperature range investigated, as the critical level for this effect is above $T_{max} > 1000\,°\text{C}$, figure 4.5.

$$U_0 = U_{Measuring\,Point} + U_{Cold\,Junction} \tag{4.2}$$

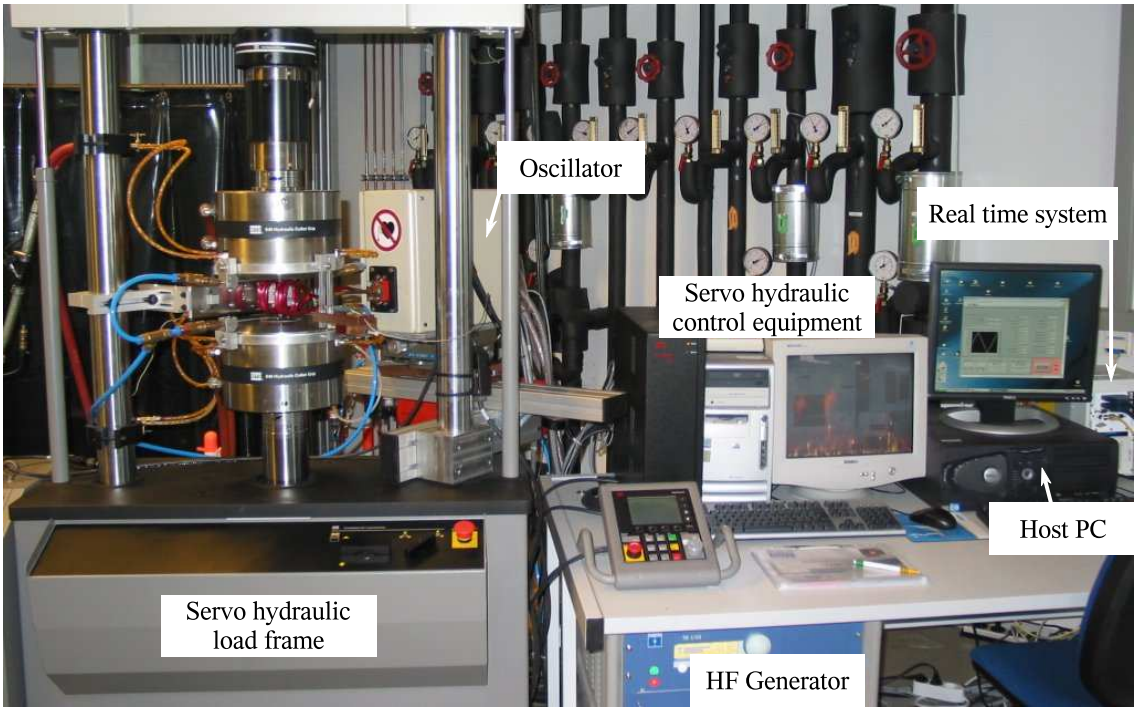

Figure 4.4: The TMF system in a general overview, here conditioned for TMF tests.

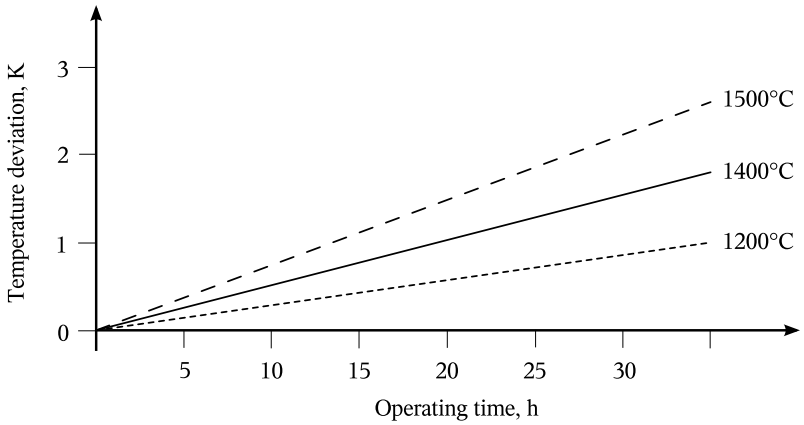

Figure 4.5: Thermocouple ageing effects of S-type wires at temperatures higher than 1000 °C. An altering effect cannot be detected below the critical temperature [99].

Induction Heating System: The heating system is designed to produce a homogeneous and uniform temperature field in the gauge length at each point of the cycle. The required heating rates with good control can only be achieved with an induction system. A typical view of the arrangement around the specimen is shown in figure 4.6. To ensure the required fast transients the use of inductional heating is obvious. Other heating devices, e.g. infrared heating elements cannot be controlled in such an accuracy.

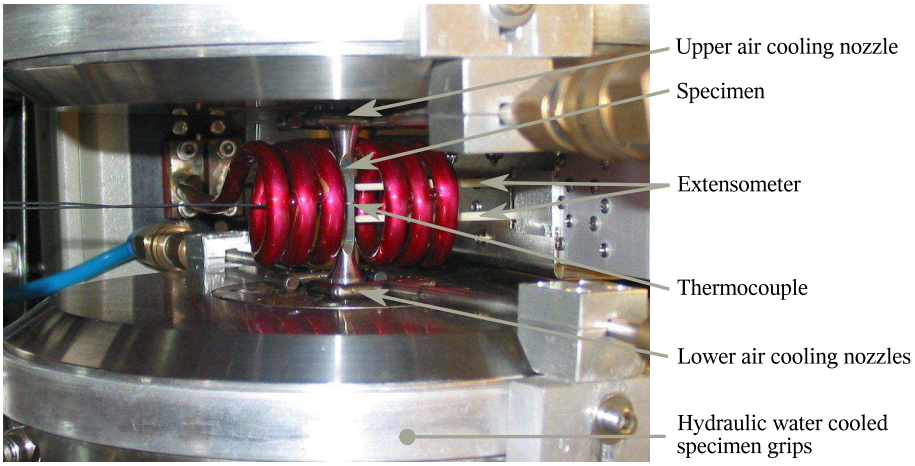

Figure 4.6: Detailed view of a specimen with induction coil, air nozzles, attached extensometer and ribbon type thermocouple on a Nimonic 90 specimen.

One great challenge is the adjustment of the heating coil, as it is a very important part of the system. The final thermal load depends directly on the coil geometry, which influences the electromagnetic field and, in this way, the heat generation within the specimen. Lots of differnet coil designs were manufactured and analysed to point out the most homogeneous temperature distribution. The selected coil geometry ensures an almost constant temperature distribution in the volume and on the specimen surface, where the control thermocouple is applied. Additional tests with instrumented specimens were performed to find the ideal set up for the required heating rates. The temperature is influenced by convection, surface radiation, thermal conductivity, electrical conductivity, induction frequency and specimen geometry. The aim is the minimisation of temperature gradients in the volume of the gauge length. Both factors (geometry and HF penetration depth) have to be tuned for minimised radial temperature gradients [100–102].

Cooling Devices: The second important device is the specimen cooling system. It is the combination of appropriate heating and cooling that results comparable with the real processes. A servo pneumatic valve actuates the cooling system and has to be precisely defined with a nearly linear characteristic voltage – output – flow relation, in order to reduce the control calculations as well as providing stable control algorithms. The compressed air supply reduces variations in the complete air pressure system. Dither, realised by the control software, with a low amplitude, high frequency sine wave applied to the valve spool is used to improve the valve response to low amplitude control signals by reducing sticking.

Filter: S-type thermocouples typically have a sensitivity of 11µV/K. The appropriate filtering of the induced and superimposed signal by the heating device, which is higher than the original temperature signal by a factor of 10^6, is a great challenge. The passive filter used has a low-pass characteristic with a cut-off frequency of 100 Hz, which is related to the maximum theoretical rate of temperature change 100 K/s. Due to the fact that the measured signals are of a very low voltage and the other equipment interferes with the signal, this filter is a combination of two different types, the passive hardware filter and subsequent filtering software.

4.1.2. Temperature Controller

In contrast to other systems, this rig uses a real-time control device *PXI*[2] to control all signals depending on the temperature measurement and subsequent calculations. The combination with National Instruments' LabView[3] brings the system to a high-performance deployment platform for measurement and automation, providing the basis of a very stable, fast and robust control system. The real time algorithm calculates the actual strains

[2] *PXI*: PCI eXtensions for Instrumentation: It is a rugged PC-based platform for measurement and automation systems. PXI combines PCI electrical-bus features with the rugged, modular, Eurocard mechanical-packaging of CompactPCI, then adds specialised synchronisation buses and software features.

[3] *LabView*: A high level graphical programming language from National Instruments, Austin, TX, USA

and forces by the following equations:

$$\begin{aligned} \varepsilon_{thermal} &= \alpha \cdot T + C \\ \sigma &= \frac{F}{A} \\ \varepsilon_{elastic} &= \frac{\sigma}{E(T)} \\ \varepsilon_{mechanical} &= \varepsilon_{elastic} + \varepsilon_{plastic} \\ \varepsilon_{total} &= \varepsilon_{elastic} + \varepsilon_{plastic} + \varepsilon_{thermal} \end{aligned} \tag{4.3}$$

The complete system is characterised by a task sharing structure. Figure 4.7 shows all important procedures and loops running inside of both computers. A summary of the different integrated calculation loops is given in the following sections.

Host PC: One of the most important loops is the graphical user interface, which allows these complex functions to be run with just a few input parameters. A set-up assistant helps to find the correct parameters and calculates any additional inputs required. The backbone of this host PC software is the internal data transfer loop, a shared memory, which collects all measured data and serves them to all other structures. The on-line test analysis tool helps to identify peak values for cycle storage reduction. Test stop sequences for safe shutdown, avoiding additional stresses are also realised by the online analysis tool. The secondary DAQ device allows separate measurement of additional signals as well as superimposed strains for TMF tests in combination with the HCF software module. A network client secures the communication between the host PC and the real-time target. All processes have an internal watchdog, which activates the different shutdown sequences if there are any internal problems detected. An internal webserver is used for access to

status information from outside the test-rig, a summary of the most important test data being shown on a special web page. The web server is able to react in case of triggered interlocks or any other events affecting the test by reporting the current situation via e-mail or text message. The advantage of this separate loop structure is stability without any loss of data. In the case of an internal problem, e.g. wrong DAQ settings, only this loop will be stopped and all the others will get a feedback signal and react accordingly, e.g. by writing all test data to the hard drive in a secure machine shutdown sequence.

Real Time Target: The task dependent loop structure, described above, is also implemented in the real time target, and communication with the host PC is established by a network server. The time-critical process, the temperature controller, runs with the highest priority and is served by the DAQ loop for all the trigger lines as well as all other analogue signals.

To summarise, all time-critical processes run on the PXI side and all test sequences as well as data storage are executed on the host PC.

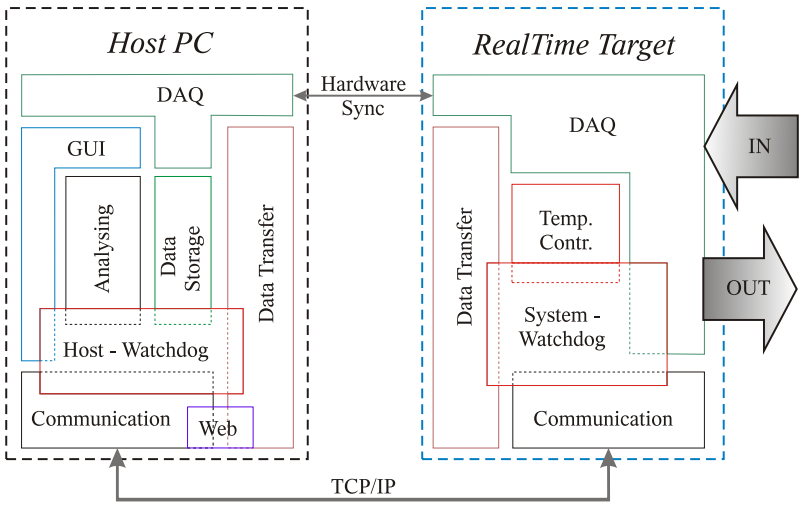

Figure 4.7: Measurement and control signal flow between host and realtime target. The overlapping watchdog structures have the lowest priority but influence any other local loop. Tile structures communicate in both directions.

4.1.3. Verification of Thermal Equipment

The calibration of all thermal measuring components was performed with an infrared thermal camera system *VarioScan 3021ST* with the additional software *IRBIS Pro*[4]. This system affords the possibility of very detailed temperature measurement due to the special scanning set-up. In contrast to commonly used bolometers, this system is characterised by a single high precision sensor. Rotating mirrors generate an infrared radiation matrix and temperatures are calculated and transformed into real thermographic pictures [103]. This system allows a precise and detailed analysis of the data by virtue of the variable emissivity coefficients, which can be set separately for every image region. All thermocouple temperatures were referred to this instrument with an operating and calibrated range from $-40\,°C$ until $1200\,°C$. Infratec GmbH [103] defines the temperature error of the thermographic camera as $\approx \pm 0.03\,K$ under calibration conditions. Figure 4.8 shows the thermal gradients over a specimen surface and in longitudinal and transversal scans during a holding time of $650\,°C$. Important is the homogeneous temperature distribution at the extensometer measurement. For a precise emissivity correction, a special high temperature varnish with a defined emissivity was applied to the specimen gauge length. This varnish emissivity was measured in advance in a seperate calibration furnace.

The reproducibility of the temperature control affects the accuracy of the mechanical strain control, and so temperature control loop optimisation steps are necessary for avoiding instabilities.

The operation of the different devices used in the test rig leads to the minimisation of thermal deviations and is shown in figure 4.9.

[4] *IRBIS Pro*: Special analysing software in combination with the infrared measurement system.

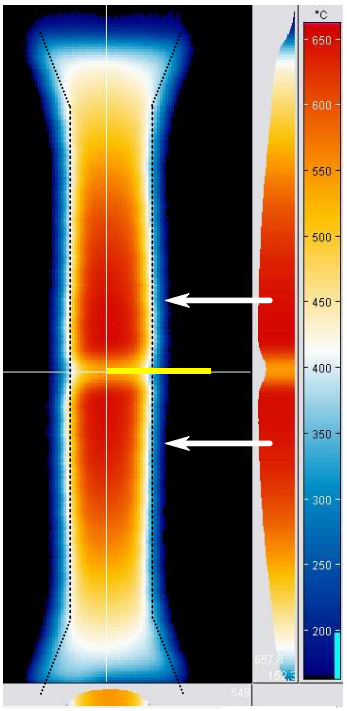

Figure 4.8: Thermal calibration picture of Nimonic 90 at 650 °C with longitudinal and transversal profiles, viewed from the flattened side. The extensometer locations are marked by the white arrows where the temperature gradients are comparatively small. The visible temperature of the thermocouple does not correspond with the image temperature, due to the high reflections at the platinum wires and the different emissivity coefficients. The specimen surface is marked by dotted lines and yellow line presents the thermocouple perimeter. Due to the small dimension of the thermocouple wires it is not shown here.

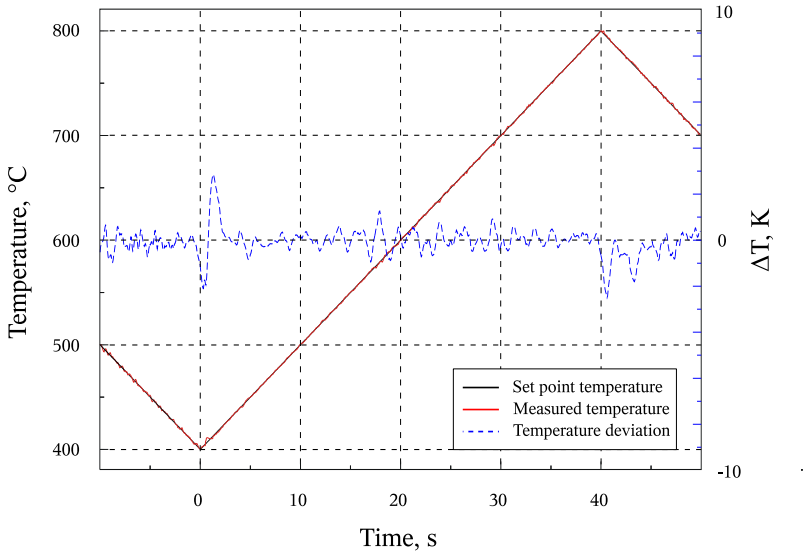

Figure 4.9: Thermal stability of the test rig with during the peak temperatures. The peak values as well as the following overshoot areas are limited to a very small range.

4.1.4. Mechanical Equipment

An MTS[5]test machine, working with a servo hydraulic actuator was used to apply mechanical strains and measure. The maximum applicable force was limited by the load frame to 250 kN. Hydraulic collet grips were used to avoid specimen sliding. This gripping technology leads to good and consistent heat transfer between the specimen volume and the grips. Due to the water cooling system of the fixation, the specimen gripping volume has almost the same temperature gradient along it during a temperature cycle.

The test machine was programmed by its own system software, *MPT*[6]. For this application, a combination of load and displacement control was implemented. The data connection with the thermal controller was realised by analogue interfaces and digital trigger lines. All test-related data were sent to the PXI to be handled with an equivalent time base.

Specimen alignment was investigated using a three dimensional deformation measurement system *Aramis*[7]. A round specimen surface was speckled by a stochastically distributed pattern for the system internal calculations, which are based on the Euclidean displacement, the apparent distance between given points calculated from equations 4.4. The specimen surface was marked by three parallel lines, each with 55 data points, see figure 4.10. Plot 4.11 shows that the displacement behaviour was the same for all measurement points along all three lines for a range of fixed loads at room temperature. This shows, the mechanical equipment to be well aligned not producing any bending moments in the specimen [105].

[5]MTS: Material Test Systems 810 from MTS Systems Corp., Minnesota, USA (250 kN load frame with TestStar IIs Controller)

[6]*Multi Purpose Testware* is a programming tool for any application of servo hydraulic testing machines. Every test set-up is freely programmable for an interaction with analogue and digital external signals [104].

[7]ARAMIS 3d deformation measurement system, GOM mbH, Braunschweig, Germany

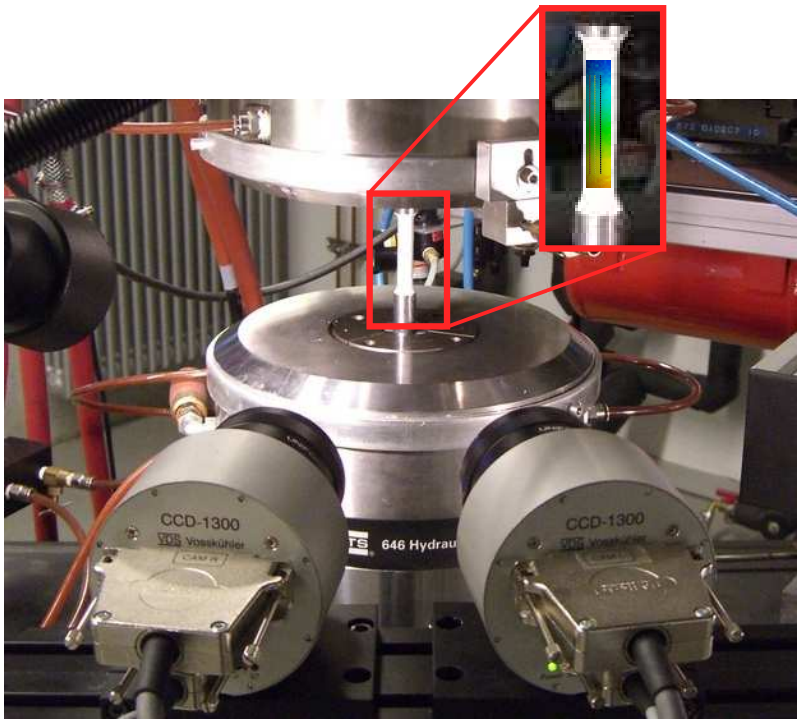

Figure 4.10: The alignment of the setup was checked by an optical deformation measurement system using constant incremental load steps and analysis of the three dimensional deformation.

$$\begin{aligned} d(x,y) &= |x-y| = \|x-y\|_2 \\ &= \sqrt{(x_1-y_1)^2+\cdots+(x_n-y_n)^2} \\ &= \sqrt{\sum_{i=1}^{n}(x_i-y_i)^2} \end{aligned} \tag{4.4}$$

4.2. Test Conditions for TMF and Creep Tests

4.2.1. TMF Test Procedure

TMF tests simulate the sequential start-up and shut down of an engine. In this work a cycle is considered as such an on-off sequence. The main damage mechanisms occur during these phases and not during steady state conditions. Therefore, the operating time at constant mechanical loadings and temperatures is not included in these investigations.

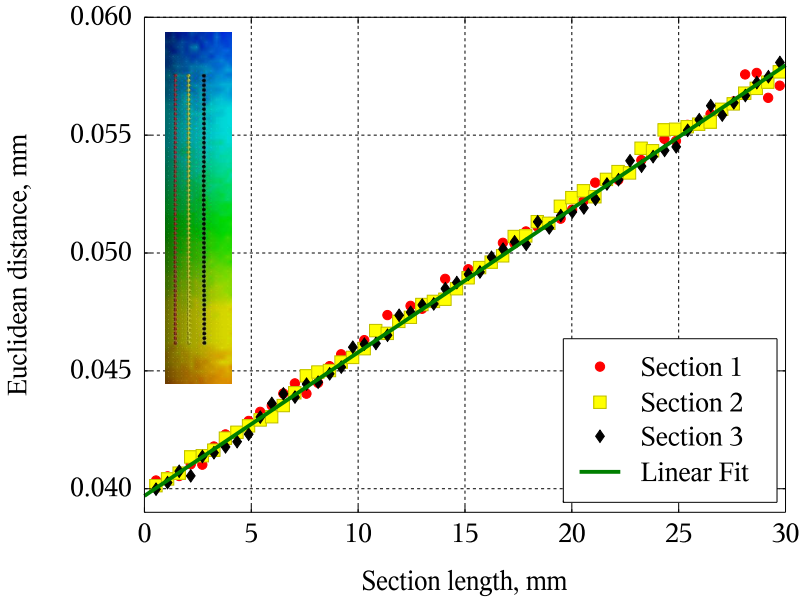

Figure 4.11: Alignment measurement results. The Euclidean vector for each point was calculated to give surface displacements.

TMF Pretests

Due to the great influence on the TMF cycle shape and its relevance to the service conditions, this work deals with the phase shift $\varphi = -135°$ between the mechanical strain and temperature, which represents the highest stressed material of the leading edges of turbine blades, see figure 2.3. The peak mechanical strains are of equal magnitude in these tests ($R_\varepsilon = 1$) and heating and cooling rates are fixed to 10 K/s. The temperature was cycled between 400 and 850 °C to encompass the ductile-brittle-transition and to give results wich can be compared with other works [28]. The high rates of temperature change require a very complex set of control actions to realise the cycle shape. Pretests were necessary to determine the thermal expansion and the temperature dependence of the Young's modulus. The accuracy of both results was checked by the zero stress test, figure 4.12.

The pretests was performed in three steps. First, the temperature of a specimen was cycled in load control mode ($F = 0$) to measure thermal expansion within a temperature range from $T_{min} - 50\,\mathrm{K}$ to $T_{max} + 50\,\mathrm{K}$ with temperature transients similar to those in test cycling. The thermal elongation can be considered as linear between two data points ($\Delta T \approx 1\,\mathrm{K}$) and strains were calculated by a linear interpolation between both data sets

in the following test processes. The second step was the measurement of the temperature dependency of Young's modulus. Here the specimen was heated in increments of 50 K and held at each temperature for ≈ 30 s to ensure a homogeneous temperature distribution in the gauge volume. After this holding, time a defined stress ($\sigma < 20\,\%$ of the yield stress at T_{max}, [2]) was applied and the resulting mechanical strain, compensated by the thermal strain at this temperature, was calculated using equations 4.3. The final pretest step checked the values obtained by the Zero-Stress-Test, and was carried out under strain control. This can be regarded as a benchmark for the complete set-up and the pretest results. Additionally, it shows the accuracy of the active thermal strain compensation and its reliability during cycling. This final pretest was run in strain control mode at $\varepsilon_m = 0$ and the resulting total strain, used as the command value for the machine, is equivalent to the thermal strain ($\varepsilon_{tot} = \varepsilon_{th}(T)$). All other conditions were comparable to the subsequent main TMF test. This part of the pretest is of the most importance to the final TMF test results because it measures directly the control over thermal strain achieved in the test set-up [6].

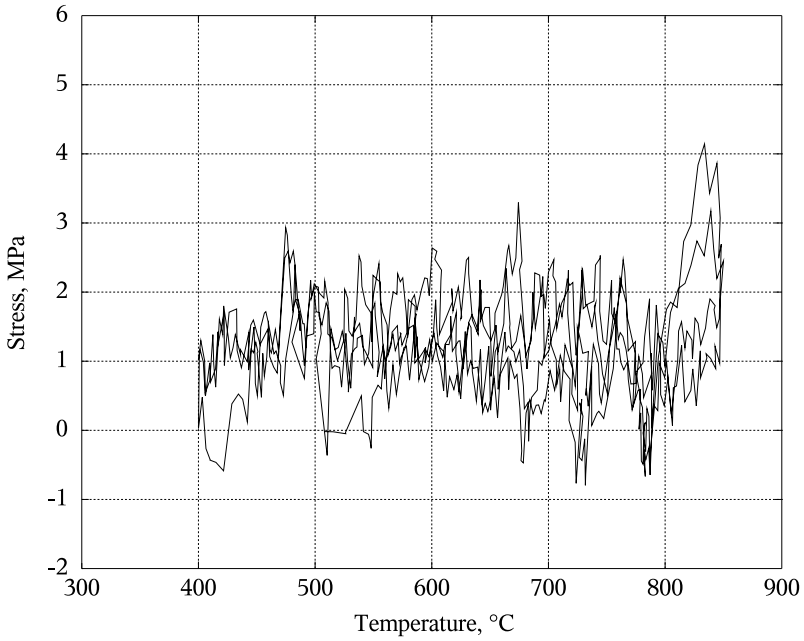

Figure 4.12: Accuracy of the temperature controlling equipment as shown by one cycle during the zero stress test. The suggested limit of 5% of maximum stress by Hähner et al. [2] leads under the applied conditions of these tests to a maximum allowed zero-stress-test amplitude of ± 20 MPa.

of constant

Main TMF Tests

After the pretest procedure, the main test needs to start quickly to avoid additional stresses caused by cooling down. Based on the pretest results, the preset strain control modes will be activated and the corresponding setpoint strains calculated. By agreement with other laboratories, the main tests were started either with $\varepsilon_m = 0$ or in the compression direction, so the required launch sequence, including the exact time point for the switch of the control signal, was also calculated.

4.2.2. Conditions for TMF Tests

Both types of nickel base superalloy were loaded with varying temperatures and different mechanical strains. Failure was defined as the number of cycles at which the peak cycle tensile stress dropped below 10 % of its maximum value from the whole test. A complete list for the test parameters used can be found in table 4.1.

Nimonic 90: One test was used as a benchmark for the complete set-up to verify the accuracy and the comparability of the lifetime results with other workers, and this involved an in-phase test (phase angle of $\varphi = 0°$) and a rate of change of temperature of $\dot{T} = 5\,\mathrm{K/s}$. The applied mechanical strain amplitudes for the TMF tests varied from 0.25 % to 0.7 %. Apart from the IP test, the phase shift for all investigations was constant at $\varphi = -135°$. In order to compare the effect of a positive mean strain with the PM 1000 investigations, one test was performed with a mean strain offset of 0.75 % and a strain amplitude of 0.5 %. This mean strain offset value was chosen to correspond to the thermal elongation at the mean temperature of the cycle ($T_{mean,cycle} = 625\,°\mathrm{C}$).

PM 1000: The TMF tests on PM 1000 were also performed under mechanical strain control with a positive means strain offset at amplitudes ranging from 0.05 % to 0.4 %. Because of to the high stresses and the specimen geometry this was necessary to avoid buckling. As before, phase angle between the mechanical strain and the thermal cycle was constant at $\varphi = -135°$. The temperature was cyclically changed between 450 and 850 °C with a rate change of $\dot{T} = 10\,\mathrm{K/s}$, in accord with other investigations [18, 21, 23, 106]. The positive mean strain allowed crack propagation to be investigated the value of 0.75 % coinciding with the thermal elongation at 650 °C, the mean temperature of this cycle.

Under these conditions, a comparison can be carried out for the single phase shift of $\varphi = -135°$ between Nimonic 90 and the effect of mean strain for PM 1000.

Table 4.1: TMF test conditions for the nickel base superalloys investigated. Tests were started at $\varepsilon_m = 0$ in compression direction.

Type	Material	Parameter	Value	Unit
IP	Nimonic 90	Phase Shift	0	°
		Temperature rate of change	5	K/s
		Temperature	400 … 850	°C
		Mechanical strain amplitude	0.7	%
		Mean strain	0	%
TMF	Nimonic 90	Phase Shift	-135	°
		Temperature rate of change	10	K/s
		Temperature	400 … 850	°C
		Mechanical strain amplitudes	0.5	%
		Mean strain	0.75	%
TMF	Nimonic 90	Phase Shift	-135	°
		Temperature rate of change	10	K/s
		Temperature	400 … 850	°C
		Mechanical strain amplitudes	0.25 … 0.7	%
		Mean strain	0	%
TMF	PM 1000	Phase Shift	-135	°
		Temperature rate of change	10	K/s
		Temperature	450 … 850	°C
		Mechanical strain amplitudes	0.05 … 0.4	%
		Mean strain	0.7508	%

4.2.3. Conditions for Creep Tests

To investigate the creep behaviour of the NiAl material, it was necessary to modify the TMF test rig. Figure 4.14 shows the additional characteristic components including the optical deformation measurement as well as the special heating equipment. Due to the very small test volume, direct induction heating cannot achieve temperatures of more than 370 °C in the specimen. A special set-up was arranged using the radiation from four pure nickel plates, heated up inside the electromagnetic field, thus ensuring a constant additional heat flux to the specimen. The thermocouple for temperature control was centred between the heating plates and on the gauge length. The loads were applied by hanging calibrated masses to the lower end of the specimen. A window between the nickel plates allowed for continuous image acquisition during the test. Ceramic surface markers were used to provide an optical image analysis and subsequent strain calculation. The frame-grabbing rate was set to 0.1 $^{\text{frames}}/_{\text{sec}}$ initially and decreased later to 0.1 $^{\text{frames}}/_{\text{min}}$ at each test. Additionally two LVDTs measured the complete specimen elongation between the grips and were used for a controlled shutdown of the test system. Homogeneous thermal conditions could be achieved with a maximum allowed temperature deviation of $\Delta T \leqq \pm 5$ K. Figure 4.14 shows a detailed view of the experimental set up.

Because of the limited number of three specimens, the tests were carried out with an incremental increase in load, each step increase being applied after the first creep rate minimum. Thus, whereas creep rates could be determined, creep fracture life could not be measured in this experiment.

After the test, the greyscale images (figure 4.13a) were cropped around the region of interest, arranged into multiple parts and transformed into binary image modes separately with the Jarvis-Roberts algorithm [107, 108], which finds the brightest and the darkest parts of a picture and calculates a local threshold value. The advantage of this method is a robust calculation and a precise identification of markers, even those which became detached during the test. After the the transformation in a binary image mode two other algorithms filled small holes of incorrect identification and cleaned the marker areas [105].

The geometrical center indicates the reference point for each marker, figure 4.13b.

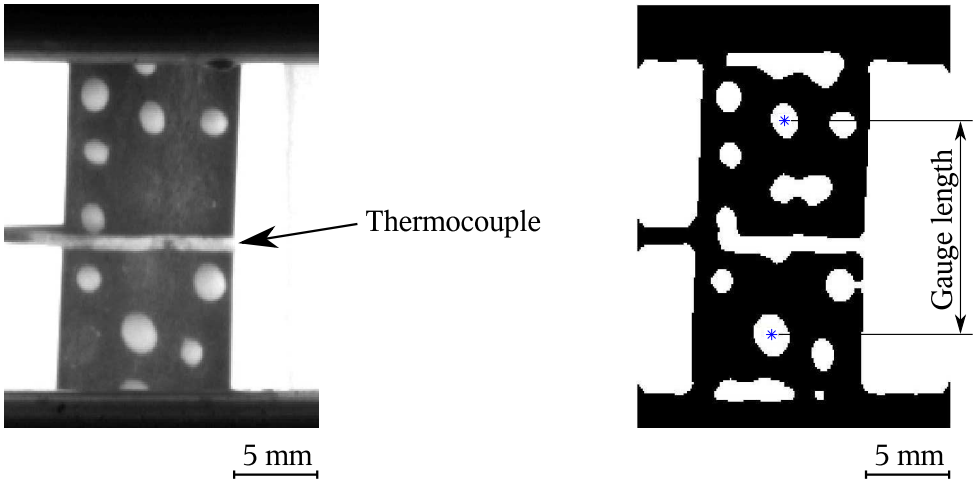

(a) Cropped greyscale image, directly captured by the CCD camera.

(b) Binary image, including the geometrical moments of inertia.

Figure 4.13: Image preparation for the strain analysing procedure of creep experiments.

Due to the small number of grains through the thickness, thickness can be considered as constant during the test. This assumption allows the boundary condition of constancy of volume to be used to recalculate true stresses, see equation 4.5, where V represents the constant test volume between two selected markers, w stands for specimen width, t for thickness and l for the distance between centeroids of the selected markers. The index i represents individual images within a test series.

$$\begin{aligned} V = const. &= l_0 \cdot w_0 \cdot t \\ &= (l_0 + \Delta l_i)(w_0 - \Delta w_i)\, t \end{aligned} \tag{4.5}$$

With $\Delta l_i = l_0 \cdot \varepsilon_i$ and $V/t = l_0 \cdot w_0$ from equation 4.5 the width reduction can be calculated from equation 4.6, and hence the true stress σ_{eff} from equation 4.7.

$$\begin{aligned} \frac{1}{w_0 - \Delta w_i} &= l_0 + \Delta l_i \\ w_0 - \Delta w_i &= \frac{w_0}{1+\varepsilon} \end{aligned} \tag{4.6}$$

$$\begin{aligned} \sigma_{eff,i} &= \frac{F}{(w_0 - \Delta w_i)\,t} \\ &= \frac{F\,(1+\varepsilon_i)}{w_0 \cdot t} \end{aligned} \tag{4.7}$$

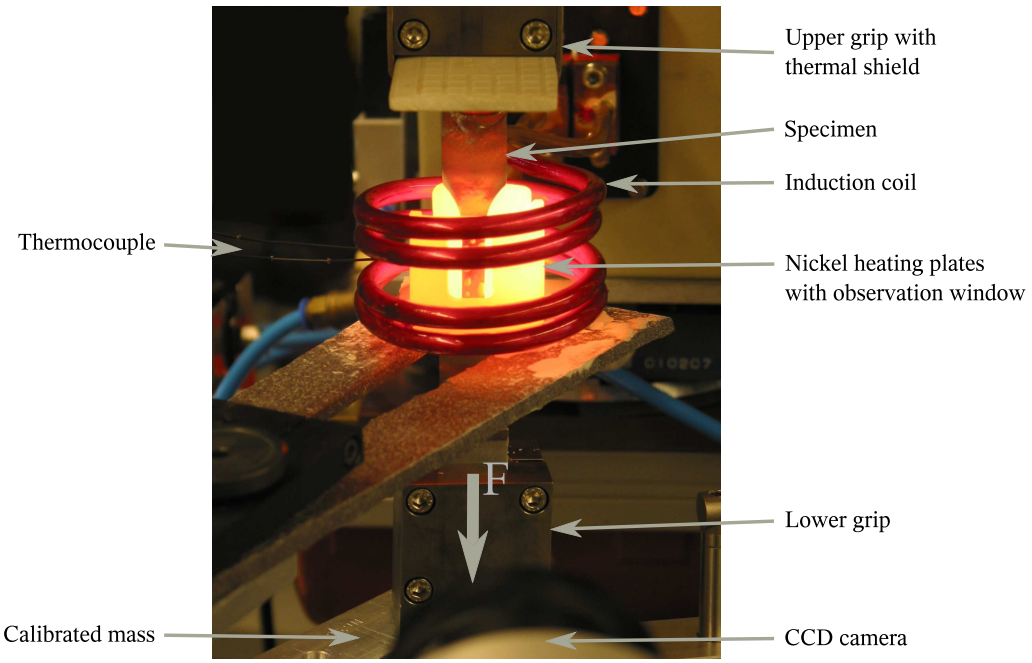

Figure 4.14: The modified TMF test rig, used for the creep investigations. An observation window in the front heating plate is used for optical access to the markers. The CCD camera is positioned perpendicularly to the specimen surface at the front. The ribbon type thermocouple (marked) is directly centred to gauge length.

The test conditions for the NiAl creep specimen are summarised in table 4.2. The temperature was fixed at 800 °C and the initial applied stresses were calculated to be 40, 80 and 103 MPa. To analyse the data, measured points will be fitted by a polynom of 5th degree or more, to ensure stable conditions for the following derivation, needed for

the strain rate calculation.

Table 4.2: Creep conditions for NiAl.

Material	**Parameter**	**Value**	**Unit**
NiAl	Temperature	800	°C
	Stress levels	40, 80, 103	MPa

5. Results

This chapter is devided into three main sections. First, the TMF results on the two superalloys are presented, followed by a description of the metallographic results. Finally, the creep and microstructural results for NiAl are given. Comparison of results with those of other workers is only introduced where this can be made directly and detailed discussion is deferred to the next chapter.

5.1. Thermal Mechanical Fatigue

Both material types were subjected a series of different mechanical strain amplitudes to observe the differences in lifetime between powder metallurgical and conventional nickel based superalloys. Generally, the number of cycles to failure will be reduced by increasing the strain amplitude. Figure 5.1 summarises the results of all the combinations investigated, and the corresponding literature data. The IP test of the Nimonic 90, shown by the symbol (★), is used as a benchmark to verify the results quality with those of other investigations as well as other conditions of stress and cyclic behaviour. The Nimonic 90 IP range (horizontal bar) is a result of the COST project and has been reported by Marchionni et al. [109]. This project was established to analyse and compare TMF data from all TMF performing European institutes, and, as can be seen, the range of results of the project partners cover, from ≈ 300 to nearly 1100. Marchionni et al. [109] have also reported fatigue curves for Nimonic 90 IP (red line) and OP (green line). It is evident, that the Nimonic 90 phase shifted tests in the current study (blue line) show nearly the same slope as the OP tests and are much closer to the OP curve than to the IP curve.

The influence on the lifetime of an superimposed tensile mean strain was investigated for Nimonic 90 for the same mean strain level as was used for the PM 1000. A dramatic reduction (by a factor of about 3) was observed in the number of cycles to failure of Nimonic 90 at a strain amplitude of $5 \cdot 10^{-3}$. It is expected that the anomalously high slope of the curve for PM 1000 compared to the OP and IP curves of Ngala et al. [18] are attributable to the non-zero mean strain and that of the curves (including those for Nimonic 90) would show an increased slope at non-zero mean strain. The remainder of this section considers the detailed results, firstly for the pre-tests and validation of the set-up, then for the Nimonic 90 and finally for the PM 1000. In general, all hysteresis diagrams given in this chapter consist of one of the initial transient cycles, a mid-life saturation cycle and one cycle close to the failure.

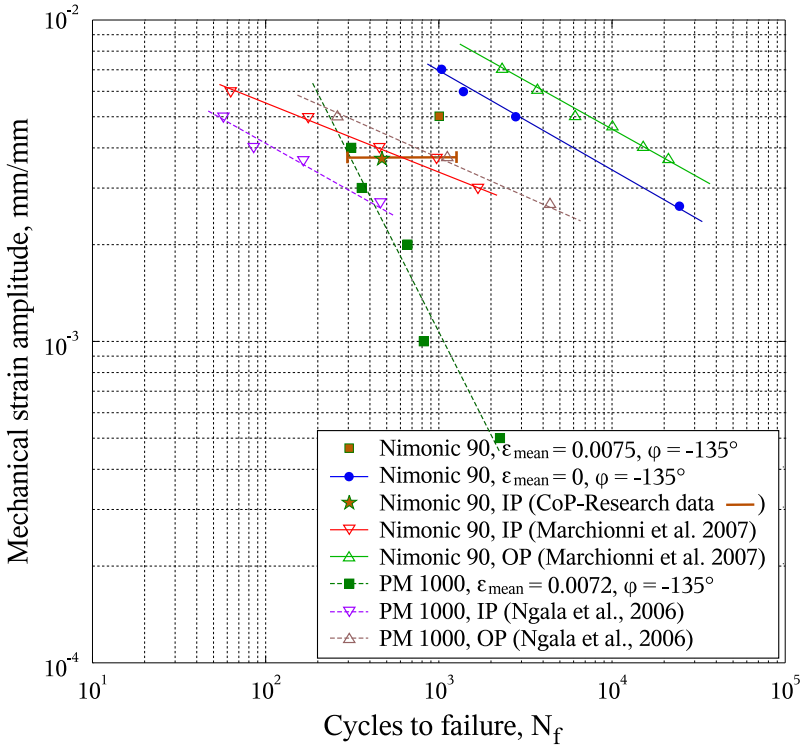

Figure 5.1: Cycles to failure of both alloys investigated (PM 1000 and Nimonic 90) under thermal mechanical fatigue loading. Open symbols correspond to literature data. The PM 1000 IP and OP tests were investigated by Ngala et al. [18] and the Nimonic 90 IP and OP results came from the Standardisation Project partners [23, 109, 110].

5.1.1. Experimental Set-up

Figure 5.2 shows the superposition of the demanded mechanical strain (solid line in figure 5.2a) and the thermal strain (dotted line in the same diagram) calculated from equation 2.4 for three different cycles. As indicated earlier the tests start at the time point where the mechanical strain $\varepsilon_m = 0$ moving in the compression direction of the hysteresis, in order to avoid additional tensile stresses on the specimen. The blue solid line (cycle 1) shows this behaviour at the beginning of the test, where $\varepsilon_m = 0 = \text{const.}$ with increasing temperature in the first $\approx 11\,\text{s}$. The corresponding total strain (the test rig output signal) only consists of thermal strain, due to thermal expansion (increasing blue line in figure 5.2b), illustrating the importance of starting the test in this way. Both diagrams generally show the extraordinarily stable long time precision of the testing system, with small variations only being present in the first cycle. The same stability was observed even for the long term tests with more than $25,500$ cycles as shown in the cycle-time plot (figure 5.6). Except for some minor hardening in the first few cycles the actual stresses appear sufficiently constant during the whole experiment.

5.1.2. Nimonic 90

Pretest

The pretests for Nimonic 90, described in section 4.2.1, showed a non-linear correlation of thermal elongation with temperature, figure 5.3. The temperature dependence of the Young's modulus could be linearly approximated, figure 5.3, but the online temperature-dependent calculation is not based on a curve fit of the whole experimental interval, typically used in other test equipment [11, 111]. Rather the actual thermal strain as well as Young's modulus were calculated incrementally using a linear interpolation of 1 K for the thermal strain and 50 K (or lower, depending on the requirements) for the elastic part of mechanical strain. Due to the small linearisation steps, the results for both variables are very precise without any inhomogeneities. The preliminary heat treatment ensured

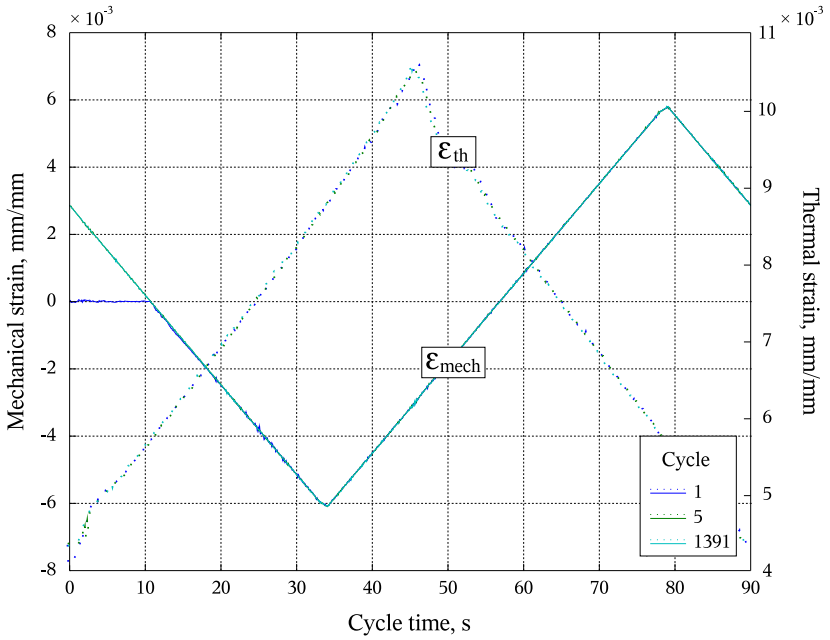

(a) Recalculated from the measured data: actual thermal strain ε_{th} and mechanical strain ε_m as the control signal.

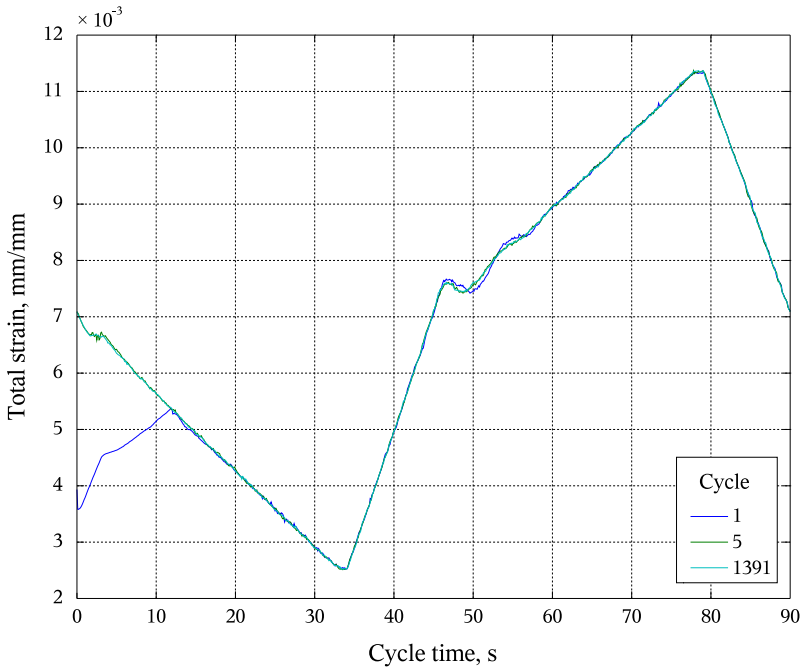

(b) Resulting total strain during a cycle as the superposition of both curves of 5.2a.

Figure 5.2: Stability of control parameters for cycles 1, 5 and 1391 with applied strain amplitude of $\Delta\varepsilon_m = 0.6\,\%$ for Nimonic 90. Variables: measured total strain (b) and temperature.

no influence of microstructure during the pretest procedure, which can be considered as homogenous [68].

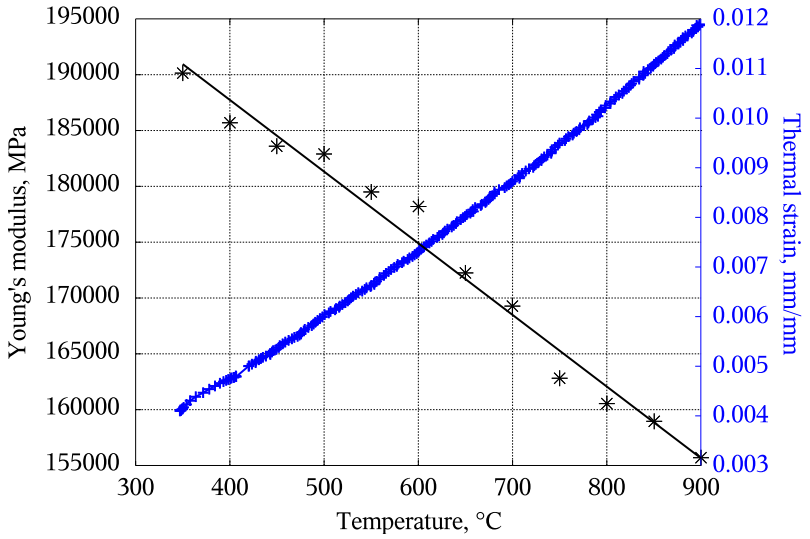

Figure 5.3: Pretest for Nimonic 90: temperature dependent Young's modulus and thermal elongation.

Cyclic Deformation Behaviour

TMF lifetime behaviour of nickel base superalloys follows the principal mechanisms of fatigue and creep. It can be separated into the following general stages: the initial transient region, which consists of a hardening and a softening part, the saturation zone, including the predefined failure criterion, and the final crack propagation part. Figure 5.4 shows the four stages of hardening, softening, saturation and failure for one example of a Nimonic 90 specimen. The cyclic deformation behaviour of Nimonic 90 is summarised in figure 5.14 for the in-phase test and the phase shifted investigations. A mean compression stress level can be observed, caused by high temperatures at the tensile sequence of the cycle. During the heat increasing, the applied mechanical strain induces high plastic deformations. The decreasing Young's modulus and the given mechanical strain leads to a shift between plastic and elastic strains according to equation 5.1, resulting in higher plastic deformations. At reduced temperatures during a cycle these accumulated strains cannot be dissipated completely and therefore induce much higher compression stresses

by reaching the required mechanical compression strain values, resulting in an increasing plastic strain.

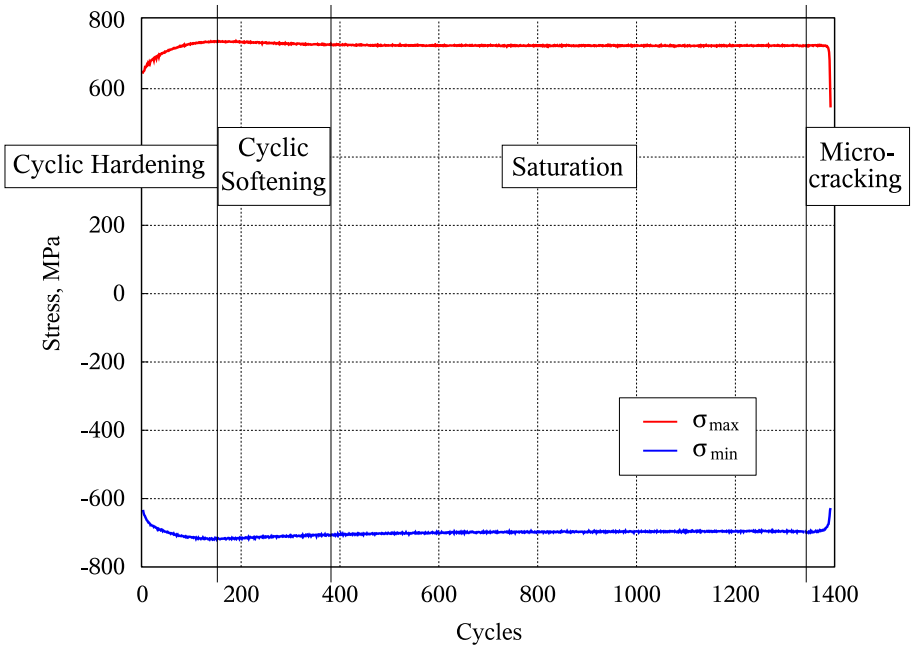

Figure 5.4: Cyclic loading deformation curve of Nimonic 90 for a mechanical strain amplitude of $\Delta\varepsilon_m = 0.6\,\%$, showing cyclic hardening at the beginning, followed by cyclic softening and saturation with crack formation and propagation.

$$\varepsilon_m = \frac{\sigma}{E(T)} + \varepsilon_{pl} \tag{5.1}$$

An overview of all the mechanical strain amplitudes investigated is shown as a function of temperature in figure 5.5. The shape is closely related to the real service conditions of turbine blades, figure 2.3, and can be seen as the "input" hysteresis.

Figure 5.6 demonstrates the cyclic behaviour during the long-term test with $\varepsilon_m = 0.25\,\%$. The shift of induced stresses is marked by the grey arrow (cyclic softening), attributed to the low applied mechanical strain amplitude and the quasi-stationary dislocation structure.

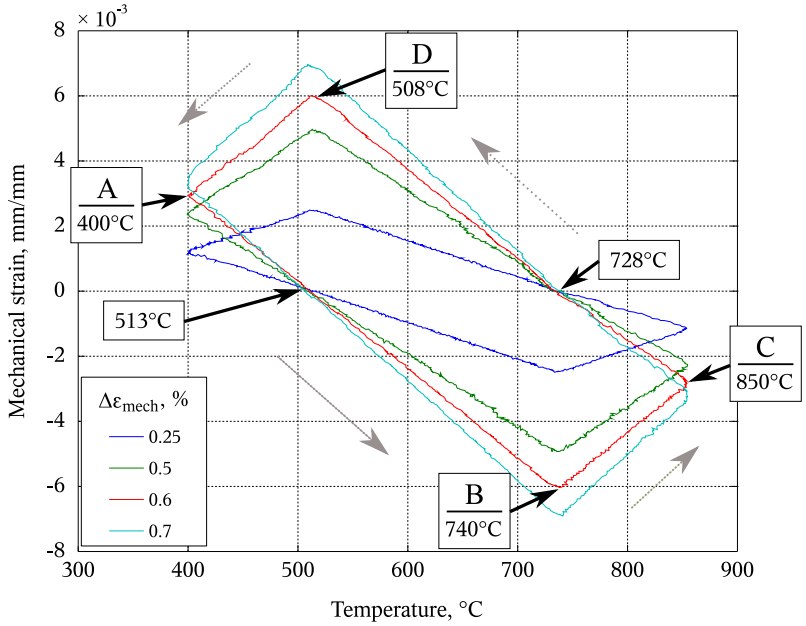

Figure 5.5: Mechanical strain vs. temperature cycle as the input signal with respect to varying mechanical strain amplitudes. This shape is closely related to figure 2.3. The cycle starts at "A" in compression direction with heating up, reaches point "B" at highest compression loads. "C" is the peak temperature before cooling and "D" is the maximum of mechanical strain in tension. The mechanical strain was applied in compression direction at a temperature of 513 .

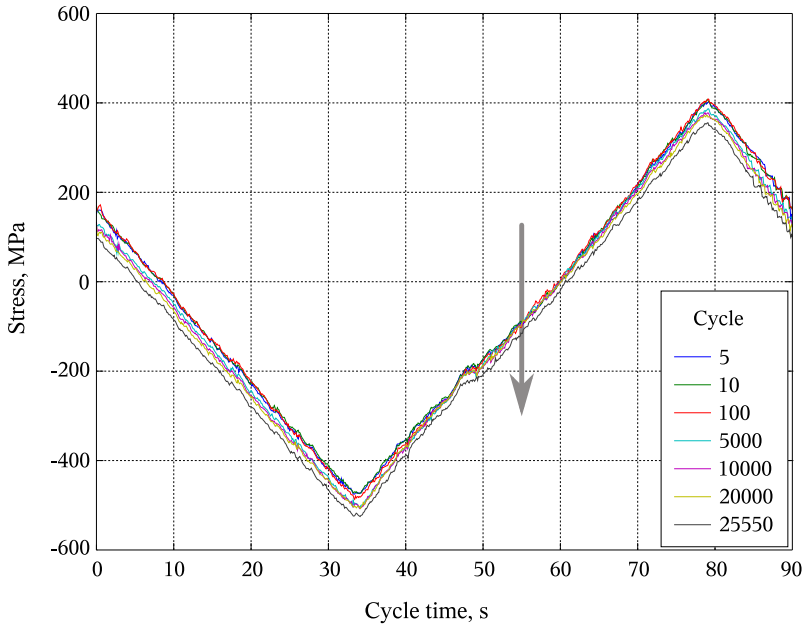

Figure 5.6: Stress vs. cycle time for the Nimonic 90, $\varepsilon_m = 0.25$ %, long term test. The resulting stress levels are saturated after ≈100 cycles. After the first 100 cycles the hardening effect is finished, follows by a continuous shift to compressive hardening and tensile softening, respectively.

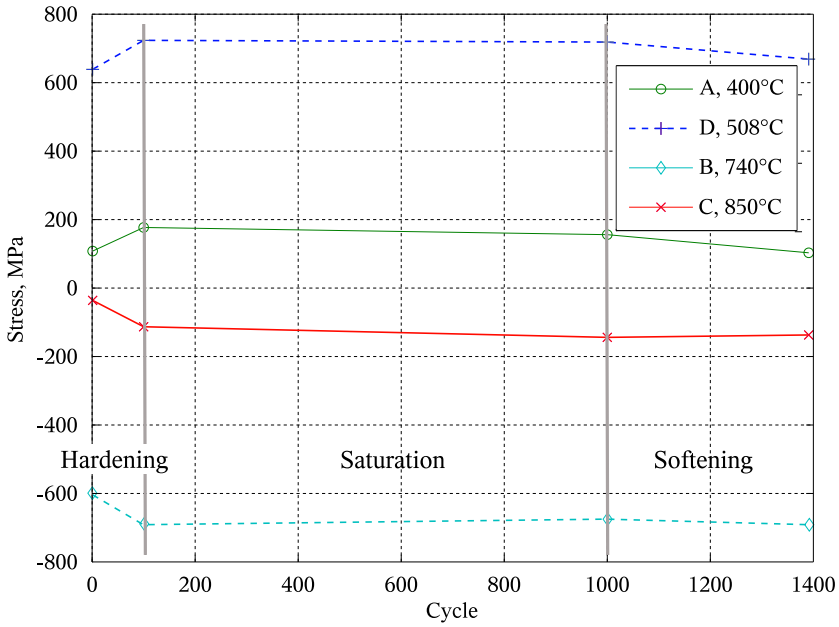

Figure 5.7: Development of peak stresses at the important temperatures (A - D) of Nimonic 90 for a mechanical strain amplitude of $\Delta\varepsilon_m = 0.6\,\%$.

Initial Transient Region

Due to the solution annealing of 850 °C at 5 hours to reduce the dislocation density, the first few cycles of each test show typical work hardening effects, as the dislocation density builds up. Figure 5.9b shows the plastic strain development for Nimonic 90 at mechanical strain amplitude of $\varepsilon_m = 0.6\,\%$. In both the tension and compression part of the initial cycle the sample requires less stress for a given plastic strain. Comparing the loop shapes, a move to higher plastic deformations for of the first few cycles of the test at z - z ($\varepsilon_{pl} = 2x10^{-3}\,\%$ can be observed. y - y is characterised by compression softening for cycle 100 and 1000. The line x - x shows the similarly behaviour, a tension hardening with higher tensile stresses for the same plastic strain amplitude. The resulting peak stresses at the most important temperatures (marked with A - D in figures 5.5 and 5.9) are plotted in figure 5.7.

Figure 5.8 shows the initial hardening of the different investigations acc. equation 5.2. Amplitudes smaller than $\Delta\varepsilon_m = 0.5\,\%$ leads to small influences of this ratio. The diagram shows the limitations of these tests. Below applied mechanical strains of

$\Delta\varepsilon_m = 0.25\,\%$ the resulting hardening effect is very small. leading to extensive long cycle numbers. At the other direction, large amplitudes leads to increased cyclic hardening effects, attended by reduced cycles. Equation 5.3 summarises the observed data. The coefficient of determination is $R^2 = 0.99$.

$$\text{Hardening Ratio} = \frac{\sigma_{max}}{\sigma_0} \tag{5.2}$$

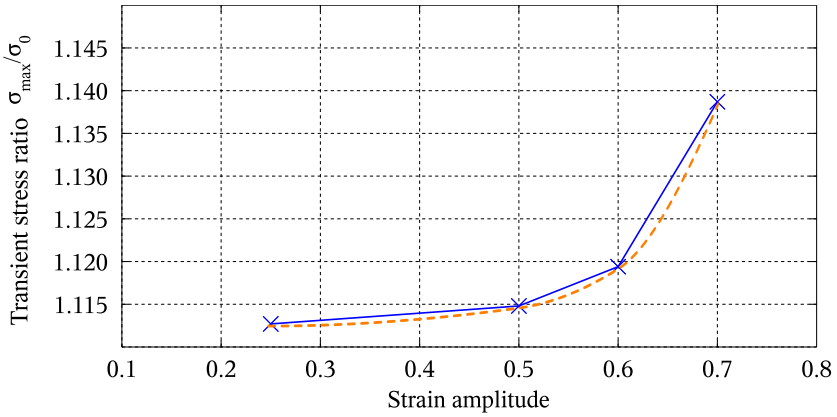

Figure 5.8: Ratio of transient and initial stresses at varying strain amplitudes for Nimonic 90 phase shifted tests, and without additional applied strain. The dotted line represents the fit.

$$\text{Hardening Ratio}\,(\varepsilon) = -0.98 + \left(\frac{\varepsilon}{5.66}\right)^{0.01} \tag{5.3}$$

Saturation Region

Due to the complex saturation behaviour the results will be divided into the three investigated loading series, the phase shifted tests with different mechanical strain amplitudes, the in-phase test and the phase shifted test under offset conditions.

Phase shift of $\varphi = -135°$, varying ε_m

After the transient region, the stress response stabilises at a certain level, when most of the plastic deformation caused by dislocation multiplication and reorganisation in the bulk

material is finished. This behaviour can be seen by examining the peak stress values at point A and D in figure 5.9b.

The hysteresis loops of the first (incomplete) cycle, two midlifetime cycles (No. 100 and No. 1000) and the close to last cycle (No. 1391) are shown in figure 5.9a. This diagram is characterised by a shift of the compressive stress peaks to higher values between the first and hundredth cycles, after which the peak drops a little. On the tension side, there is a similar increase between the first and the hundredth with little change between the 100^{th} and the 1000^{th} cycles.

The turning points of these hysteresis are the peaks of the mechanical strain cycle. Except for the first and the last few cycles, the plastic deformations have equal shapes. The tension stresses reach nearly the same levels in tension and in compression for one cycle.

In-phase conditions

The in-phase hysteresis is characterised by smaller hysteresis area during the transient and saturation zones. In the crack propagation regime the area and the shape is changed, figure 5.10. At the beginning of the test the resulting stresses are shifted to compression. One of the final hysteresis is also plotted in this figure, where creep effects under tension are observable (cycle 550). Horizontal shapes are usually based on creep effects during cyclic loadings at this diagram type.

Phase shift with strain offset $\varphi = -135\,°$, $\varepsilon_{mean} = 0.75\,\%$

The hysteresis curve figure 5.11 is affected by creep under compression loadings throughout the whole lifetime, a behaviour also observed for the PM 1000 tests. The creep effect can be seen by examining the plastic deformation hysteresis as a function of temperature, figure 5.12. As the temperature is increased from its minimum, the imposed phase phase shift makes the plastic strain decrease initially and the increases sharply until the given mechanical peak value at which it and is much higher than the thermal elongation. After

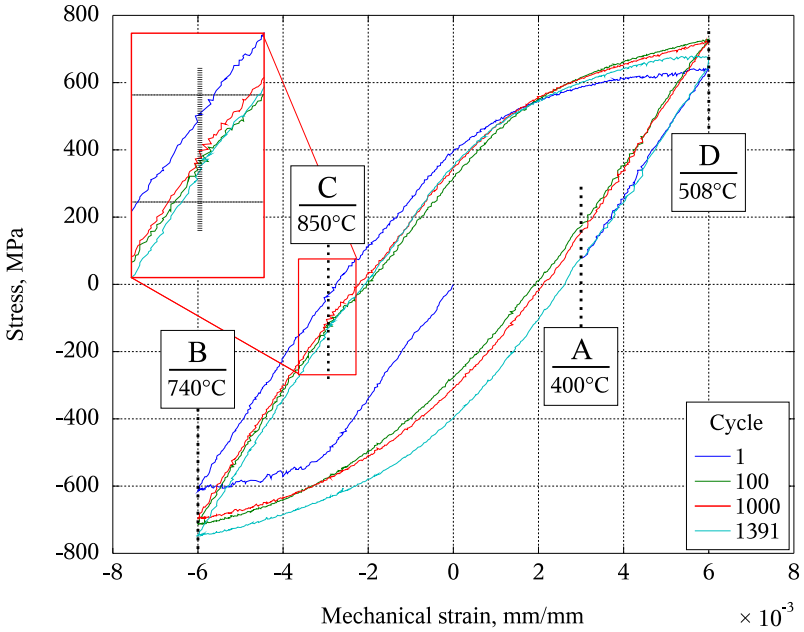

(a) Hysteresis loops for Nimonic 90 with an applied strain amplitude of $\varepsilon_m = 0.6\,\%$. During the first few cycles the cyclic hardening leads to higher tension and compression stresses. After this hardening the hysteresis loops are similar until the end of the test, where the tension stresses decrease, mostly related to crack initiation. The values of 850 °C are magnified at the left upper box.

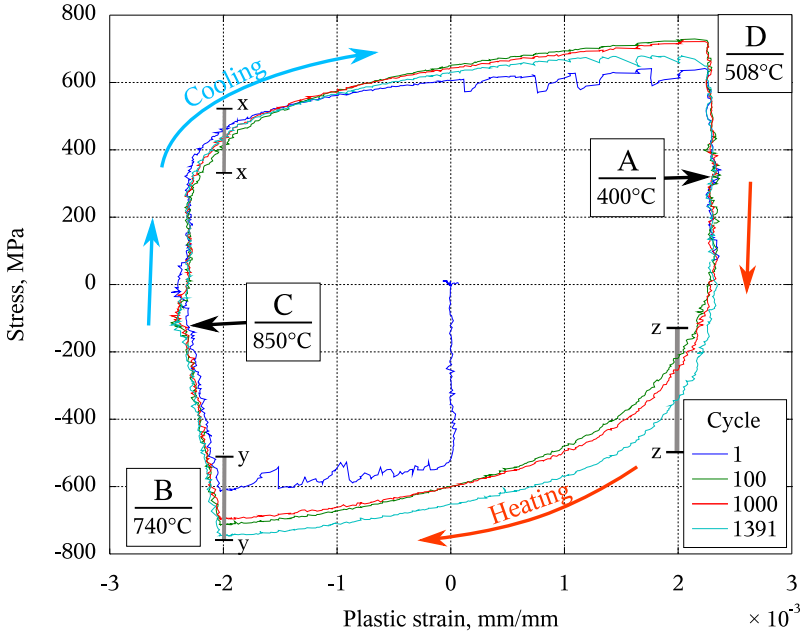

(b) Plastic strain development for Nimonic 90 with a mechanical strain amplitude of $\varepsilon_m = 0.6\,\%$, showing permanent cyclic hardening in compression mode. The tension part shows also a cyclic hardening for the first few cycles.

Figure 5.9: Stress vs. plastic and mechanical strain $\Delta\varepsilon_m = 0.6\,\%$ for Nimonic 90.

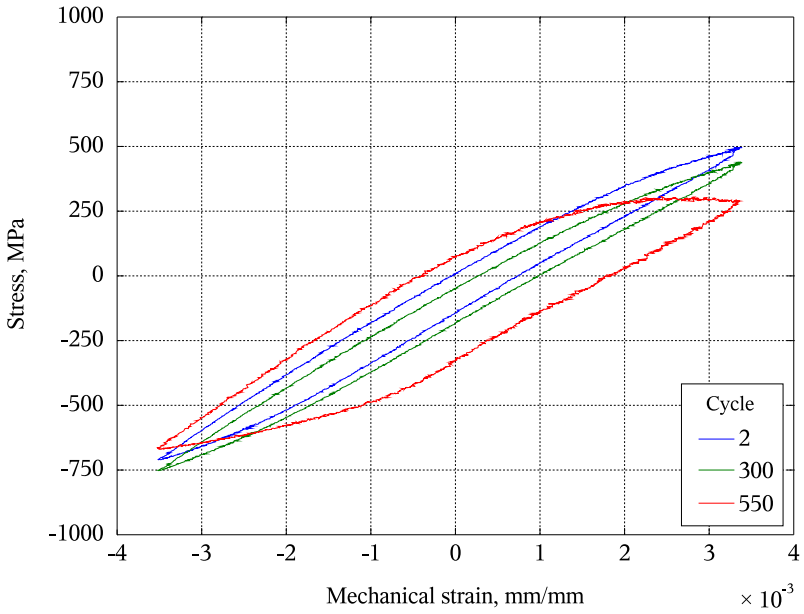

Figure 5.10: In-phase TMF hysteresis $\varepsilon_m = 0.35\,\%$ for Nimonic 90. Creep in the tension regime dominates the hysteresis of the last cycles.

that point, the plastic strain decreases rapidly followed by a dwell at peak temperature and then decreases again to another reversal point after which it increases at a smaller rate until it reaches the maximum shortly before the temperature minimum.

One notable feature about the hysteresis loops in 5.12, also visible to an extend in figure 5.11, is that there is a progressive shift in the general level of plastic strain towards higher tensile values throughout the test. This is in contrast to the saturation behaviour in the other tests at $\varphi = -135°$ and is indicative of a significant component of creep due to the unidirectional strain. Figure 5.13 confirms that there is a remaining average tensile stress of 100 MPa – 150 MPa, acting throughout the experiment.

Failure

Figure 5.14 shows the lifetime deformation behaviour of the Nimonic 90 specimens. In general, the failure region of the test end is characterised by a rapid drop in the maximum load to the predetermined failure value, with corresponding increase in the minimum values. Apart from the IP conditions with its mean compressive stress, all curves show the symmetric behaviour, commented earlier. This diagram shows also a general reduction in

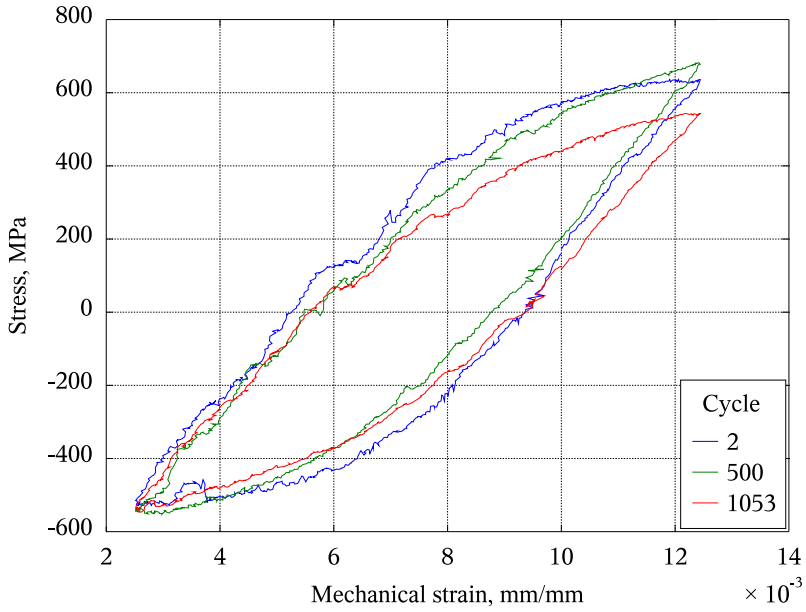

Figure 5.11: Hysteresis of Nimonic 90 with an applied strain amplitude of $\varepsilon_m = 0.5\,\%$ under offset conditions with a mechanical mean strain of $\varepsilon_{mean} = 0.75\,\%$. Creep was occuring in the compressive regime of the cycle throughout the whole experiment.

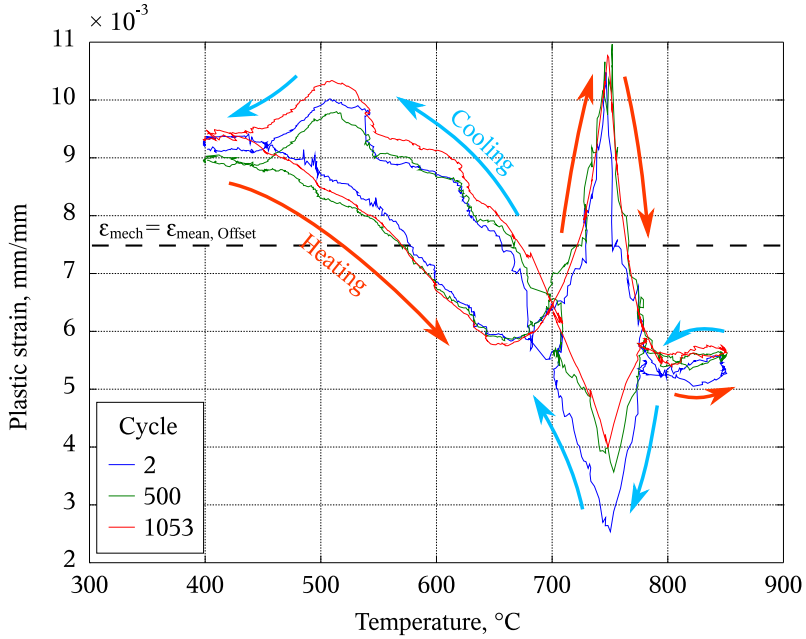

Figure 5.12: Resulting plastic strain vs. temperature for Nimonic 90 under offset conditions with a mechanical mean strain of $\varepsilon_{mean} = 0.75\,\%$. The cycle chronology is marked.

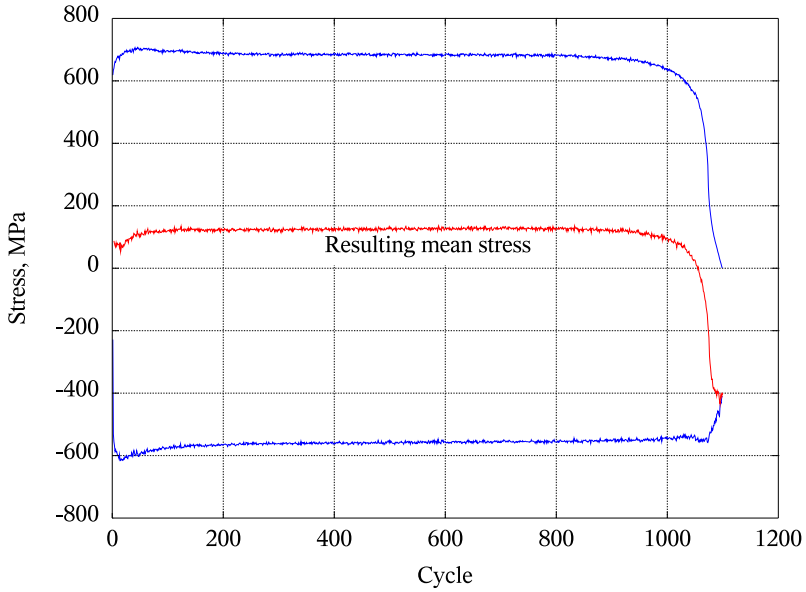

Figure 5.13: Cyclic hardening/softening behaviour for Nimonic 90 with an applied strain amplitude of $\varepsilon_m = 0.5\,\%$ and an additional mechanical mean strain of $\varepsilon_{mean} = 0.75\,\%$. This combination leads to a mean tensile stress during the experiment.

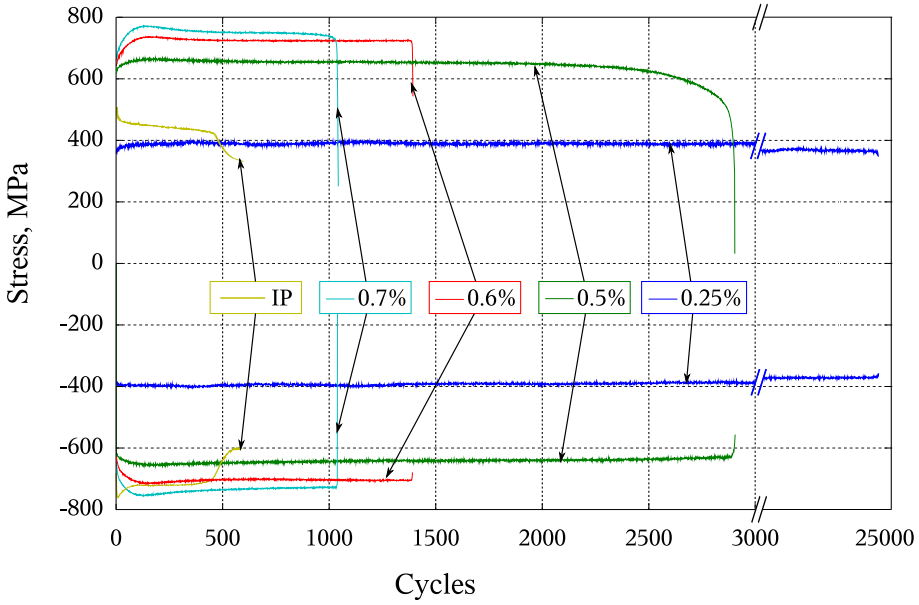

Figure 5.14: Cyclic hardening and softening curves of Nimonic 90 for varying mechanical strain amplitudes in phase shifted and in-phase TMF tests.

maximum and minimum stress magnitudes which results from a lowering of the applied mechanical strains. Varying the applied offset or the phase shift leading to mean tensile stress. Another important observation is the large decrease of lifetime brought about by small increments in strain amplitude. Table 5.1 summarises the observed lifetime data, expressed as number of cycles to failure. The investigated measured data are summarised in table 5.2, focused at the saturation and stress data.

A comparison between literature data for IP and OP conditions and the data from the current investigation is presented in figure 5.15. As can be seen, all of the best-fit straight have nearly the same slope like the $\varphi = -135°$ phase shifted line being closer to the OP than the IP line reported by Marchionni et al. [109]. Clearly, IP testing results in the lowest predicted life. The addition of a non-zero mean strain (symbol ■) reduces the lifetime in comparison to the equivalent phase shifted test by a factor of ≈ 2.8, and by more than 6 times compared to the OP results.

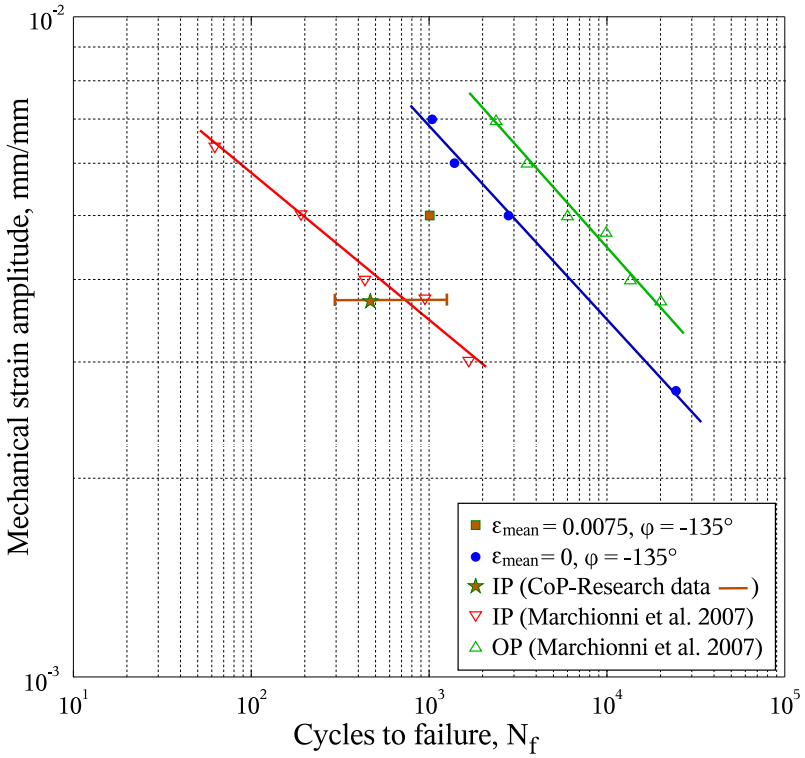

Figure 5.15: Lifetime plot for Nimonic 90, opened symbols symbolise literature data.

Because of the straight-line relationship it is possible to fit the results to the Manson-Coffin relation (equation 2.3). Accordingly the plastic strain amplitudes at the corresponding failure criterion are plotted in diagram 5.16, along with the regression line with the calculated parameters shown in equation 5.4, for which the coefficient of determination was $R^2 = 0.991$.

$$\frac{\Delta\varepsilon_{pl}}{2} = 0.726 \cdot N_f^{-0.892} \tag{5.4}$$

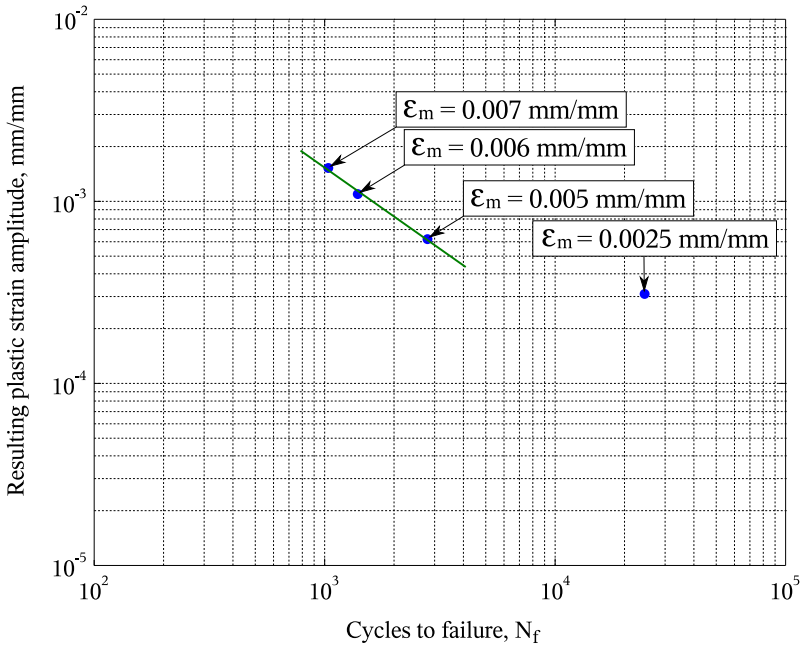

Figure 5.16: Manson Coffin plot for Nimonic 90 with plastic strain development and its scope of application $\varepsilon_m > 0.5\,\%$.

The point corresponding to the test with $\varepsilon_m = 0.25\,\%$ has not be included in the regression fit as it clearly does not follow the trend of the other three results, suggestion a different mechanism of in this test.

Table 5.1: Lifetime data for Nimonic 90 tests

Test #	Strain amplitude, %	Strain offset, %	Phase shift, °	Cycles to failure[+]
1	0.25	0	-135	24 449
2	0.5	0	-135	2 794
3	0.6	0	-135	1 392
4	0.7	0	-135	1 037
5	0.5	0.75	-135	1 002
6	0.35	0	0 (IP)	457[*]

[+] defined by a drop of the maximum cyclic stress by 10 %
[*] cycle number when the specimen started creeping

5.1.3. PM 1000

Pretest

The pretests were carried out under the same conditions as the Nimonic 90 phase shifted offset test with a small variation in temperature range. The thermal elongation also shows a non-linear correlation and the temperature dependence of Young's modulus can again be linearly approximated, figure 5.17. The determination of the thermal strains and the Young's modulus are equivalent to the Nimonic 90 pretests.

Table 5.2: Investigated data for Nimonic 90 tests

Test #	1	2	3	4	5	6
Cycles to $\sigma_{max} = 90\,\%$	24 449	2 794	1 392	1 037	1 002	457
Duration of Saturation period, cycles	24 325	2 624	1 128	773	949	338
Maximum mean stress, MPa	0	0	0	0	125	-265
Maximum tension stress, MPa	391	653	738	771	705	453
Maximum compression stress, MPa	402	658	718	758	615	725
$\bar{\sigma}_{max}$ at saturation, MPa	384	655	725	751	688	446

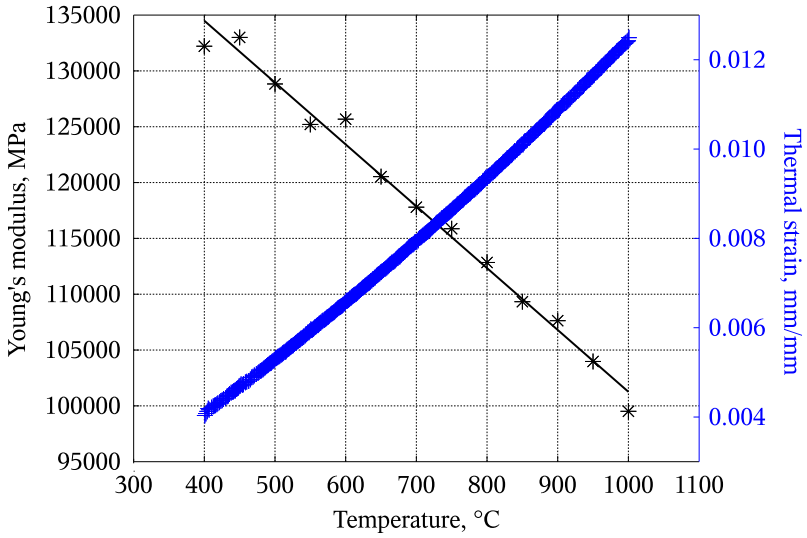

Figure 5.17: Pretest for temperature dependent Young's modulus and thermal elongation for PM 1000.

Cyclic Deformation Behaviour

As for Nimonic 90, the influence of the applied strain amplitude, test temperature and strain rate on the fatigue life and cyclic deformation behaviour have been investigated. Figures 5.18 and 5.19 show the hysteresis loops for the mechanical strain amplitudes of $\varepsilon_m = 0.1\,\%$ and $\varepsilon_m = 0.4\,\%$. These plots consist of the first complete cycle (No. 2), a half-life cycle and one after the failure criterion near final fracture for the temperature range of 450 °C to 850 °C. Due to the positive mean strain offset the hysteresis loops are shifted to higher tensile stresses. The other tests with varying parameters behave in the same way.

For both strain amplitudes a hardening effect at the low temperature part of the cycle can be observed, figure 5.18 section A-B-C. This leads to a shift of the peak stresses (sharp turning points) in the hysteris' in figures 5.18 and 5.19. In the compression regime of the cycle the peak values are nearly stable during the experiment for that sample. Typical creep conditions could be found for all tests under compressive loadings.

Fatigue Life

Figure 5.22 shows the TMF cyclic hardening and softening curves, which can be compared to the figures 5.13 and 5.14 for the Ninmonic 90 tests. In both the compression

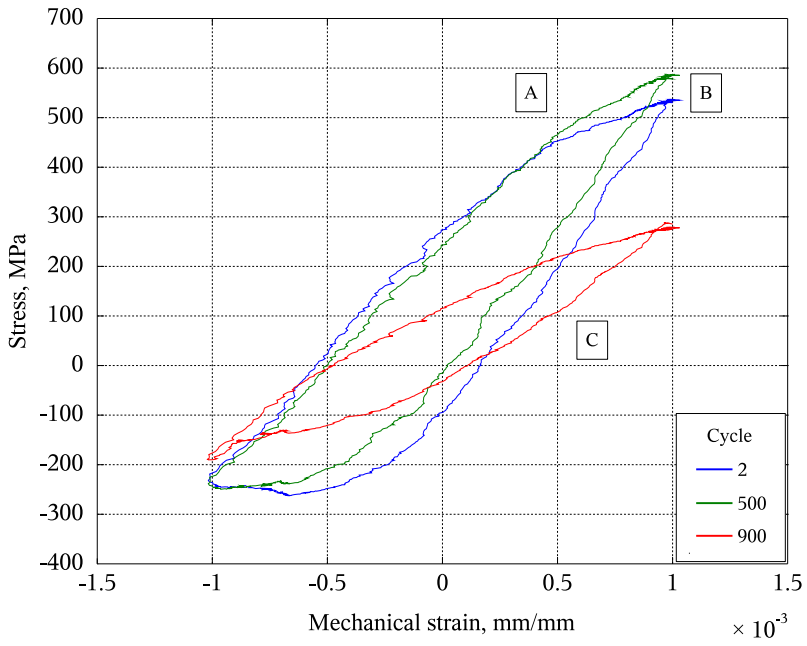

Figure 5.18: PM 1000, stress vs. mechanical strain of $\varepsilon_m = 0.1$ %, including creep effects under compression loading. The range A-B-C markes the cold region of the cycle.

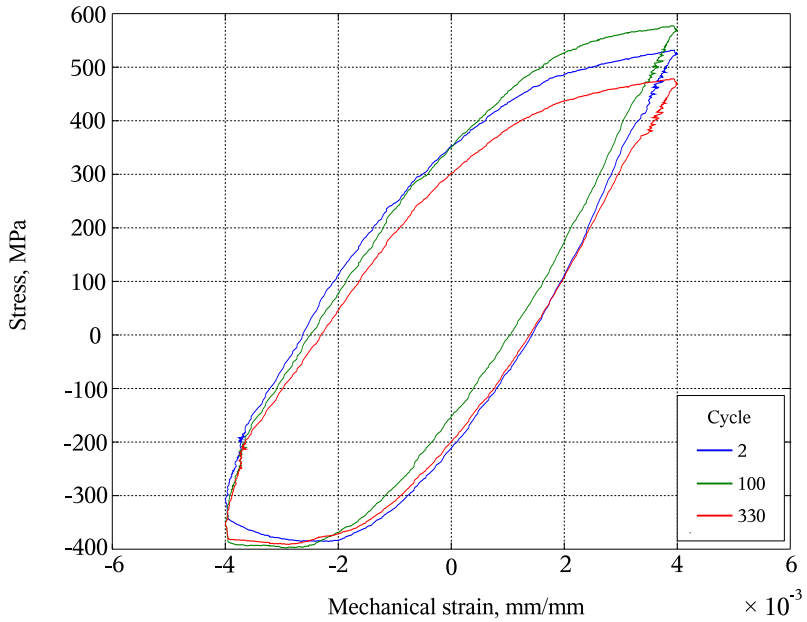

Figure 5.19: PM 1000, stress vs. mechanical strain of $\varepsilon_m = 0.4$ %, including creep effects under compression loading.

and tension parts of the cycle, the initial hardening is unlike that of the $\varphi = -135°$ tests for Nimonic 90, a saturation being set up relatively quickly. The maximum compressive stress remains either constant or gradually increases during each test, whereas the tensile stress increases to maximum and then drops off at an increasing rate towards failure. The observed mean stress as the material response is shown in figure 5.20.

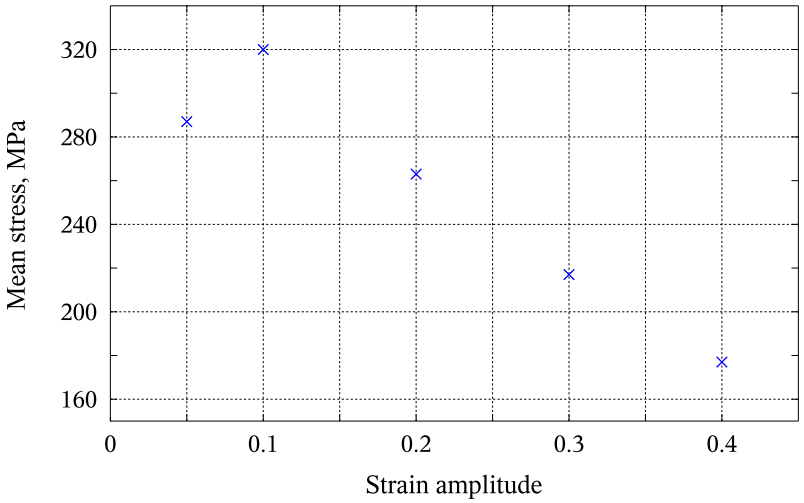

Figure 5.20: Development of mean stress at varying strain amplitudes of PM 1000.

Figure 5.21 show the hardening effect. Due to the fact that these tests were performed with a mean strain, the stress development is different to the Nimonic 90 investigations.

Figure 5.23 shows this behaviour for the $\varepsilon_m = 0.1\,\%$ test in detail with the test end criterion (10 % drop in cyclic saturation stress) marked. All tests have nearly equal maximum tensile stresses, except for the $\varepsilon_m = 0.05\,\%$ strain amplitude. The average maximum compressive stresses vary between ≈ -220 and ≈ -400 MPa increasing approximately linearly with ε_m.

During the initial TMF loops (N$<$ 10), the cyclic loading deformation curve shows fast hardening in maximum and minimum, indicated at maximum peak values by a shift to higher stresses and at the minima to lower levels. During cycling the hysteresis peaks are shifted by exposing the material to a plastic deformation and the followed unloading. The combination of the shifted phase between temperature and mechanical cycling

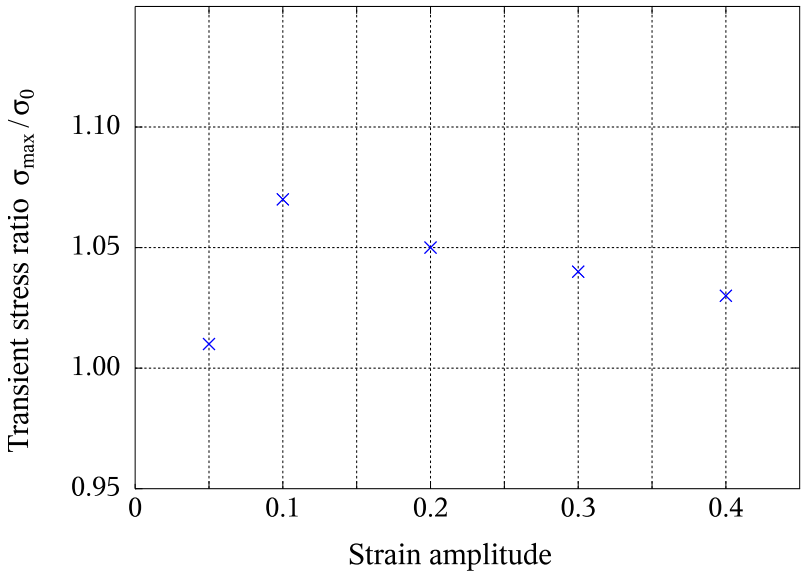

Figure 5.21: Ratio of transient and initial stresses at varying strain amplitudes for PM 1000 phase shifted tests for constant mean strain offset 0.7508 % and a phase shift of $\varphi = -135°$.

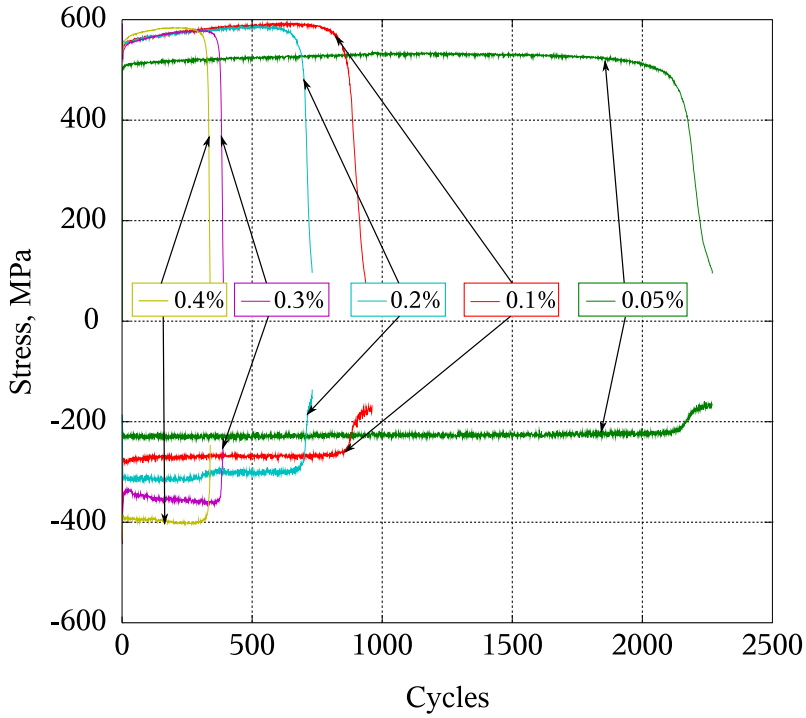

Figure 5.22: Cyclic hardening and softening curves for PM 1000 for varying mechanical strain amplitudes in TMF and strain offset of $\varepsilon = 0.75$ % .

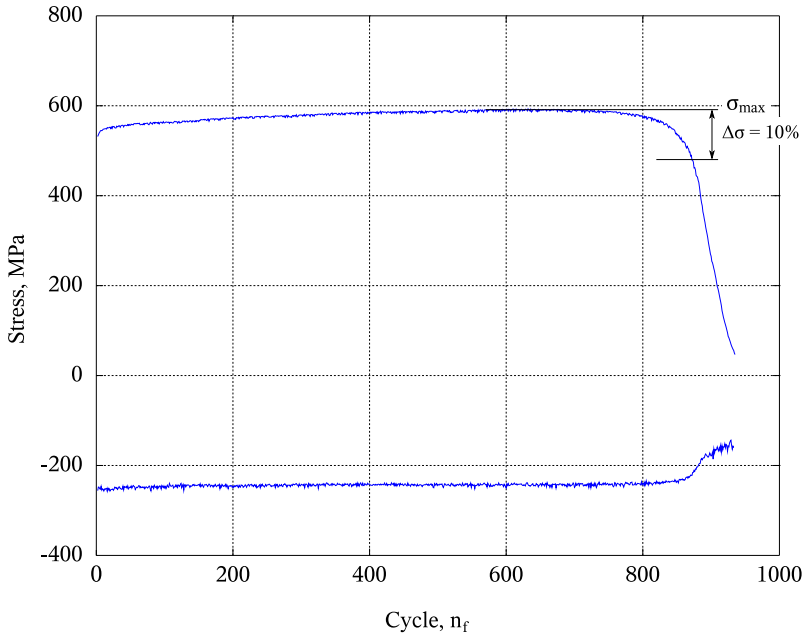

Figure 5.23: Cyclic deformation curves for $\varepsilon_m = 0.1$ % on PM 1000, showing cyclic hardening/softening, and the test end criterion.

and the additional mean strain leads to a lifetime reduction. The slope in the SN-curve is changed and reduces the calculated lifetime for smaller loadings. Compared with IP and OP cycling the reduction is in the order of 2 magnitudes, figure 5.24.

Table 5.3: Lifetime data for PM 1000 tests.

Applied strain amplitude, %	0.05	0.1	0.2	0.3	0.4
Cycles to $\sigma_{max} = 90$ %	2 063	858	691	376	327
Duration of Saturation period, cycles	2 015	836	668	358	313
Maximum mean stress, MPa	287	320	263	217	177
Maximum tension stress, MPa	516	590	583	581	584
Maximum compression stress, MPa	229	270	320	364	407
$\bar{\sigma}_{max,\ tension}$ at saturation, MPa	514	570	568	565	574

Table 5.3 shows the observed data for these PM 1000 tests.

The Manson Coffin equation for this alloy (equation 5.5) is illustrated in figure 5.25. Omitting the lowest amplitude a good linear fit can be obtained in log-log space with a coefficient of determination, $R^2 = 0.999$.

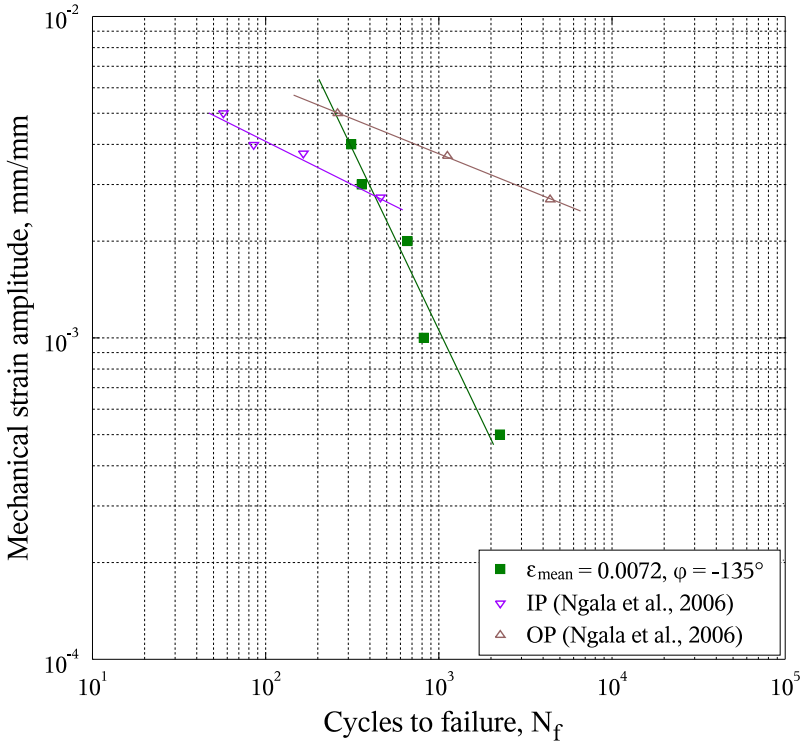

Figure 5.24: Lifetime plot for PM 1000. The offset conditions (constant mean strain of $\varepsilon = 0.7508\ \%$) and phase shift ($\varphi = -135°$) lead to a steeper slope and a dramatic reduction of the lifetime even in lower amplitudes compared to In-Phase and Out-of-Phase tests performed by Ngala et al. [18]. The current investigations were performed on specimens with an equivalent microstructure.

$$\frac{\Delta\varepsilon_{pl}}{2} = 16.155 \cdot N_f^{-1.928} \tag{5.5}$$

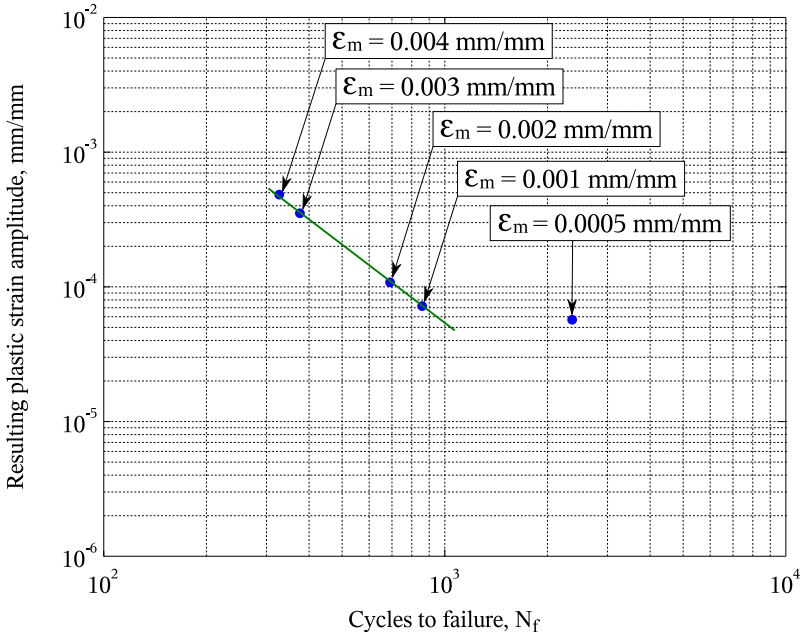

Figure 5.25: Manson Coffin plot for PM 1000 with plastic strain development and its scope of application with the lower limit of $\varepsilon_m > 0.1$ %.

5.2. Microstructural Investigations

Scanning electron and optical microscopy was performed in order to characterise the damage evolution in detail. The influence of test temperature and applied strain amplitudes on crack initiation, propagation and fatigue life was investigated. All fractured specimens were examined to evaluate the fatigue damage with mode of cracking and any other crack propagation or influencing effects. Other characteristics, e.g. dispersiods or precipitations are not visualisable by the used equipment and cannot be determined by this way.

5.2.1. Nimonic 90

Perceptible microstructural differences and changes regarding the grain sizes or twin densities could not be determined for Nimonic 90 material.

Phase shift of $\varphi = -135°$

For all tests with a phase shift between mechanical strain and temperature, cracks were initiated on the specimen surface and propagated into the volume in a transgranular manner. Multiple crack initiations were observed in all specimens, figure 5.26.

The fracture surfaces at these amplitudes are characterised by twins in the volume, figure 5.27 and the crack propagation area, figure 5.28 with the small terrace fracture surface.

An example of the crack evolution is presented in the composite image figure 5.29 with its complex cracking mode, starting transgranular and changes later into intergranular cracking.

In-phase conditions

In contrast to the phase shifted investigations, the dominant crack evolution mode are under in-phase conditions intergranular as can be seen in the fractograph' figure 5.30,

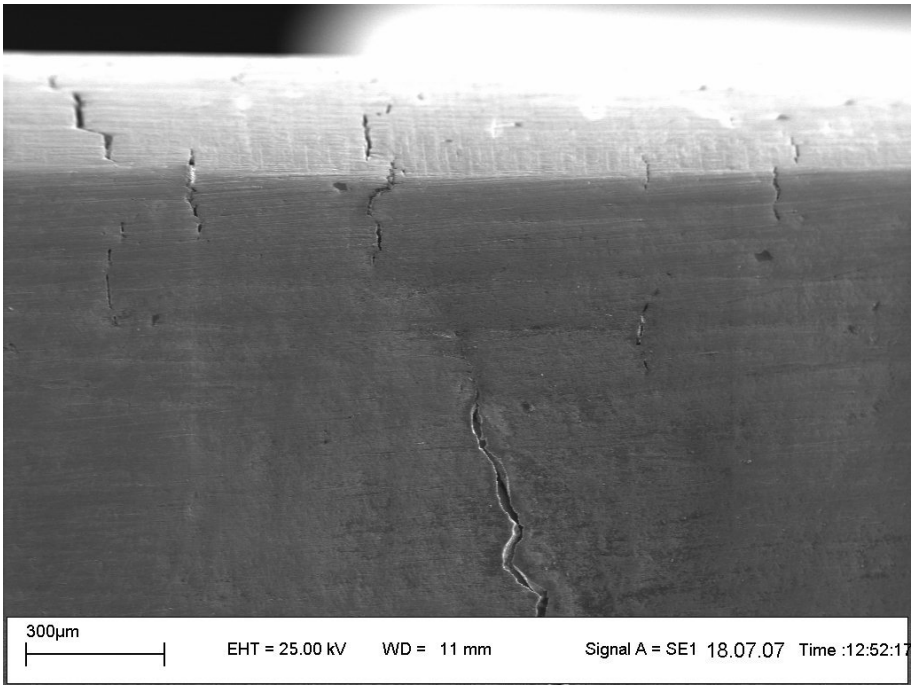

Figure 5.26: Multiple surface cracks for $\varepsilon_m = 0.7\,\%$ with a horizontal loading direction for Nimonic 90, [96].

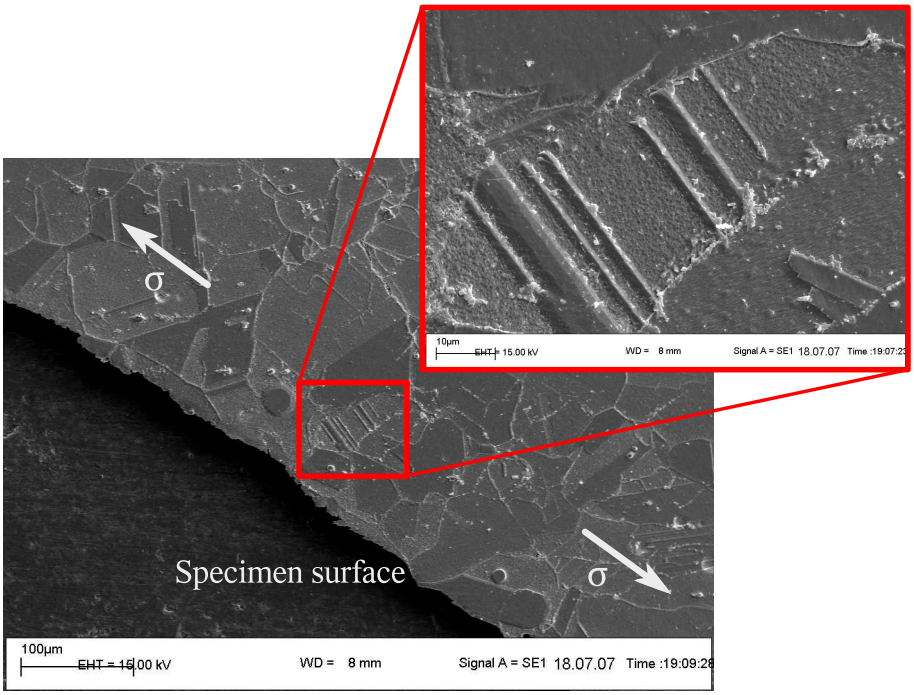

Figure 5.27: Twins after a loading of $\varepsilon_m = 0.7\,\%$. Electrolytically etched with chromic acid.

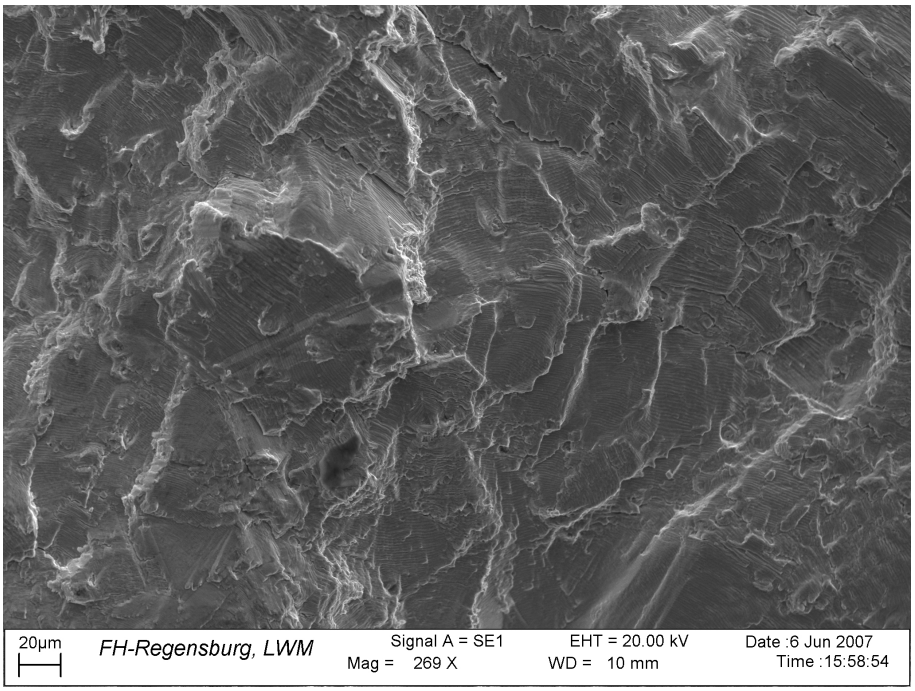

Figure 5.28: Fractography of $\varphi = -135°$ and $\varepsilon_m = 0.5\,\%$ with a transgranular crack growth, striations and lamellar fracture.

which shows the oxidised grain structure on the fractured surface. A secondary internal crack can be observed in the middle of this picture again running intergranularly. The importance of oxidation in the opening of cracks at the highest temperatures of the cycle can be seen in figure 5.31. Secondary cracks, related to the high plastic deformations along the gauge length can be seen in figure 5.32. This high plastic deformation leads to a increased twin density.

Phase shift with strain offset $\varphi = -135°$, $\varepsilon_{mean} = 0.75\,\%$

Parallel gliding plane areas can be found at the fracture surface of the specimen with strain offset, figure 5.33, which are typical markers of incremental crack propagation. Secondary transgranular microcracks were also observed perpendicular to the loading direction, comp. figure 5.34. The crack is characterised by a mix of intergranular and transgranular cracking.

Figure 5.35 shows the cross section after the long-term test. It does not lead to

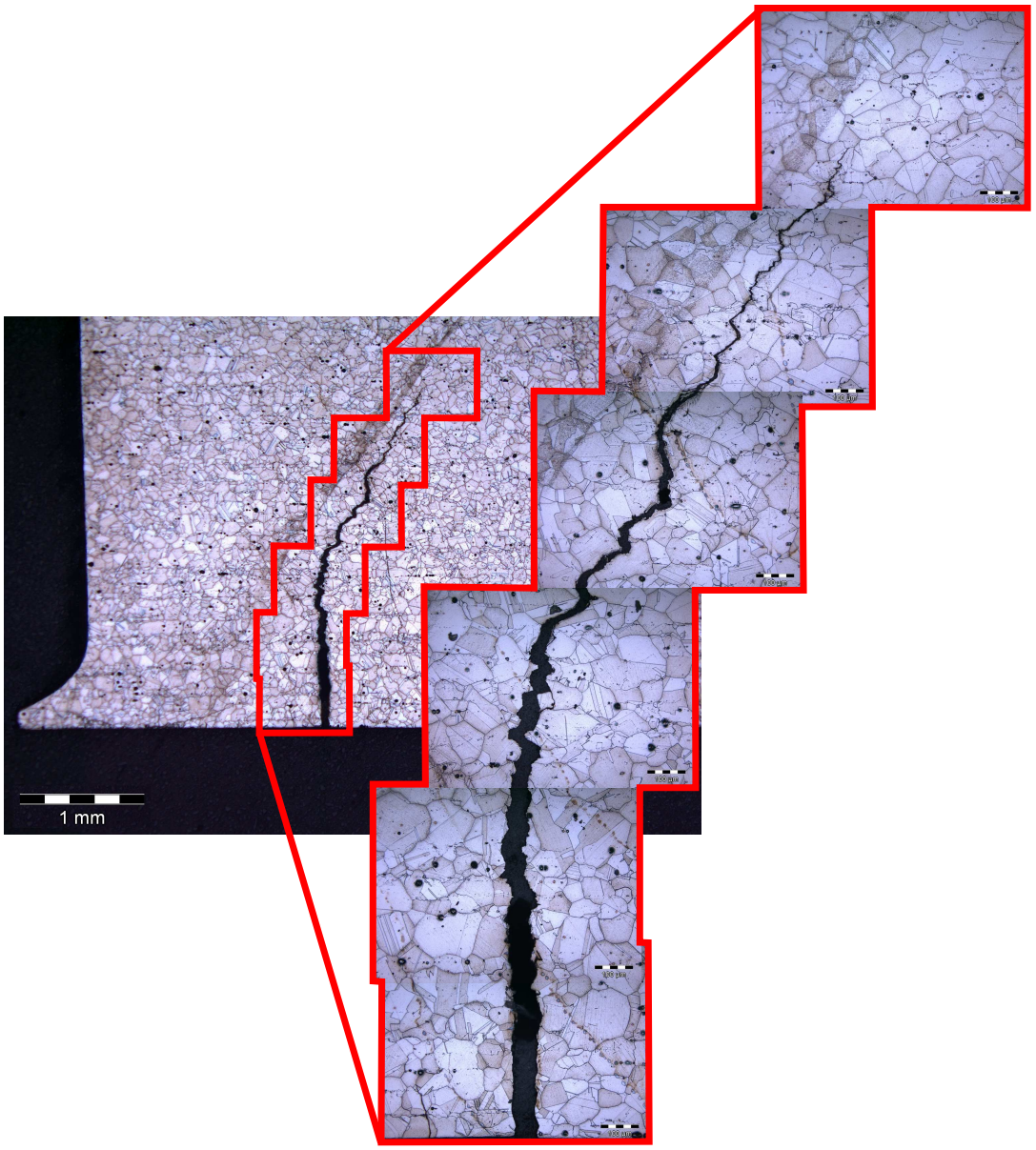

Figure 5.29: Crack evolution for mechanical strain amplitude of $\varepsilon_m = 0.6\,\%$ under phase shifted conditions. A typical transgranular cracking at the surface can be observed. The crack propagates in mixed mode (inter- and transgranular). The loading direction is horizontal.

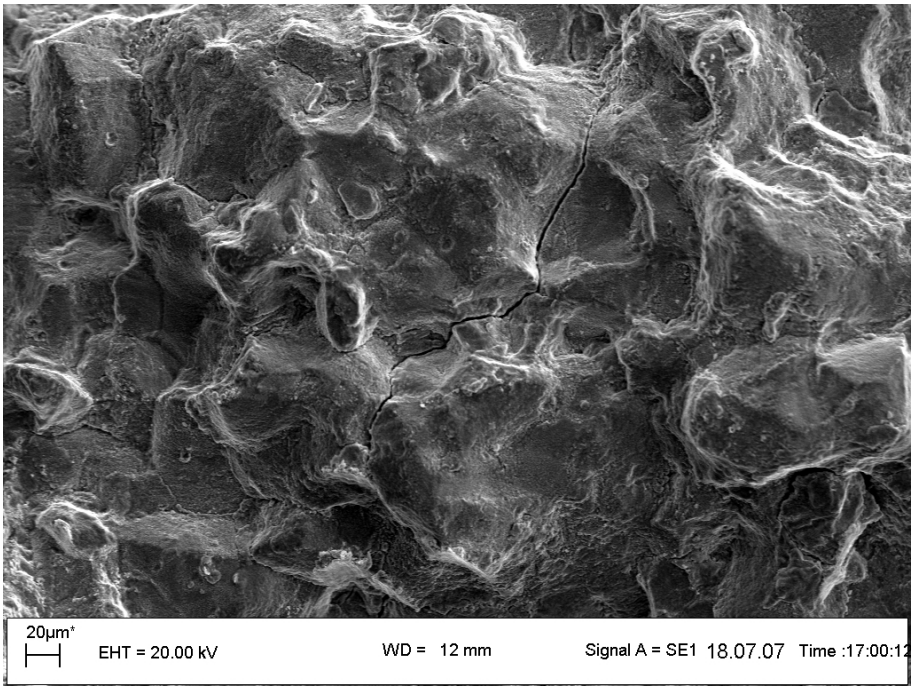

Figure 5.30: Fractograph of IP TMF specimen with an intergranular crack growth and a secondary volume crack.

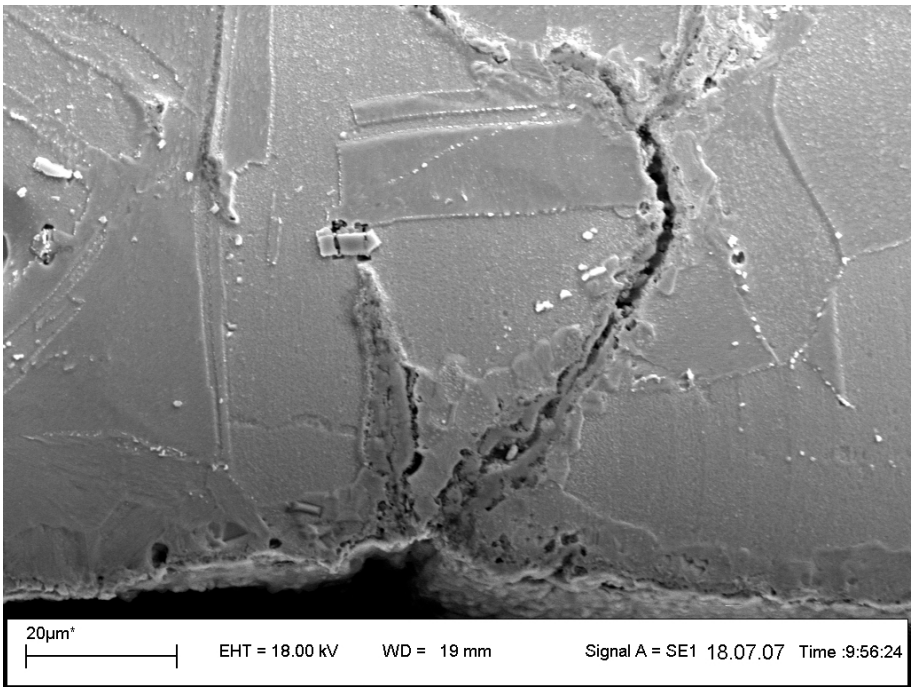

Figure 5.31: IP TMF with intergranular crack growth. Oxidation growth at the head of the crack can be observed. The loading direction is horizontal. Polished and electrolytically etched in chromic acid.

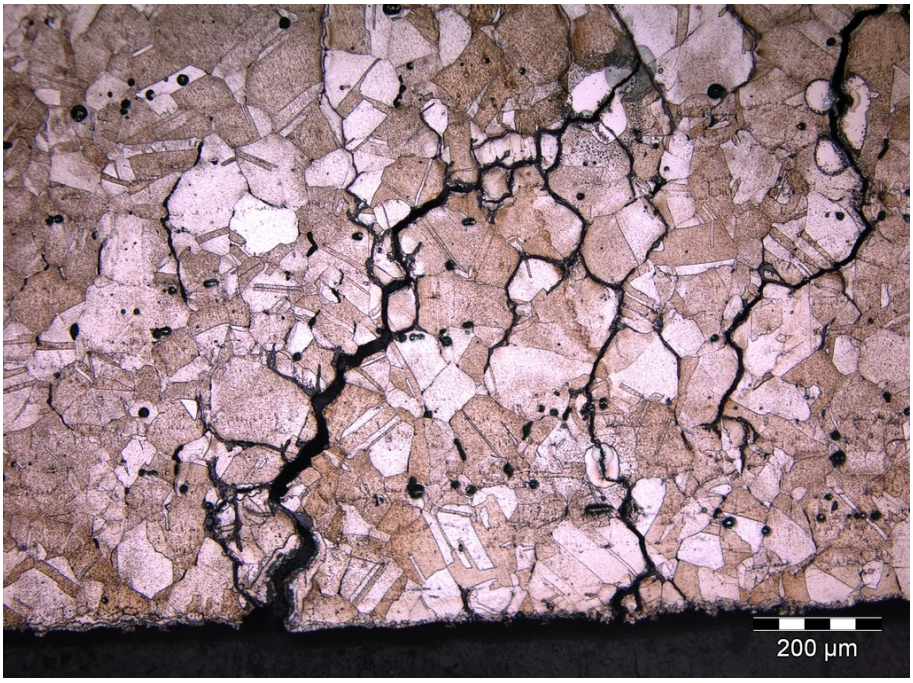

Figure 5.32: Secondary intergranular cracks in Nimonic 90 under IP conditions also showing a high twin density [96].

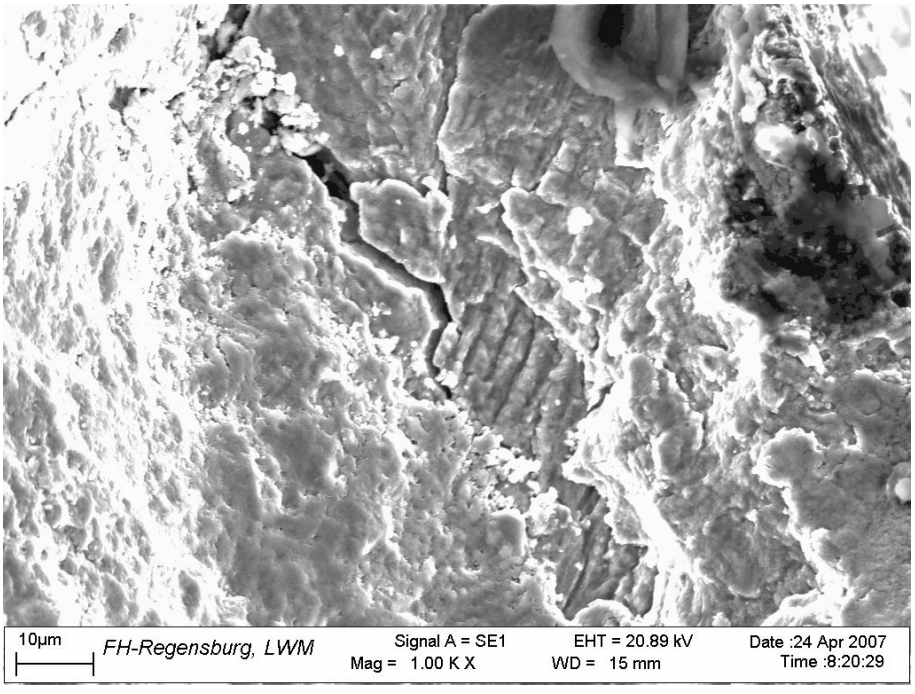

Figure 5.33: Crack propagation area with fatigue striations and an intergranular crack. The fracture surface is partially covered by an oxidation layer, Nimonic 90, $\varepsilon_m = 0.5\,\%$, $\varepsilon_{mean} = 0.75\,\%$, $\varphi = -135°$ [96].

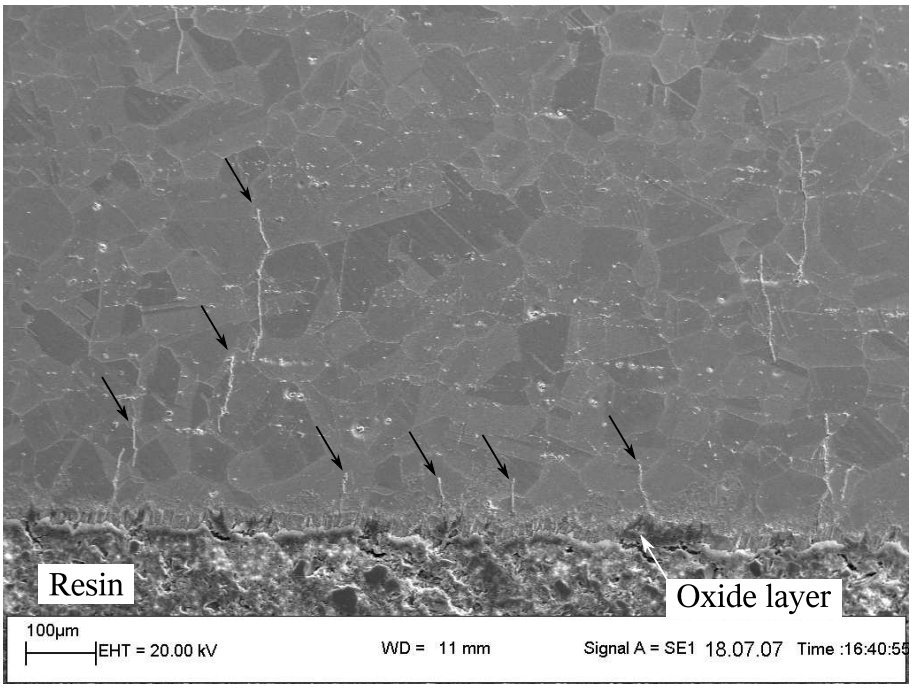

Figure 5.34: Cross section of the gauge length of the Nimonic 90 specimen, $\varepsilon_m = 0.5\,\%$, $\varepsilon_{mean} = 0.75\,\%$, $\varphi = -135°$. The horizontal loading direction leads to the marked secondary transgranular and perpendicular microcracks. The oxidation growth can be seen at the complete outer specimen surface.

additional internal cracking or large-scale microstructural changes. In contrast to this, figure 5.36 shows the high strain amplitude test, where internal transgranular cracks can be observed.

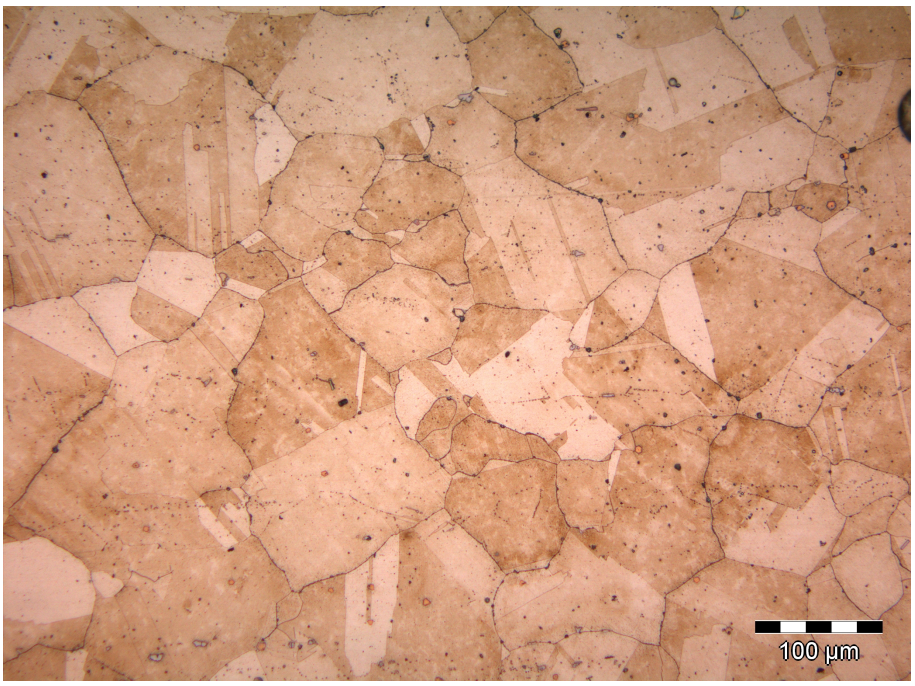

Figure 5.35: Nimonic 90 microstructure for $\varepsilon_m = 0.25\,\%$ with horizontal loading direction; etched with Bloech & Wedl II [96].

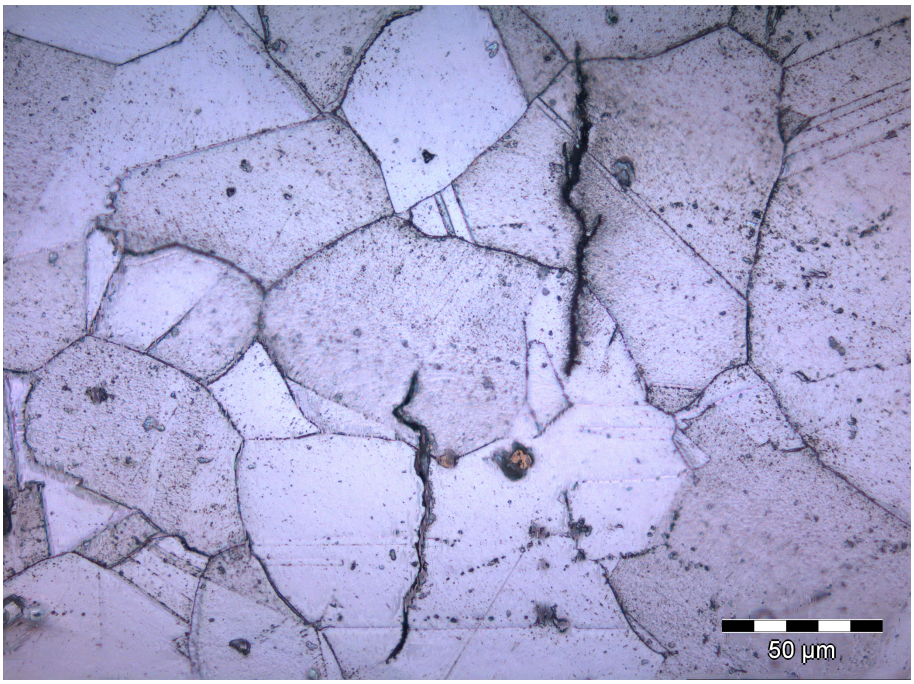

Figure 5.36: Internal volume cracking for $\varepsilon_m = 0.7\,\%$ with horizontal loading direction. These type of cracking was observed over the complete section surface.

5.2.2. PM 1000

The offset TMF specimens are characterised by a ductile failure without necking, figure 5.38 and 5.37. Fractography of the tested specimens showed typically intergranular cracking pattern as well as an oxidised surface, 5.39 for all load regimes. Regions of high plastic deformation, could be found on all fractured specimens. Subsequent sectioning of the gauge length and SEM examination confirmed the intergranular cracking behaviour, figure 5.40. The beginnings of void formation due to the creep activity under compression at lower temperatures could be observed for $\varepsilon_m = 0.1\,\%$.

Fatigue striations as an indicator for high plastic deformations were observed for mechanical strain amplitudes of $\varepsilon_m = 0.1\,\%$ at the fractured surface. This region is marked in figure 5.41.

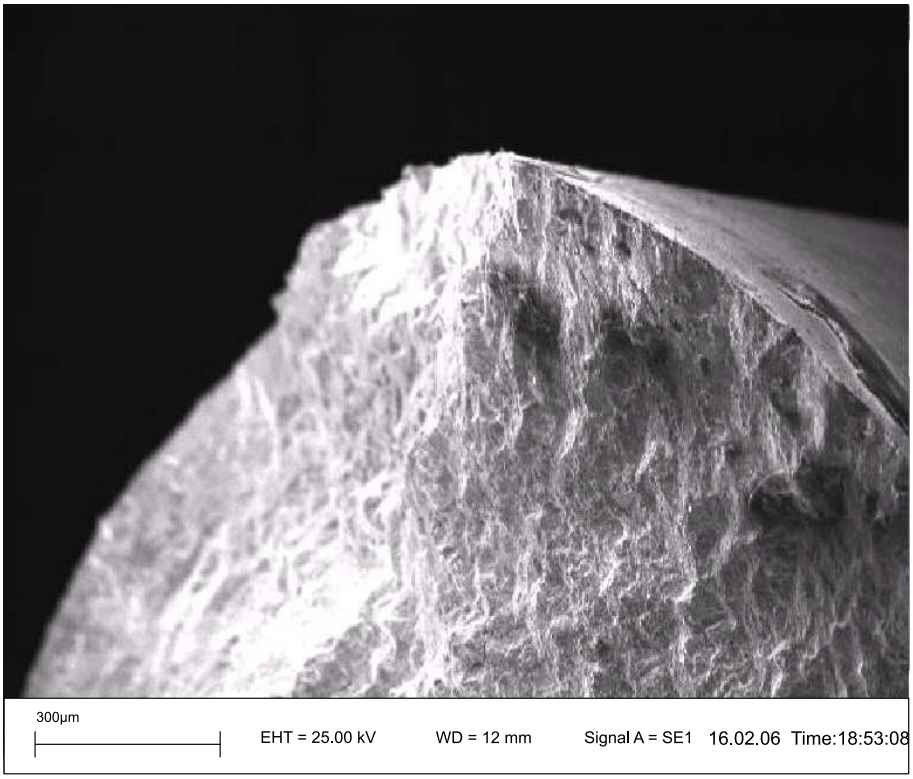

Figure 5.37: Fractography of PM 1000 for an applied mechanical strain amplitude of $\varepsilon_m = 0.1\,\%$. The fracture surface is not necked.

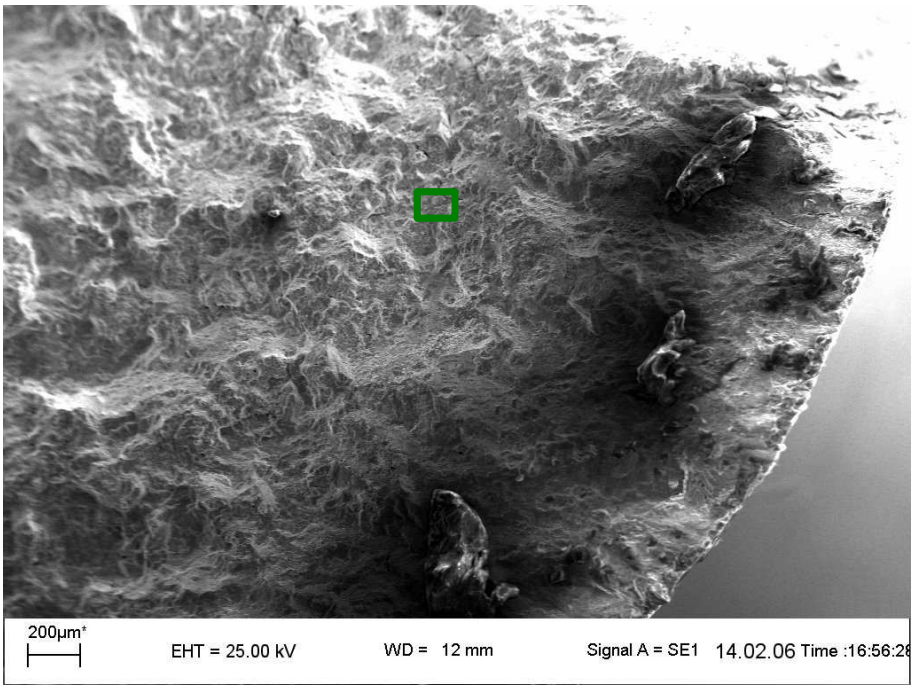

Figure 5.38: Fractography of PM 1000, $\varepsilon_m = 0.1\,\%$. The marked area represents the detailed view of figure 5.39.

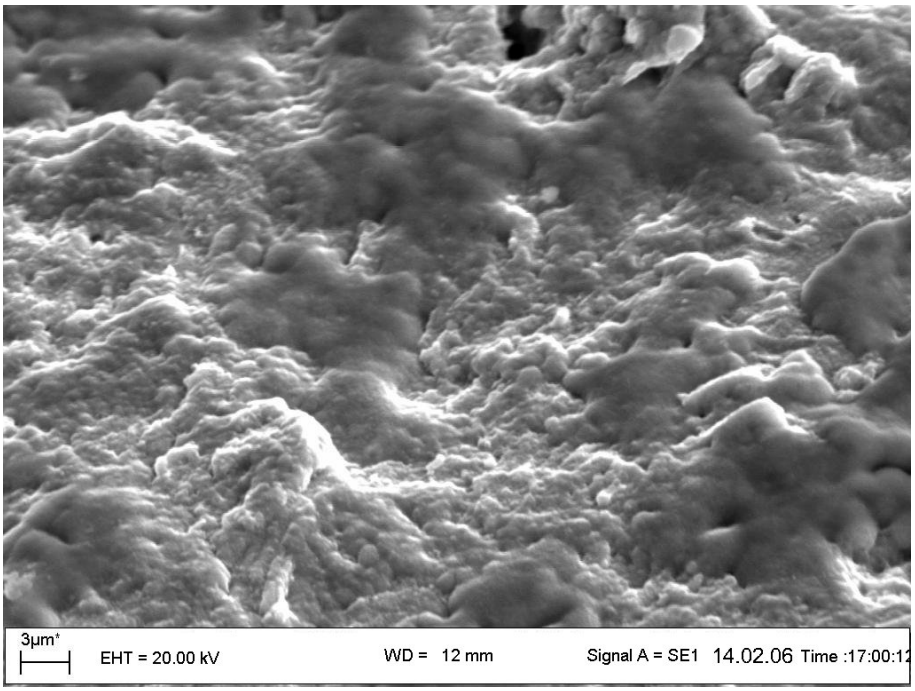

Figure 5.39: Detailed view of the fractured surface of PM 1000 for an applied mechanical strain amplitude of $\varepsilon_m = 0.1$ % shows the typical oxidation layer of the fracture surface.

5.3. NiAl

5.3.1. Creep Behaviour

The creep behaviour of NiAl exhibits several "classic" characteristics and the minimum rate suggested by the Monkman-Grant equation. The first specimen was loaded under a constant force of 34.8 N. The measured lifetime for this test is the basis of the following lifetime calculations, based on the Monkman-Grant relation for the stepwise loaded specimen. The analysis starts with the total strain development during the experiment, figure 5.42. The observed creep starts with a rapid strain increase, followed by a reduced creep rate.

A polynomial fit gives a continuous function which can then be differentiated to find the creep rate as a funtion of time. This function is plotted for the initial portion corresponding to the actual range of experimental observation. As can be seen, there is a clear minimum, which can be used to fit a creep rupture time at that stress and temperature,

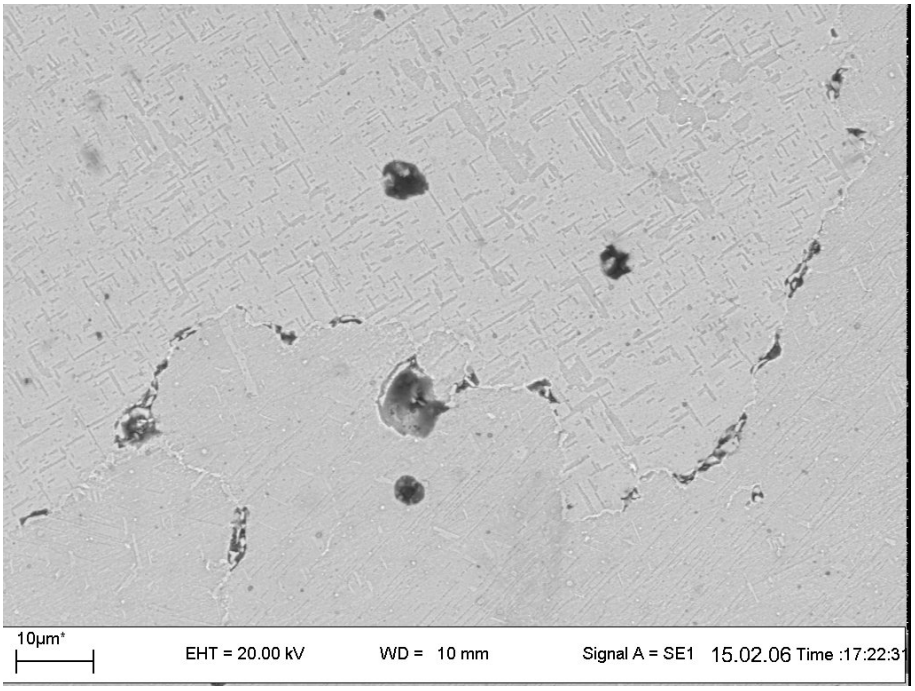

Figure 5.40: SEM of microstructure corresponding to figure 5.39 in horizontal loading direction and transversal sectioning with clearly identifiable cracks along the grain boundaries as well as the beginning of grain boundary sliding in the middle of this picture. Cutting direction is The surface texture is due to the special SEM etching solution.

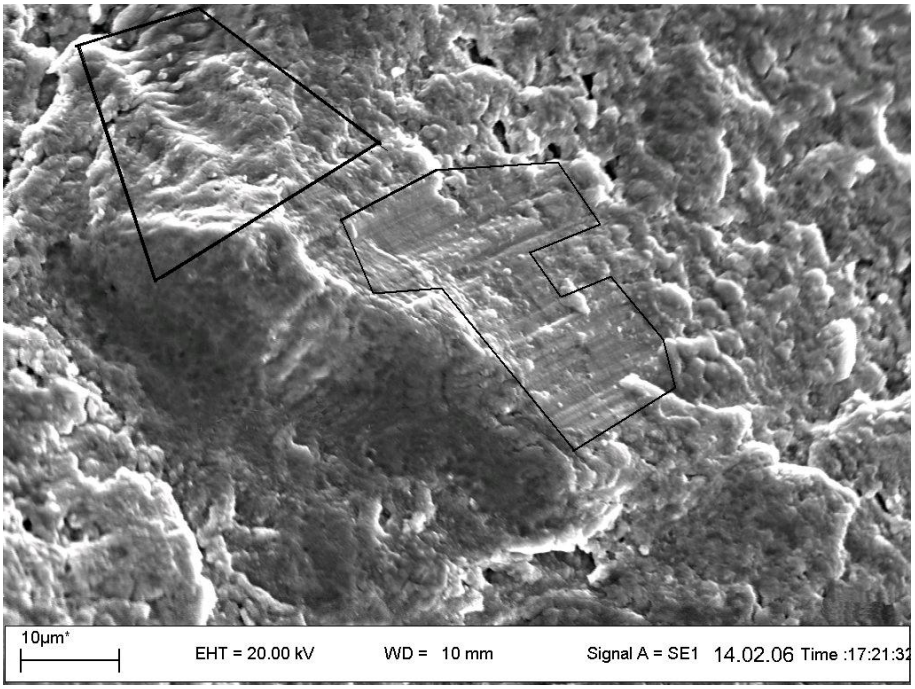

Figure 5.41: Fatigue striation and deformation twins marked on the fracture surface of PM 1000 for an applied mechanical strain amplitude of $\varepsilon_m = 0.1\,\%$.

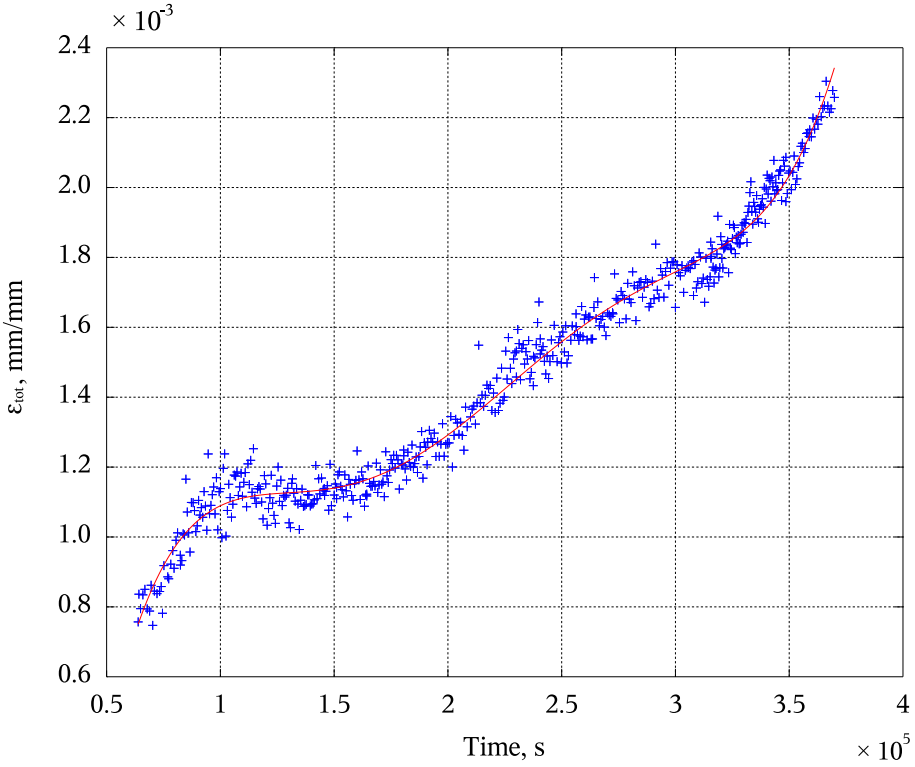

Figure 5.42: Total strain development vs. time curve for the 40 MPa test. The red line indicates the polynomial fit for the subsequent differentiation [112].

figure 5.43. After this minimum the loads steps can be realised. The investigated time for measured creep rates for the load step test is marked by a solid line style.

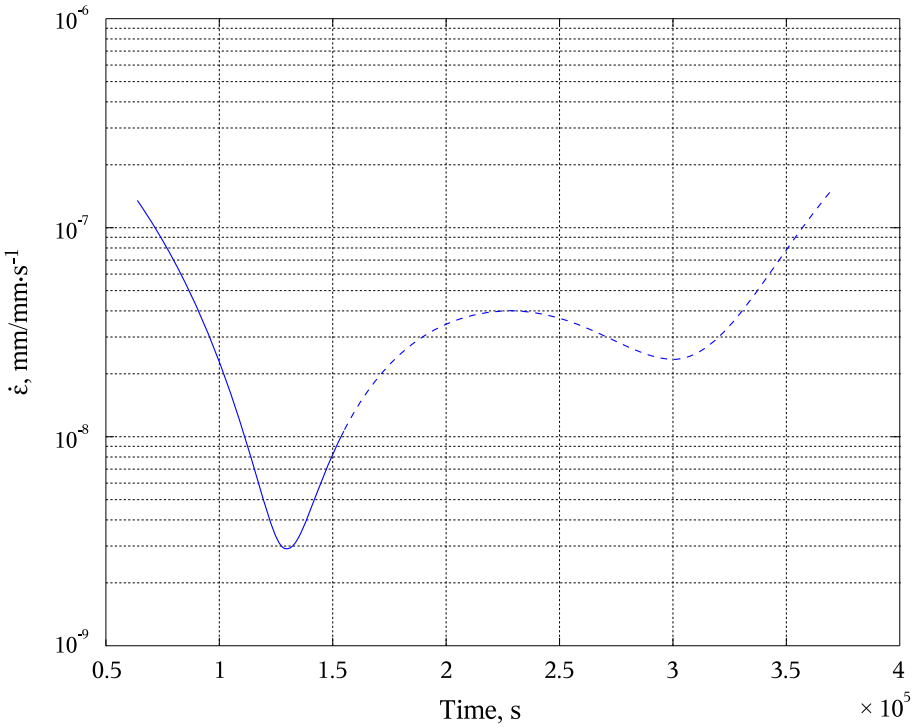

Figure 5.43: Derivation of the fitted polynomial of figure 5.42. The solid line style marks the part of the curve which relates to the experimental data.

Figure 5.42 shows the development of the total strain with time for the 40 MPa test. The initial part until the first minimum is characterised by a higher creep rate than in the presented time range. The scatter in the measured data is related to the resolution of the markers. To ensure stable numerical conditions for the subsequent differentiation of the data, they were fitted using a polynomial of a 5th order. The result of this differentiation is the time dependent strain rate evolution, figure 5.43. In general, the important point of this curve is the first minimum, and the range of the curve useful in the calculation of the creep exponent n is marked by a solid line style. The differentiated creep curve plotted vs. the total strain shows the first creep stage until the minimum, figure 5.44. The 40 MPa and 80 MPa stress levels have local strain minima with a saturation zone in contrast to the 103 MPa test, which shows a constant increase of the analysed creep rate.

The results at all the stresses are summarised in table 5.4. In general, smaller me-

chanical loading leads to lower minimum creep rates, figures 5.44 and 5.45, and the creep exponent n was calculated to be $n = 4$. Figure 5.45 shows a small step in the creep exponents.

Table 5.4: Results for creep analysis for NiAl Results, including lifetimes, calculated from equation 2.7.

Initial applied stress, MPa	True stress at minimum creep rate, MPa	Minimum creep rate, $\dot{\varepsilon}_s$, s^{-1}	Estimated lifetime, h
39.8	43.1	$2.865 \cdot 10^{-9}$	102.8^{+}
80.1	84.3	$2.769 \cdot 10^{-8}$	10.6
102.7	107.2	$9.341 \cdot 10^{-8}$	3.2

$^{+}$ This time was measured and is the basis for the other estimated lives.

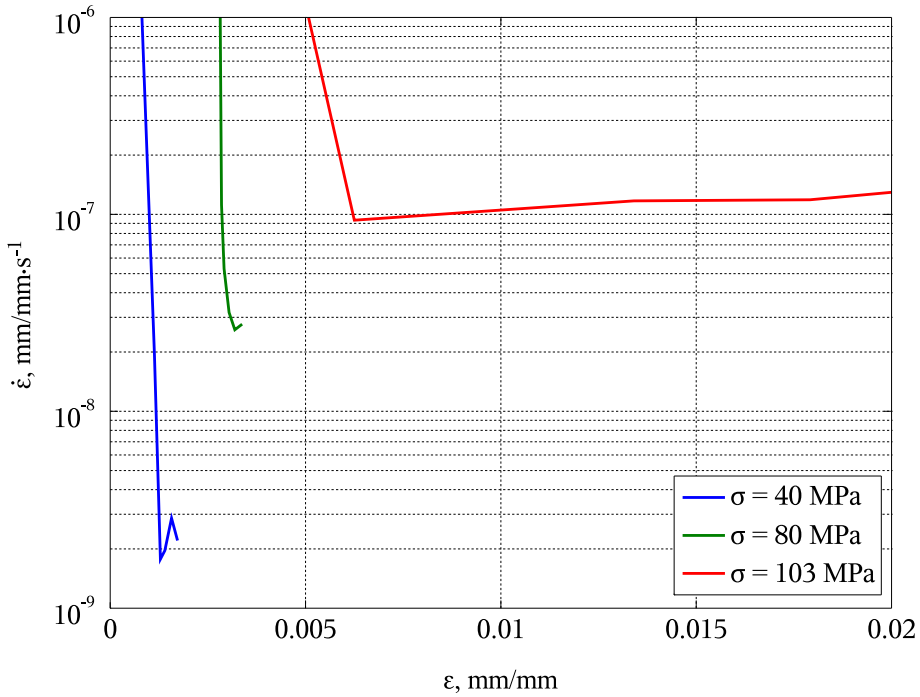

Figure 5.44: Creep rate vs total strain. 40 MPa and 80 MPa stress levels have distinctive local strain minima including saturation zones in contrast to the 103 MPa stress curve. Rather this test shows a constant increase of the total strain and the creep rate after the minimum.

The curves of 40 MPa and 80 MPa tests are slightly steeper after the minimum than the 103 MPa data. Due to the fact, that there was an incremental increase of the load a real stationary creep zone after the minimum could not be observed. Figure 5.45 shows

no distinctive transition threshold for the applied loads and the resulting minimum strain rates.

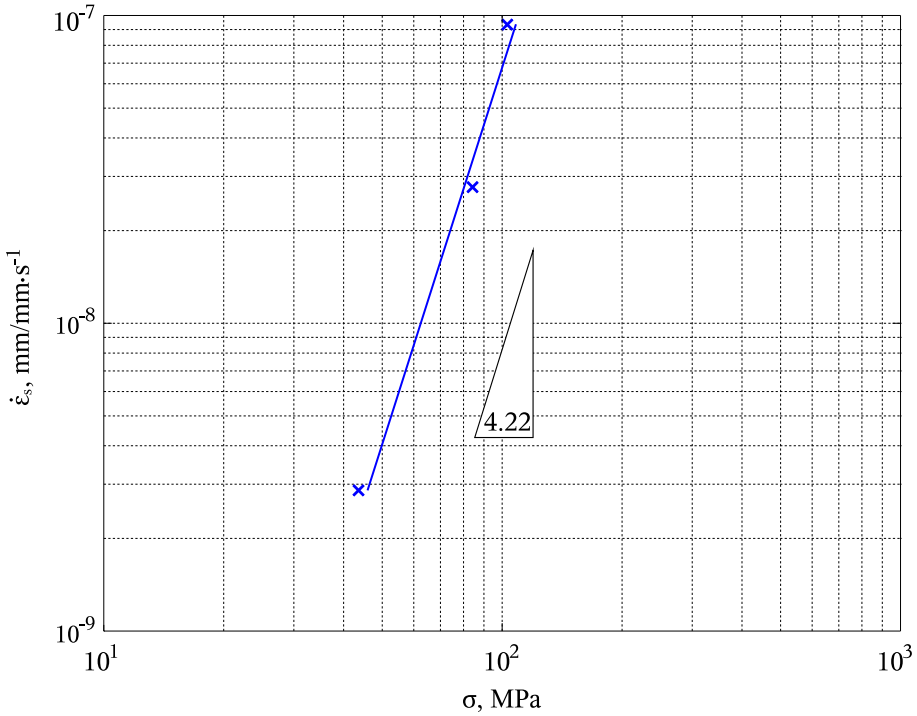

Figure 5.45: Norton plot (minimum creep rates vs. depending stresses) and the resulting creep exponents.

Table 5.4 summarises the loads, creep rates and the lifetimes calculated by the Monkman-Grant relation 2.7.

An obvious neck formation during the creep exposure was observed for all specimens, figure 5.46, which leads to a reduction in the cross section and therefore to an increasing stress. The thickness remain constant also be seen in the fractography images figures 5.48 and 5.49.

Hence, based on the Norton creep law, explained in subsection 2.1.3, the determination of the creep parameters can be carried out, using equation 2.5. The constant A can be calculated to be $3.628 \cdot 10^{-16}$, assuming $Q = 307\ \mathrm{kJ/mole}$ for the thermal activation energy [113].

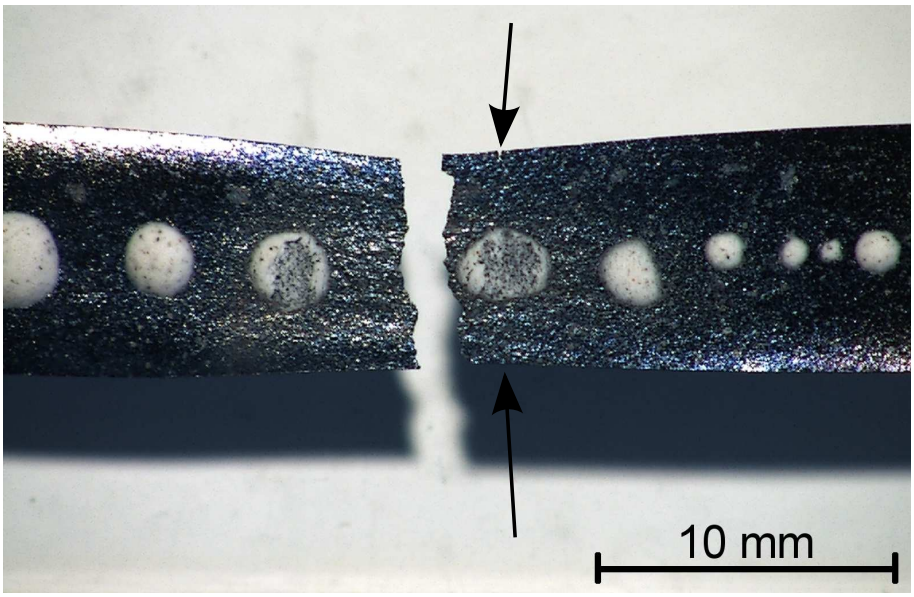

Figure 5.46: Fractured creep specimen with markers on the surface. The strains were calculated after the test by binarisation, calculating the moment of inertia of each marker and their resulting local strains. The right hand half of this specimen shows additional microcracks.

5.3.2. Microstructure

The specimens were embedded in resin for SEM X-ray mapping, figure 5.47. No specific element distribution, e.g. oxidation layers, could be observed, all elements being uniformly distributed. Furthermore the fracture surface shows typical indications of intergranular creep effects, based on dislocation mechanisms, namely v-notches, figure 5.49 and cavities, figure 5.48. Cavities are an indicator for intergranular creep behaviour. All the micropores at the grain boundaries are combined to larger chains of these pores until v-notch cracks, indicating grain boundary gliding and are marks of an advanced creep stage [54]. Secondary microcracks could be found in the near of the fractured region along the gauge length, parallel to the loading axis.

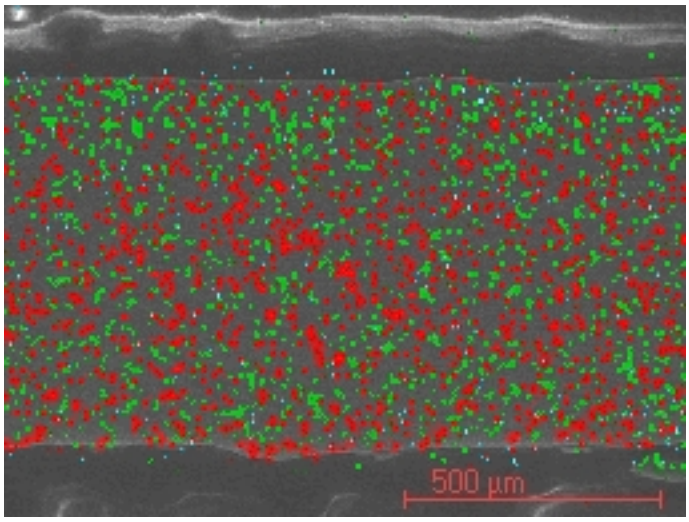

Figure 5.47: EDS-Mapping of polished cross section. This area has no inhomogeneous element distribution. Green points indicate aluminium, red, nickel and blue, oxygen.

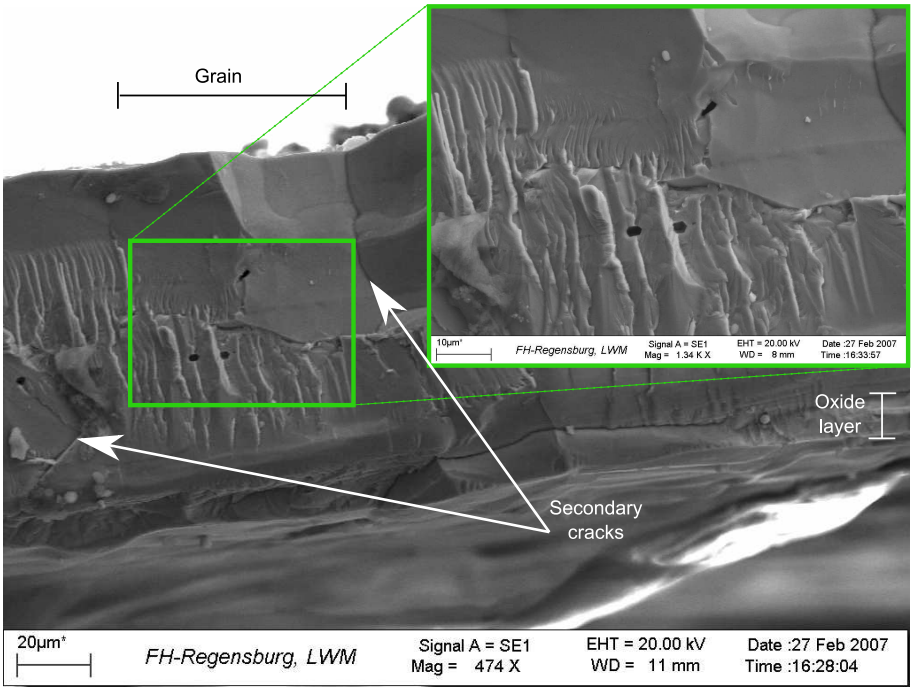

Figure 5.48: Crack surface, load: 40 MPa. Cavities as a typical indicator for intergranular creep mechanisms could not be detected. Moreover they are located inside the grains.

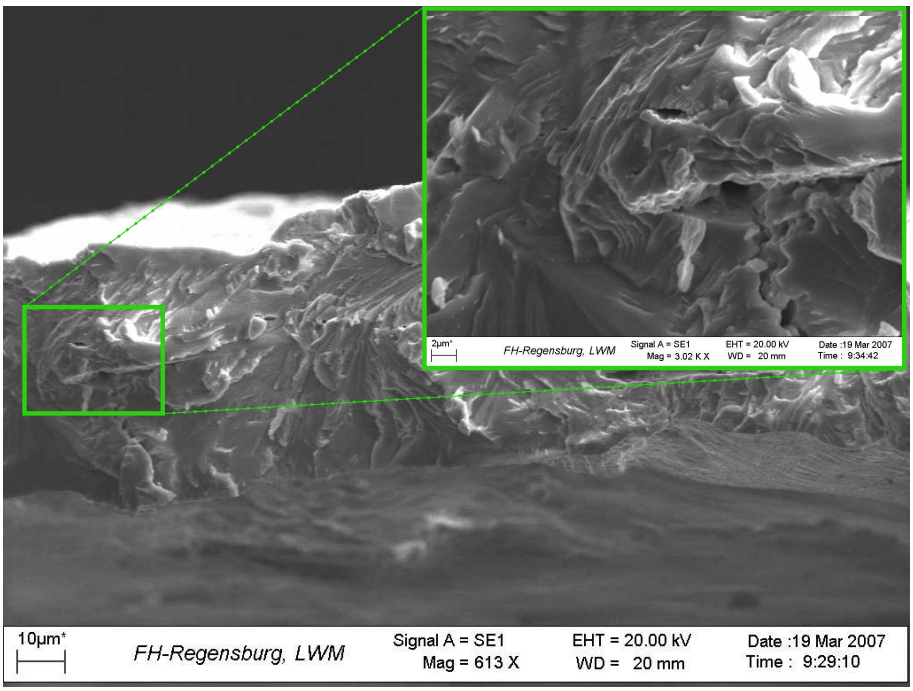

Figure 5.49: SEM picture of the crack surface from the 80 MPa test. The v-notch cracks are typical for grain boundary gliding and dominate the crack surface [54].

6. Discussion

This study focuses on the deformation behaviour of two different nickel base superalloys, one oxide dispersoid strengthened (PM 1000) and one matrix material (Nimonic 90). A third investigation focussed on the creep behaviour of the commonly-used diffusion coating. Considerable effort was put into precise measurement and control techniques in view of the high specimen costs and some measurements were made on well-studied material in order to benchmark. The phase shifted fatigue life in TMF, as an important factor for the blade and case design, and the creep behaviour of the pure coating as well, have been not addressed yet. The investigated results from all tests, described within the Results chapter, will be summarised and discussed. Therefore this chapter is separated into the main issues of this thesis:

- Experimental set-up
- Fatigue lives
- Microstructures
- Creep

6.1. Experimental Set-up

The precision of the overall set-up was demonstrated by the very small stress range of the zero stress test, shown in subsection 4.2.1. This precision was attributable to the exact

pretest procedure and accurate control algorithms. The long time stability for a complete test is shown in section 5.1.1. The use of a temperature-compensated mechanical strain control signal in combination with very small interpolation ranges for the thermal strain values is the basis of the precise long term tests and ensures accurate results for changing environmental conditions. Hähner et al. [2] limited the maximum allowed zero-stress-test amplitudes to 5 % of the maximum resulted stress. Under the applied loads for Nimonic 90 with the smallest mechanical strain amplitude ($\varepsilon_m = 0.25\,\%$) the acceptable stress range according this criterion is ± 20 MPa. Figure 4.12 shows the peak stresses of this benchmark test, ≈ 1 MPa in compression and ≈ 4 MPa in tension. In front of these limitations, agreed by several institutes, the benchmark of this equipment can be regarded as successful.

6.2. Fatigue Lives

The saturated stress amplitudes for the "pure matrix material", Nimonic 90, increase with increasing strain amplitude and are associated with decreased cyclic life.

Even with similar stress amplitudes, fatigue lives are strongly dependent on the specific loading conditions. Figure 5.1 shows that IP TMF and strain offset TMF are the most damaging conditions. The superposition of the damage mechanisms during these tests leads to that massive life time reduction. This superposition can be different by the use oxidation resistant materials. Also some coating structures may influence the damage behaviour. These test modes accelerate crack initiation and propagation as well as final failure. Reduced fatigue lives can be explained by early crack nucleation. On the other hand, the large plastic strains induced by higher temperatures accelerate crack propagation. In each test with reduced strain amplitudes most of the life is spent for crack initiation. This was observed for both superalloys, figure 5.13 and 5.22. The temperature is also as important, a small constant temperature increase of 20 K during the test leading to a slightly reduced lifetime, attributed to environmental and time dependent damage mechanisms, e.g. oxidation and creep. These mechanisms are most active during the high

temperature part of the cycle, and coincide with the crack opening for the IP TMF and the offset TMF tests. The material spends more time in the tensile regime than in compression which accelerates the diffusion of easily-oxidised elements, such as Cr, Ti and Al, and microvoid coalescence along the grain boundaries. For IP tests the high temperature half of the cycle exposes the crack surface to air at the maximum temperature and leads to an accelerated oxidation of the crack surface and the tip. This behaviour was investigated for the IP test on Nimonic 90 and for the TMF tests under offset conditions on both PM 1000 and Nimonic 90. To compare the PM 1000 lifetime results with the literature data of Ngala et al. [18], it was necessary to use material out of the same batch and the same initial microstructure. For example, Liu et al. [114] and Ngala et al. [18] report that oxidation typically takes place along surface cracks and penetrates intergranularly along transverse grain boundaries resulting in grain boundary crack propagation. Grain boundaries are preferred areas for surface diffusion due to the presence of easily-oxidised elements. The oxidation layer inside a crack can be seen in figure 5.31. The coinciding peaks of temperature and stress during the IP and the strain offset tests leads to a prefered intergranular crack mode. Due to the fact that the maximum temperature during the $\varphi = -135°$ phase-shifted tests is not synchronised to the maximum tension stress, the crack mode can vary. At a macroscopic scale the offset TMF tests have a nearly constant maximum stress level, in contrast to the compression peak values, figures 5.14 and 5.22. This can be explained by the oxidation of the crack, as mentioned above and seen in figure 5.31. Under OP cycling, the cracks are completely closed at the maximum temperature, and this leads to retarded oxidation and consequent retarded crack growth. The $\varphi = -135°$ phase-shifted tests lie between these limiting cases.

Under in-phase conditions, the superimposed additional strain leads to a slightly different hysteresis at the end of specimen's life. The shape of the hysteresis loops for IP and $\varphi = -135°$ tests is completely different. The IP tests support fast crack growth and cyclic crack opening at higher temperatures.

After the peak mechanical strain values ("B" and "D", figure 5.9) the plastic deformation reaches constant stress levels in compression and tension. At elevated tem-

peratures the superimposed thermal and mechanical strains have different directions. The thermal part is of superior importance to the mechanically induced strain, leading to larger linear ranges in the stress vs. plastic strain plot, as shown in figures 5.9a and 5.9b. To a limited extent, the high temperatures lead to recovery, which will be counteracted by the additional plastic deformation under compressive loadings. In the tension part of the cycle, the thermal elongation does not have such a strong influence because of the lower temperatures where recovery is not as effective. Under compression, the plastic deformation starts to change at $\varepsilon_m = 0$.

The fatigue life for Nimonic 90 can be described very well with the Manson Coffin relation for mechanical strain amplitudes higher than 0.5 %. Below this point the elastic deformation of the fatigue life is much more pronounced and higher lifetime values are reasonable, in accordance to the Basquin law, comp. figure 5.16. An equivalent behaviour could be observed for the ODS alloy for strains of 0.1 % and smaller 5.25.

The ODS-alloy fatigue behaviour is different to Nimonic. The cyclic hardening is attributed to an increased dislocation density due to the interaction of yttria particles with dislocations during plastic deformation [115, 116]. These fine yttria particles interact in a different way to precipitates in other second phase strengthened nickel base superalloys, such as Nimonic 90. All PM 1000 tests showed a constant increase of the resulting stress until the saturation zone of the test, where the stress is nearly in the tensile regime.

Because of the annealing and the very low dislocation density, plastic deformation is predominant in the first few cycles. During this period dislocations start to move and to build up a dislocation cell structure, leading to cyclic hardening. In general, polycrystalline metals can be characterised by an isotrop linear elasticity up to yield strength. A plastic material response can be investigated for higher stresses (hardening). By changing the loading direction the material responses nearly isotrop and linear elastic. Due to the increasing dislocation density, the plastic deformation starts earlier. This typical cyclic deformation behaviour can also be seen in TMF tests. The shift of the ratio between elastic and plastic strains in heating direction and at the transition from mean stress to maximum compression can be seen in figure 5.9b. This behaviour can be explained by

the equation 5.1, and is indicated by the lower slope of the curves. This is in contrast to the opposite direction, where nearly all the plastic deformation can be found at the high temperature part of the cycle. This effect is based to the temperature dependence of the Young's modulus and is also reported in the literature [11–13] for the start sequence of TMF tests. After the initial hardening phase a modest cyclic softening starts, attributable to reorganisation of the dislocation structure.

Single phase materials are typically characterised by such a cellular dislocation structure, e.g. copper. This effect was reported and explained by Gottstein [117] for nearly all fcc metals. As dislocations reorganise into a cellular structure, "dislocation free" areas are formed, where new dislocations can be generated. A splitting of the sub-grains leads to a mean size reduction.

6.3. Strain Offset

The influence of a mean strain of 0.75 % led to a reduction in time to failure of a factor of around 10, [37, 109], over the full amplitude range for PM 1000 tests. For the Nimonic 90 tests a similar offset led to a reduction in life by a factor of about 3 for the single amplitude (0.5 %) investigated. This drastic reduction in life can be attributed to the fact that the mean stress and mean strain are both well into the tensile region.

Both types of offset tests (Nimonic 90 and PM 1000) showed a cyclic hardening during the low temperature half of the cycle, figures 5.14 and 5.22. This can be explained by enhanced dislocation rearrangement and recovery at higher temperature, since dislocation climb and cross-slip are both thermally activated processes. During the low temperature part of the cycle the restructured grains are smaller in size, resulting in an increased yield stress.

The interaction of yttria particles with dislocations, reported by Ngala et al. [18], Linde and Henderson [115], Arzt and Schröder [118], which should lead to an increased dislocation density due to the plastic deformation could not be observed for the

tests performed. Despite of the strong interactions between the dislocations and the small incoherent dispersoide particles, the deformation behaviour also strongly depends on interactions of the dislocation network. The formation of this complex three-dimensional structure is usually suppressed until a specific level by the dispersoides, depending on the stress amplitude. The dislocation structure cannot adapt rapidly enough to follow the varying applied loads. This leads to an established dislocation arrangement of a corresponding average strain [21].

Even the absence of strengthened particles in Nimonic 90 leads to the same hardening effect, figure 5.13. During the initial 50 cycles this effect can be specified with $\approx 50\,\mathrm{MPa}$. In contrast to that, the small yttria particles of PM 1000 do not affect the high applied strain amplitudes. A typical recovering of the dislocation structure can be excluded. The temperature-plastic strain plot of figure 5.12 shows the plastic deformation to be tensile throughout the cylce. The resulting compressive stresses are attributed to the superposition of thermal and elastic strains and are too small for starting any compressive plastic deformation. The second peak in the tensile plastic strain can be identified as the reason for the dramatic lifetime reduction.

At higher temperatures during the compression part of the cycles, creep and a stress relaxation could be observed, attributable to decreasing dispersion strengthening at elevated temperatures. Arzt [119] has reported a reduction in creep strength by a temperature increase of ODS superalloys. Furthermore he reports of creep damages by void formation along grain boundaries, usually formed during the high temperature deformation of TMF cycling. The typical void formation after creep could not be observed. The crack initiation during the lower temperature half occurs when a critical dislocation density has been obtained due to plastic strains. Because of to the phase shift, the highest damage occurs at maximum compression ($\approx 750\,^{\circ}\mathrm{C}$) and at maximum tension ($\approx 510\,^{\circ}\mathrm{C}$). The continuous increase of the maximum stresses of PM 1000 is the result of this creep under compressive loading. During the saturation zone the dispersoides cause slip dispersal, resulting in homogeneous deformation [120], and do not produce detectable microstructural changes.

The Nimonic 90 investigations with offset condition leads to plastic deformation

peaks twice in each cycle, one in the lower temperature part at the tensile peak and the second at the high temperature part of the cycle due to the superimposed peak thermal strain with the offset mechanical strain, figure 5.12. This leads to high rates of change of strain during elevated temperatures and, critically, a second deformation peak in the cycle. Therefore the reduction of lifetime could be determined by a factor of ≈ 3, comparing with non-offset conditions.

Generally, Nimonic 90 and PM 1000 shows a different behaviour during saturation. The cyclic hardening effect can be calculated by the transient stress ratio. For both test batches it is shown in figure 5.8 and 5.21. This factor increases for higher strain amplitude at Nimonic 90 and is nearly stable for the PM 1000 samples. The offset strain leads to a premature damage during initial cycling. Therefore the plastic deformation capacity of the material is reduced to a small part and the crack initiation and propagation start earlier. Another important factor is the resulting mean stress. At all non-offset phase shifted ($\varphi_m = -135°$) conditions the observed mean stress was nearly zero. Changing the phase as well as the strain offset leads to an increase of this stress level, ranging from compression to tension.

6.4. Microstructural Effects

The grain boundaries of the IP test specimen were damaged by the high temperature during the tension part of the cycle. Fast crack growth aggravated by oxidation leads to more an opening of the grain boundaries ahead of the crack tip as was observed under in-phase conditions. Intergranular cracking during in-phase TMF testing has been widely observed and attributed to oxidation and creep [121–123]. For example, Liu et al. [114] have reported that oxidation takes place along transgranular surface cracks and intergranular transverse grain boundaries, leading to a grain boundary crack propagation. Grain boundaries are areas where enhanced diffusion can occur and therefore can show accelerated crack growth due to oxidation. Additionally, they present favourable oxidation paths due to the presence of easily oxidised elements. Fractography and examination of crack

initiation sites showed oxidation layer formed on the surface of the in-phase tests. Since such a layer is absent for the non-IP tests, this must be associated with exposure of the fracture surface to oxygen at the peak temperature. The mismatch of Young's modulus and the thermal expansion coefficients between the oxide layer and the underlying meterial induces strains and causes fracture of the oxidation layer, which when it occures at the crack tip, exposes fresh metal to oxidation and hence enhanced crack propagation.

In all samples, the crack path was perpendicular to the specimen axis. The crack tip was found either in the grains or at the grain boundaries, indicating trans-granular or intergranular propagation depending on the loading mode.

The ODS alloy showed a microstructure indistinguishable from the initial state for the whole experiment, with no perceptible change in the grain size. Striations at the fracture surface indicated zones of high plastic deformation. The similarity of the $\varphi = -135°$ test to the out-of-phase conditions can be also found in the crack surfaces, according to Marchionni et al. [109]. All investigated TMF cycling resulted in a visible large macrocrack arising from fast brittle fracture without any necking.

6.5. Creep Behaviour of NiAl

The analysis of the creep results shows that the assumption of a constant thickness during a test series, as mentioned in section 4.2.3 as the basis for the true stress calculation, is an acceptable method. All specimens showed neck formation only in direction of specimen width. Figure 5.46 shows a little or no necking in the thickness direction and a nearly constant thickness, figures 5.48 and 5.49. The reason for this effect is the larger quantity of grains in longitudinal direction, including more microstructural slip systems than in thickness direction, which would contain a maximum of two grains due to the thin samples (0.1 mm).

The insensitivity of this material to the changed load levels can be attributed to the coarse grain microstructure, so that creep is typically dominated by dislocation mecha-

nisms at high stresses. This mechanism was observed indirectly in the SEM investigations and by the precense of pores and cavities, characteristic of dislocation based creep. The observed necking leads to local concetration of the strain. Hence, for the following calculation the region of interest has to be located in the fractured area.

Due to the very wavy, brittle and thin specimen, the NiAl films can be predamaged by oscillations before starting any creep test, which could have affected the time to failure. An incremental load change technique was used to obtain more data from the limited specimen number. Therefore, a direct time to failure cannot be obtained for any load steps. Analysis of creep data was performed using the Monkman-Grant relation.

Because to the specimen is only two grains wide, the internal stress distribution can lead to unintentional horizontal oscillation, measurable by having LVDTs on both sides of the specimen. By using low pass filters and calculating the mean value, these oscillations were nearly eliminated.

An oxide layer was not detectable by EDS. Typical dislocation creep mechanisms were observed on the fracture surface of the specimen. Following the main creep laws from section 2.1.3 all constants were measured and determined.

Some of the scatter in the measured data is related to the markers, which degrade during the test. The image analysis routine recognises the marker's shape, but the resulting outline becomes less sharp with time leading to a change in the calculated centre of geometry. By this method the strain distribution could be abserved any changes in Poisson's ratio during the test.

The results of the creep tests can be summarised as follows:

- Creep cracks always start at pre-existing pores and propagate perpendicular to the loading axis.
- NiAl creep can be adequately described by classic creep relations within the range of the limitied specimen number.

- The creep exponent is around 4 as determined from a Norton plot.
- The use of optical deformation measurement equipment is of considerable benefit in investigating these thin and brittle specimens.

7. Conclusions

Thermal mechanical fatigue tests have been performed on two different materials: Nimonic 90, as a well established alloy, and PM 1000 as a new oxide dispersoid strengthened material. Tests with in-phase, $\varphi = -135°$ phase shifted as well as phase shifted with an additional mean strain were performed. The basis for these tests was the European Code of Practise used because it provides comparability of test results between institutes.

The in-phase test was used as a benchmark for the experiment and gave results, very close to those of others. The most detrimental effect on the IP lifetime was the combination of internal crack oxidation and corresponding intergranular fracture mode. This effect can be further aggravated by the superposition of a positive mean strain, which leads to a dramatic reduction of the lifetime even at smaller mechanical loadings by a factor of 10^2 and more, found for the PM 1000.

The interaction between creep and oxidation leads to this decreasing lifetime, compared to tests where these parameters are not dominant. The Nimonic 90 $\varphi = -135°$ phase shifted tests without such a mean strain have nearly the same fatigue behaviour, reported in literature for out-of-phase investigations. Due to the high mechanical strain amplitudes the strengthening effect of the small yttria particles could not be measured. For the specimens investigated, the dominant fatigue damage mechanism is based on the dislocation rearrangement. The in-phase and the phase shifted TMF tests lead to larger tensile stresses and therefore to a dramatic reduced lifetime, due to the complex tensile stress situation, creep and oxidation behaviour.

For these investigations a new set up was designed and implemented with the focus on precision and simulation thermal transients. This leads to lower thermally induced

stresses than in conventional set-ups, as demonstrated by the zero-stress-test. Inaccurate temperatures strongly influence any experimental results, particularly the measured lifetime. Typical TMF test rigs use different temperature controlling techniques, normally industrial controllers, which are not configured for such high temperature transients. These systems are unable to recognise a growing oxidation layer, leading to an increased temperature at higher cycle numbers. Other disadvantages of these test rigs are the limited temperature rate with high overshoots and the insensitivity to external thermal interference.

The thermal controlling equipment used for these investigations consisted of a special real time temperature controller with a separate PC for data handling and all operation sequences. All the software was prepared directly to the possibilities of the used hardware and ensures fast data acquisition and controlling. Finally, the developed test rig was benchmarked with the European Code-of-Practise for TMF tests and shows completely comparable results. Zero-stress-tests are required as another benchmark for every test series, showing very small deviations in the resulting stress amplitudes. Due to the variability of this design, creep investigations could also be carried out at thin film specimens of β-NiAl.

The coating material β-NiAl was phenomenologically characterised by the classical creep relations. Load changes at comparable temperatures to the TMF tests resulted in local creep rate minima, providing the basis for subsequent time-to-failure analysis. These separate investigations can be used as the basis for a more detailed material selection and future blade design.

Index

W

Z

Bibliography

[1] J. HAMMER. *Kriech- und Zeitstandsverhalten der einkristallinen Nickelbasis-Superlegierung SRR99 unter besonderer Berücksichtigung der mirkrostrukturellen Vorgänge und der Materialfehler*. PhD thesis, Universität Erlangen-Nürnberg, 1990.

[2] P. HÄHNER, E. E. AFFELDT, T. BECK, H. KLINGELHÖFFER, M. LOVEDAY, AND C. RINALDI. Validated Code-of-Practise for Strain-Controlled Thermo-Mechanical Fatigue Testing. Joint-Research Centre, June 2006.

[3] H.-J. CHRIST. Effect of environment on thermomechanical fatigue life. *Mater. Sci. Eng., A*, 468-470:98 – 108, 2007. The McEvily Symposium: Fatigue and Fracture of Traditional and Advanced Materials, TMS 2006.

[4] P. MAJERUS. *Neue Verfahren zur Analyse des Verformungs- und Schädigungsverhaltens von MCrAlY-Schichten im Wärmedämmschichtsystem*. PhD thesis, Fakultät für Maschinenwesen der Rheinisch-Westfälischen Technischen Hochschule Aachen, July 2003.

[5] E. E. AFFELDT, J. HAMMER, U. HUBER, AND H. LUNDBLAD. Analysis of Thermal Gradients during Cyclic Thermal Loading under High Heating Rates. In *Thermomechanical Fatigue Behavior of Materials*, volume 4, 2003.

[6] T. BECK, V. BICEGO, T. BRENDL, P HÄHNER, AND M. MACHIONNI. TMF-Standard Project - Draft. TMF-Standard Project, March 2004.

[7] J. SCHIJVE. *Fatigue of Structures and Materials*. Kluwer Academic Publishers, 2001.

[8] S. SURESH. *Fatigue of Materials*. Cambridge University Press, 2001.

[9] H. MUGHRABI. Dislocations in fatigue. In *Dislocations and Properties of real Materials*, 323, pages 244–261. The Institute of Metals, London, 1985.

[10] H.-J. CHRIST. *Wechselverformung von Metallen*, volume 1. Springer Verlag Berlin, February 1991.

[11] F. GRUBE. *Zum Einfluß platinmodifizierter Aluminidschichten auf das thermo-mechanische Ermüdungsverhalten einer einkristallinen Nickelbasis-Superlegierung*. Phd thesis, Friedrich-Alexander-University Erlangen-Nürnberg, Germany, April 2003.

[12] E. E. AFFELDT. Influence of an aluminide coating on the TMF life of a single crystal nickel-base superalloy. *Transactions of ASME, Joural of Engineering for Gas Turbines and Power*, 121:687–690, 1998.

[13] D. J. ARRELL, J. BRESSERS, AND J. TIMM. Effect of cycle history on thermo-mechanical fatigue response of nickel-base superalloys. In *AMSE-IMCE 99 Symposium on High Temperature Applications, International Mechanical Engineering Congress and Exhibition, American Society of Testing and Materials*, pages 1–6, 1999.

[14] O. BASQUIN. The exponential law of endurance tests. In *Proceedings of the American Society for Testing and Materials*, volume 10, pages 625–630, 1910.

[15] S. S. MANSON. Behaviour of materials under conditions of thermal stress. NACA TN 2933, 1954.

[16] L. COFFIN. A study of the effects of cyclic thermal stresses on a ductile metal. *Transactions of the American Society of Mechanical Engineers*, 76:931–940, 1954.

[17] H.-J. CHRIST, F. O. R. FISCHER, AND H. J. MAIER. High-temperature fatigue behavior of a near-γ titanium aluminide alloy under isothermal and thermomechanical conditions. *Mater. Sci. Eng., A*, 319-321:625–630, December 2001.

[18] W. O. NGALA, G. BIALLAS, AND H. J. MAIERAFFELDT. Isothermal and thermomechanical fatigue behavior of the ODS superalloy PM 1000. In E.E. GDOUTOS, editor, *Proceedings International Conference of Fracture (ECF 16): Fracture of Nano and Engineering Materials*. Springer, Dordrecht, The Netherlands, 2006.

[19] G. PITZ, T. BECK, K.-H. LANG, AND D. LÖHE. Thermisch- mechanisches und isothermes Ermüdungsverhalten der Nickelbasis - Superlegierung IN 792 CC. *Materialwissenschaft und Werkstofftechnik*, 28(3):142–148, 1997.

[20] C. C. JR. ENGLER-PINTO, H. SEHITOGLU, AND H. J. MAIER. Cyclic behavior of A1319-T7B under isothermal and non-isothermal conditions. In *Thermomechanical Fatigue Behavior of Materials, 4th Volume*, 2003.

[21] M. HEILMAIER, H. J. MAIER, A. JUNG, M. NGANBE, F. MÜLLER, AND H.-J. CHRIST. Cyclic stress-strain response of the ODS nickel base, superalloy PM 1000 under variable amplitude loading at high temperatures. *Mater. Sci. Eng., A*, 281: 37–44, 2000.

[22] M. HEILMAIER, M. NGANBE, B. BECKERS, H. G. BROKMEIER, R. TAMM, C. G. OERTEL, AND W. SKROTZKI. Plastic anisotropy of textured ODS nickel-base alloy PM 1000. *Materials Science and Engineering A*, 319-321:290–293, December 2001.

[23] F. E. H. MÜLLER, M. HEILMAIER, AND L. SCHULTZ. The influence of texture and grain structure on the high temperature low-cycle fatigue behaviour of the ODS nickel-based superalloy PM 1000. *Materials Science and Engineering A*, 234-236: 509–512, August 1997.

[24] H. J. MAIER. Environmental effects on the isothermal and thermomechanical fatigue behavior of γ-near-titanium aluminide. In *Thermomechanical Fatigue Behavior of Materials, 4th Volume*, 2002.

[25] E. E. AFFELDT. MTU Aero Engines GmbH, Munich, Germany, private communication, 2003-2006.

[26] H.-J. KÜHN, O. KAHLCKE, AND S. BROOKES. A practicable nominal temperature tolerance for TMF-tests. *Int. J. Fatigue*, 30(2):277 – 285, 2008. High Temperature Thermo-mechanical Fatigue: Testing Methodology, Interpretation of Data, and Applications.

[27] E. E. AFFELDT. Strain Gradients and related induced Stresses due to temperature fields during Thermal Mechanical Fatigue Testing. In G. BIALLAS, H. J. MAIER, O. HAHN, K. HERRMANN, AND F. VOLLERTSEN, editors, *Camps 2002*. Institut für Prozess- und Werkstofftechnik Paderborn, April 2002.

[28] P. HÄHNER, C. RINALDI, V. BICEGO, E. E. AFFELDT, TH. BRENDEL, H. ANDERSSON, T. BECK, H. KLINGELHOFFER, H.-J. KUHN, A. KOSTER, M. LOVEDAY, M. MARCHIONNI, AND C. RAE. Research and development into a european code-of-practice for strain-controlled thermo-mechanical fatigue testing. *Int. J. Fatigue*, 30(2):372 – 381, 2008. High Temperature Thermo-mechanical Fatigue: Testing Methodology, Interpretation of Data, and Applications.

[29] M. S. LOVEDAY, V. BICEGO, P. HÄHNER, H. KLINGELHÖFFER, H.-J. KUHN, AND B. ROEBUCK. Analysis of a european TMF inter-comparison exercise. *Int. J. Fatigue*, 30(2):382 – 390, 2008.

[30] G. BIALLAS, H.J. MAIER, O. HAHN, K. HERRMANN, AND F. VOLLERTSEN. High temperature fatigue. In *High Temperature Fatigue*. University of Paderborn, Bonifatius GmbH, Paderborn, 2002.

[31] K. DURST, O. FRANKE, H. W. HÖPPEL, E. E. AFFELDT, AND M. GÖKEN. Mikrostruktur und lokale mechanische Eigenschaften von platinmodifizierten Alu-

minidschichten auf Nickelbasis- Superlegierungen nach thermomechanischer Ermüdung. *Praktische Metallographie (Sonderband)*, 36:117–122, 2004.

[32] T. BECK. University of Karlsruhe, Germany, private communication, 2005-2006.

[33] T. BECK, K.-H. LANG, AND D. LÖHE. Thermal-mechanical fatigue behaviour of cast aluminium alloys for cylinder heads reinforced with 15 vol. *Mater. Sci. Eng., A*, 319-321:662–666, December 2001.

[34] K. RAU, T. BECK, AND D. LÖHE. Isothermal, thermal-mechanical and complex thermal-mechanical fatigue tests on AISI 316 L steel-a critical evaluation. *Mater. Sci. Eng., A*, 345(1-2):309–318, March 2003.

[35] R. P. SKELTON. Hysteresis, yield, and energy dissipation during thermomechanical fatigue of a ferritic steel. *Int. J. Fatigue*, 26(3):253–264, March 2004.

[36] R. NÜTZEL, E. AFFELDT, AND M. GÖKEN. Damage evolution during thermomechanical fatigue of a coated monocrystalline nickel-base superalloy. *International Journal of Fatigue*, 30(2):313 – 317, 2008. High Temperature Thermomechanical Fatigue: Testing Methodology, Interpretation of Data, and Applications.

[37] M. MARCHIONNI, G. ONOFRIO, T. RANUCCI, K. RAU, T. BECK, H.-J. KÜHN, H. KLINGELHÖFFER, E. E. AFFELDT, L. CERDAN DE LA CRUZ, A. KOSTER, H. ANDERSSON, E. SJÖSTRÖM, S. PAHLAVANYALI, A. RAYMENT, AND C. RAE. Workpackage 3 Report - the route to standardisation, June 2004.

[38] V. KOVAN, J. HAMMER, R. MAI, AND M. YÜKSEL. Modelling of High Temperature Fatigue Life of Oxide Dispersion Strengthened Nickel-Based Superalloy PM1000 by Artificial Neural Network. *Materials at High Temperatures*, 25(2): 81–88, July 2008.

[39] TH. BRENDEL, E. E. AFFELDT, J. HAMMER, AND CH. RUMMEL. Temperature gradients in TMF specimens. measurement and influence on TMF life. *Int. J. Fatigue*, 30(2):234 – 240, 2008.

[40] T. BECK, G. PITZ, K.-H. LANG, AND D. LÖHE. Thermal-mechanical and isothermal fatigue of IN 792 CC. *Mater. Sci. Eng., A*, 234-236:719–722, August 1997.

[41] E. FLEURY AND J. S. HA. Thermomechanical fatigue behaviour of nickel base superalloy in738lc. *Mater. Sci. Technol.*, 17(9):1087–1092, September 2001.

[42] K. S. KIM AND R. H. VAN STONE. Crack growth under thermo-mechanical and temperature gradient loads. *Engineering Fracture Mechanics*, 58(1-2):133–147, September 1997.

[43] J. LLORCA. High temperature fatigue of discontinuously-reinforced metal-matrix composites. *Int. J. Fat.*, 24(2-4):233–240, 2002.

[44] S. MALL, J. T. ROUSH, AND W. H. VAUGHT. Thermo-mechanical fatigue behavior of an angle-ply SCS-6/Ti-15-3 metalmatrix composite. *Composites Science and Technology*, 52 (1):47–59, 1994.

[45] F. C. NEUNER, U. TETZLAFF, AND H. MUGHRABI. Enhancement of thermomechanical fatigue resistance of a monocrystalline nickel-base superalloy by prerafting. In *Thermomechanical Fatigue Behavior of Materials, 4th Volume*, 2002.

[46] L. QIAN, Z.-G. WANG, H. TODA, AND T. KOBAYASHI. High temperature low cycle fatigue and thermo-mechanical fatigue of a 6061Al reinforced with SiCW. *Mater. Sci. Eng., A*, 291(1-2):235–245, October 2000.

[47] M. BAYERLEIN, W. HARTNAGEL, AND C. SOMMER. Phenomenological damage parameters for TMF life prediction of DS CM 247 LC. In J. BRESSERS AND L. RÉMY, editors, *Fatigue under thermal and mechanical loading: mechanisms, mechanics and modelling*, pages 109–118. Kluwer, 1995.

[48] C. SOMMER, M. BAYERLEIN, AND W. HARTNAGEL. Deformation and failure mechanisms of DS CM 247 LC under TMF and LCF loading. In *Proceedings of the 81st AGARD Conference on Thermal Mechanical Fatigue of Aircraft Engine Materials*, volume AGARD-CP-569, page 11/12, Banff, Canada, Oct. 2–4 1995.

[49] S. A. KRAFT AND H. MUGHRABI. Thermo-mechanical fatigue of the monocrystalline Nickel-base superalloy CMSX-6. In M.J. VERRILLI AND M.G. CASTELLI, editors, *Thermo-mechanical Fatigue Behaviour of Materials*, volume 2, pages 27–40. American Society for Testing and Materials, 1996.

[50] D. A. BOISMIER AND H. SEHITOGLU. Thermo-mechanical fatigue of MAR-M247: Part I - Experiments, Transactions of the ASME. *Journal of Engineering Materials and Technology*, 112:68–79, 1990.

[51] M. ARANA, J. M. MARTINEZ-ESNAOLA, AND J. BRESSERS. Crack propagation and life prediction in a Nickel-based superalloy under TMF-conditions. In J. BRESSERS AND L. RÉMY, editors, *Fatigue under thermal and mechanical loading: mechanisms, mechanics and modelling*, pages 393–402. Kluwer Academic Publishers, 1996.

[52] M. MARCHIONNI, D. RANUCCI, AND E. PICCO. *Influence of cycle shape and specimen geometry on TMF of an ODS nickel-base superalloy*, chapter Fatigue under thermal and mechanical loading: mechanisms, mechanics and modelling, pages 169–178. Kluwer Academic Publishers, 1996.

[53] M. OKAZAKI AND M. SAKAGUCHI. Thermo-mechanical fatigue failure of a single crystal Ni-based superalloy. *Int. J. Fatigue*, 30(2):318 – 323, 2008. High Temperature Thermo-mechanical Fatigue: Testing Methodology, Interpretation of Data, and Applications.

[54] R. BÜRGEL. *Handbuch der Hochtemperaturwerkstofftechnik*, volume 3. Vieweg, 2006.

[55] P. GUILLERY, R. HETZEL, AND B. REPPICH. *Werkstoffkunde für die Elektrotechnik*. Vieweg, Braunschweig, Wiesbaden, 1983.

[56] J. RÖSLER, H. HARDERS, AND M. BÄKER. *Mechanisches Verhalten der Werkstoffe*. Teubner, 2006.

[57] J. HANNAH AND M. J. MILLER. *Mechanical Engineering Science*. Prentice Hall, 1999.

[58] F. C. MONKMAN AND N. J. GRANT. Proceedings ASTM. volume 56, pages 593–605, 1956.

[59] A. BALDAN. Effects of carbides and cavitation on the Monkman-Grant ductility of a nickel-base superalloy. *Journal of Materials Science Letters*, 11(19):1315–1318, January 1992.

[60] H. CHEN. Mechanisches Verhalten und mikroskopische Mechanismen bei der Nickelbasissuperlegierung IN738LC bei hohen Temperaturen unter Kriech- und Ermüdungsbeanspruchung. In *Schriftenreihe Werkstoffwissenschaften*, volume 6, pages 3–6. Verlag Dr. Köster, 1995.

[61] D. C. DUNAND, B. Q. HAN, AND A. M. JANSEN. Monkman-Grant Analysis of Creep Fracture in Dispersion-Strengthened and Particulate-Reinforced Aluminum. *Metallurgical and Materials Transactions A*, 30A:829, 1999.

[62] S. V. RAJ. Tensile creep fracture of polycrystalline near-stoichiometric nial. *Materials Science and Engineering A*, 381(1-2):154–164, September 2004.

[63] P. KOFSTAD. Fundamental aspects of corrosion by hot gases. *Materials Science and Engineering A*, 120-121(Part 1):25–29, November 1989.

[64] S. YOSHITAKE, V. NARAYAN, H. HARADA, H. K. D. H. BHADESHIA, AND D. J. C. MACKAY. Estimation of the γ and γ' Lattice Parameters in Nicke-base Superalloys Using Neural Network Analysis. *ISIJ International*, 38:495–502, 1998.

[65] G. A. ZICKLER. Quantitative Analyse des Ausscheidungsverhaltens in der Nickelbasislegierung Nimonic 80a mittels Röntgen- und Neutronenkleinwinkelstreuung. Master's thesis, Montanuniversität Leoben, Institut für Metallphysik, Erich-Schmid-Institut für Materialwissenschaft, March 2002.

[66] TH. BRENDEL. MTU Aero Engines GmbH, Munich, Germany, private communication, 2003-2006.

[67] H.-J. CHRIST. University of Siegen, Germany, private communication, 2006.

[68] V. BICEGO AND N. RICCI. Workpackage 2 Report - Material Procurement, October 2001.

[69] Y. ESTRIN, M. HEILMAIER, AND G. DREW. Creep properties of an oxide dispersion strengthened nickel-base alloy: the effect of grain orientation and grain aspect ratio. *Materials Science and Engineering A*, 272(1):163–173, November 1999.

[70] R. F. SINGER AND E. ARZT. Structure, Processing and Properties of ODS Superalloys. In W. BETZ, R. BRUNETAUD, D. COUTSOURADIS, H. FISCHMEISTER, T.B. GIBBONS, I. KVERNES, I. LINDBLOM, J.B. MARRIOTT, AND D.B. MEADOWCROFT, editors, *High Temperature Alloys for Gas Turbines and Other Applications*, pages 97–126. Reidel Dordrecht, 1986.

[71] S. WEINBRUCH, A. ANASTASSIADIS, H. M. ORTNER, H. P. MARTINZ, AND P. WILHARTITZ. On the Mechanism of High-Temperature Oxidation of ODS Superalloys: Significance of Yttrium Depletion Within the Oxide Scales. *Oxid. Met.*, 51(1):111–128, February 1999.

[72] PLANSEE GMBH. Dispersion-strengthened high-temperature materials. Technical report, PLANSEE GmbH, Lechbruck, Germany, 2004.

[73] H. BÖNNEMANN, W. BRIJOUX, H. W. HOFSTADT, T. OULD-ELY, W. SCHMIDT, B. WASSMUTH, AND C. WEIDENTHALER. Nasschemische Synthese von β-Nickelaluminid NiAl. *Angewandte Chemie*, 114(4):628–632, 2002.

[74] F. GRUBE, E. E. AFFELDT, AND H. MUGHRABI. Thermomechanical fatigue behavior of an aluminide-coated monocrystalline Ni-Base superalloy. In *Thermomechanical Fatigue Behavior of Materials, 4th Volume*, 2002.

[75] Y. H. ZHANG, D. M. KNOWLES, AND P. J. WITHERS. Microstructural development in Pt-aluminide coating on CMSX-4 superalloy during TMF. *Surf. Coat. Technol.*, 107(1):76–83, August 1998.

[76] H. B. XU, S. K. GONG, AND H. B. GUO. Hot-fatigue behaviour of thermal barrier coatings by EB-PVD. In *High-Temperature Fatigue CAMP*, 2002.

[77] P. WELLNER. *Thermo-Mechanical Behavior of NiAl Thin Films*. PhD thesis, University of Stuttgart, December 2003.

[78] E. TZIMAS, H. MULLEJANS, S. D. PETEVES, J. BRESSERS, AND W. STAMM. Failure of thermal barrier coating systems under cyclic thermomechanical loading. *Acta Mater.*, 48(18-19):4699–4707, December 2000.

[79] L. RÉMY, A. M. ALAM, AND A. BICKARD. Thermo-mechanical creep-fatigue of coated systems. In *Thermomechanical Fatigue Behavior of Materials, 4th Volume*, 2002.

[80] W. SCHMIDT AND G. LEHNERT. Ductility of metallic diffusion type coatings on nickel-based alloys and its determination. *Materialwissenschaft und Werkstofftechnik*, 15(3):73–82, 1984.

[81] V. P. SERGEEV, M. V. FEDORISCHEVA, A. V. VORONOV, N. A. POPOVA, AND E. V. KOZLOV. Mechanical properties and microstructure of intermetallic coating on the basis of the Ni-Al system. In *Science and Technology, 2004. KORUS 2004. Proceedings. The 8th Russian-Korean International Symposium on*, volume 3, pages 153–157, June, 26 – July, 3 2004.

[82] Y. TAMARIN. *Protective Coatings for Turbine Blades*, volume 1. ASM International, September 2002.

[83] E. M. GRALE. *Mechanical Properties of Intermetallic Compounds*, chapter Research into NiAl and Ni_3Al, pages 266–299. J. H. Westbrook, 1960.

[84] J. RIETHMÜLLER. Mikrostruktur und mechanische Eigenschaften von Haftvermittlerschichten auf NiAl-Basis. Master's thesis, Institut für Metallkunde, Universität Stuttgart, July 2004.

[85] F. KLOCKMANN. *Lehrbuch der Mineralogie*. Ferdinand Enke Verlag, 1978.

[86] D. B. MIRACLE. The physical and mechanical properties of NiAl. *Acta Metallurgica et Materialia*, 41(3):649–684, March 1993.

[87] TH. B. MASSALSKI. *Binary alloy phase diagrams*, volume 3. Materials Park: ASM Internat., 2 edition, 1992.

[88] K. BOUHANEK, O. A. ADESANYA, F. H. STOTT, P. SKELDON, D. G. LEES, AND G. C. WOOD. Isothermal and Thermal Cycling Behaviour of Thermal Barrier Coatings: Pt Aluminide Bond Coats. *Materials at High Temperature*, 17:185–196, 2000.

[89] W. J. QUADAKKERS, A. K. TYAGI, D. CLEMENS, R. ANTON, AND L. SINGHEISER. The Significance of Bond Coat Oxidation for the Life of TBC Coatings. In N.B. DAHOTRE AND J. HAMPIKIAN, editors, *Elevated Temperature Coatings: Science & Technology III*, pages 119–130, 1999.

[90] P. S. LIU, K. M. LIANG, AND S. R. GU. Failure Behavior of an Aluminide Coating on a Co-Base Superalloy during High-Temperature Oxidation in Air. *Oxidation of Metals*, 54(3):277–283, October 2000.

[91] H. ECHSLER. *Oxidationsverhalten und mechanische Eigenschaften von Wärmedämmschichten und deren Einfluss auf eine Lebensdauervorhersage*. PhD thesis, RWTH Aachen, Germany, July 2003.

[92] SPECIAL METALS CORPORATION. Product handbook of high performance alloys. Technical report, New Hartford, NY and Huntington, WV, U.S.A., and Hereford, United Kingdom., 2001.

[93] Y. ZHANG, J. A. HAYNES, B. A. PINT, I. G. WRIGHT, AND W. Y. LEE. Martensitic transformation in CVD NiAl and (Ni,Pt)Al bond coatings. *Surf. Coat. Technol.*, 163-164:19–24, 2003.

[94] E. WECK AND E. LEISTNER. *Metallographic instructions for colour etching by immersion, part 3*. D.V.S.-Verlag Germany, 1982.

[95] G. PETZOW. *Metallographisches, keramographisches, plastographisches Ätzen*. Gebrüder Borntraeger, 2006.

[96] CH. KLIEMT. Microstructural investigations of a nickel based superalloy after TMF testing. Diploma thesis, October 2007.

[97] R. MARQUARDT AND P. HÄHNER. Survey of strain-controlled TMF testing practices. Technical report, MTU, Germany Joint Research Centre Petten, The Netherlands, October 2001.

[98] TH. BRENDEL, M. NADERHIRN, L. DEL RE, AND CH. SCHWAMINGER. Improving the reproducibility and control accuracy of TMF experiments with high temperature transients. In *Thermomechanical Fatigue Behavior of Materials, 4th Volume*, 2002.

[99] L. WEICHERT. *Technical Temperature Measurement*. Expert Verlag, Sindelfingen, 4th edition, 1987.

[100] PLUSTHERM POINT GMBH, WETTINGEN, SWITZERLAND. Private communication, 2003-2005.

[101] G. BENKOWSKY. *Induktionserwämung*. Verlag Technik GmbH, Berlin, 2002.

[102] R. MAI. Design and set-up of an induction heating system to investigate thermal gradients during fast temperature changes. Diploma thesis, December 2002.

[103] INFRATEC GMBH. *Manual of Thermographic System "VARIOScan 3021ST"*. Infratec GmbH, Dresden, Germany, 2003.

[104] MTS CORP. *Manual of Multi Purpose Testware of TestStar IIs*. MTS Corp., Minneapolis, USA, 2003.

[105] S. DENDORFER. University of Applied Sciences Regensburg, Germany, private communication, 2004-2008.

[106] V. KOVAN, J. HAMMER, R. MAI, AND M. YÜKSEL. Thermal-mechanical fatigue behaviour and life prediction of oxide dispersion strengthened nickel-based superalloy PM1000. *Materials Characterization*, 59(11):1600 – 1606, 2008.

[107] J. JARVIS AND C. ROBERTS. A new technique for displaying continuous tone images on a bilevel display. *IEEE Transactions on Communications*, 24(8):891–898, August 1976.

[108] R. STEINBRECHER. *Bildverarbeitung in der Praxis*. DBV-Verlag, München, Wien, 1993.

[109] M. MARCHIONNI, H. KLINGELHÖFFER, H. KÜHN, T. RANUCCI, AND K. MATZAK. Thermo-mechanical Fatigue of the Nickel-Base Superalloy Nimonic 90. *Key Engineering Materials*, 345–346:347–350, August 2007.

[110] ASTM. A standard practise for strain controlled thermomechanical fatigue testing. Joint Research Centre, Petten, June 2006.

[111] N. ZELINSKI. MTS Systems GmbH, Berlin, Germany, private communication, 2003-2006.

[112] T. ANGETTER. Creep behaviour of thin film nickel aluminides. Diploma thesis, February 2008.

[113] G. F. HANCOCK AND B. R. MCDONNEL. Diffusion in the intermetallic compound NiAl. *Physica Status Solidi (a)*, 4(1):143–150, 1971.

[114] F. LIU, S. H. AI, Y. C. WANG, H. ZHANG, AND Z. G. WANG. Evolutionary stress cycle behaviour and damage mechnisms in nickel based superalloy under thermomechanical fatigue. *Material Science and Technology*, 19:853–858, 2003.

[115] L. LINDE AND P. J. HENDERSON. Thermo-mechanical fatigue of an oxide dispersion strengthened Ni-Cr alloy and its effect on hysteresis loop shape. *Scripta Metallurgica et Materialia*, 26(11):1687–1692, June 1992.

[116] D. ELZEY AND E. ARZT. Crack initiation and propagation during high-temperature fatigue of oxide dispersion-strengthened superalloys. *Metallurgical and Materials Transactions A*, 22(4):837–851, April 1991.

[117] G. GOTTSTEIN. *Physikalische Grundlagen der Materialkunde*. Springer Verlag, 3rd edition, 2007.

[118] E. ARZT AND J. H. SCHRÖDER. High temperature strength of ODS superalloys due to dispersoid interaction. In W. BETZ AND M. YAMAZAKI, editors, *High temperature alloys for gas turbines and other applications*, pages 1037–1048. Liege-Riedel, The Netherlands, 1986.

[119] E. ARZT. Creep of Dispersion Strengthened Materials: A Critical Assessment. *Res Mechanica*, 31:399–453, 1991.

[120] F. E. H. MÜLLER, M. NGABE, H. J. KLAUSS, AND M. HEILMAIER. Monotonic and high temperature deformation behavior of the ODS nickel-base superalloy PM 1000. *Journal of Advanced Materials*, 32:9–20, 2000.

[121] P. J. HENDERSON, J. LINDBLOM, AND B. IVARSSON. Thermo-mechanical and low-cycle fatigue of MA 754. In E. BACHELET, R. BRUNETAND, AND D. COUTSOURADIS, editors, *High Temperature Materials for Power Engineering*, pages 1151–1162, Kluwer Academic, Dordrecht, 1990.

[122] J. J. STEPHENS AND W. D. NIX. The effect of grain morphology on longitudinal creep properties of INCONEL MA 754 at elevated temperatures. *Metall. Trans. A*, 16A:1307–1324, 1985.

[123] M. Y. NAZMY AND R. F. SINGER. High cycle fatigue and fatigue crack growth of the oxide dispersion strengthened alloy MA 754. *Metall. Trans. A*, 16A:1437–1444, 1985.

[124] G. K. DEY. Physical metallurgy of nickel aluminides. *Sadhana*, 28:247–262, February/April 2003.

[125] V. S. SINELNIKOVA, V. A. PODERGIN, AND V. I. RECHIN. *Aluminides*. Naukova Dumka, Kiev, 1965.

[126] Y. TAMARIN. *Protective Coatings for Turbine Blades*, volume 1. ASM International, September 2002.

List of Publications & Important Talks

- Ronny Mai, Advanced Realtime Software Controlling in TMF, *DVM-AK TMF*, Karlsruhe, Germany, 2006
- Ronny Mai, Temperature Controlling in TMF, *Conference of Material Science*, University of Siegen, Germany, 2007
- Volkan Kovan, Joachim Hammer, Ronny Mai, Mehmet Yüksel, Thermal-mechanical fatigue behaviour and life prediction of oxide dispersion strengthened nickel-based superalloy PM 1000, *Materials Characterization*, volume 59, 11: 1600-1606, February 2008
- Kovan Volkan, Hammer Joachim, Mai Ronny, Mehmet Yüksel, Modelling by Artificial Neural Network of High Temperature Fatigue Life of Oxide Dispersion Strengthened Nickel-Based Superalloy PM 1000, *Materials at High Temperatures*, volume 25, 2: 81-88, July 2008

A. Detailed Material Properties

A.1. Experimental Characteristics

The following tables and equations are taken from the validated code of practice [2]. Various dimensionless parameters obtained from this data are used to estimate the test boundary conditions of systematic errors, which are induced by the experimental set-up and impose the observed thermo-mechanical fatigue lifetime.

The inductional heating of the above mentioned set-up causes a skin effect with a very small direct bulk heating zone, as the ratio of the penetration depth to the specimen radius amounts to some 20 percent only, equation A.1. This error is highly influenced by the used coil design, for this work a transversal instead of a longitudinal coil was used to minimize even this deviation.

$$\frac{d}{r} = \frac{1}{\sqrt{4\pi\sigma\mu_0\mu\nu}}\frac{1}{r} \approx 20\,\% \tag{A.1}$$

Specimens are typically heated by heat conduction from the outer volume to the inside with a thermal relaxation time of $\tau \approx 2$ s, a temperature difference $\delta T \approx 10$ K between the outer zones and the inner volume occoured. The relative stress deviation coming from the radial temperature gradient induced by surface heating and following heat conduction to the inner volume can be calculated with equation A.2.

$$\frac{\Delta\sigma}{\sigma_y} = \frac{\alpha\rho c_p}{\lambda}\frac{E}{(1-\nu)\sigma_y}r^2\dot{T} \approx 7\,\% \tag{A.2}$$

These systematic errors are relatively small compared to the measurement and control uncertainties, which have to be kept as low as possible by appropriate maintenance and calibration of the complete equipment as well as by an optimization of the TMF testing techniques. The relative overall temperature deviation in the gauge length should not exceed $\pm 2.2\,\%$, equation A.3, if the rate of the relevant thermally activated process (oxidation in this case) is to be maintained within a $\pm 10\,\%$ range.

$$\frac{\Delta T}{T_{max} - T_{min}} = \pm 0.1 \frac{T_{max}^2}{T_{c,ox}(T_{max} - T_{min})} \approx \pm 2.2\,\% \tag{A.3}$$

Table A.1: Material properties of Nimonic 90, unless specified otherwise, all values refer to approximate properties at 800 °C, as listed in Special Metals data sheet [92] (`http://www.specialmetals.com`).

Property	**Symbol**	**Unit**	**Indicative value**
Mechanical properties			
Density	ρ	g/cm^3	8.2
Yield stress at T_{max}	σ_y	MPa	440 @ 850 °C
Young's modulus of elasticity at T_{max}	E	GPa	≈ 150
Poisson ratio	ν	-	0.3
Thermal properties			
Gibbs free enthalpy of plastic deformation	G_{pl}	eV	1.9
Gibbs free enthalpy of oxidation (800–1000 °C)	G_{ox}	eV	1.1
Specific heat	c_p	J/kg K	650
Thermal conductivity	λ	W/m K	24
Lin. coefficient of thermal expansion (400-850 °C)	α	10^{-6} 1/K	15
Electromagnetic properties			
Electrical conductivity	ρ	$(\mu\Omega\,\mathrm{m})^{-1}$	0.76
Magnetic permeability	μ	-	1.1
Characteristics of experimental set-up and TMF conditions			
Frequency of induction heating	υ_{ind}	kHz	120
Heating/cooling rate	$\dot{T}$	K/s	5 (10)*
Minimum temperature	T_{min}	°C	400
Maximum temperature	T_{max}	°C	850

* 5 K/s given by the draft, 10 K/s was applied for this work.

A.2. Nimonic 90

Table A.2: Derived quantities of Nimonic 90.

Quantity	Symbol	Formula	Unit	Indicative Value
Skin effect penetration depth of power density[1]	d	$\sqrt{(4\pi\sigma\mu_0\mu\upsilon)}$	mm	0.61
Characteristic temperature of plastic deformation[2]	$T_{c,pl}$	G_{pl}/k_B	°C	22000
Characteristic temperature of oxidation	$T_{c,ox}$	G_{ox}/k_B	°C	12500
Thermal relaxation time	τ	$(\frac{\rho c_p}{\lambda})r^2$	s	2.0
Radial temperature gradient	T'	$(\frac{\rho c_p}{\lambda})r\dot{T}$	K/mm	3.3
Radial stress deviation	$\Delta\sigma$	$\frac{E}{(1-\nu)}\alpha T' r$	MPa	31
Characteristic temperature deviation[3]	ΔT	$0.1T_{max}^2/T_{c,ox}$	K	10

[1] The penetration depth of the heating power density is only half the value of the penetration depth of the electromagnetic field. The vacuum permeability is calculated with $\mu_0 = 4\pi\cdot10^{-7}$ Vs/Am $\approx 1.26\cdot10^{-6}$ Vs/Am.

[2] Boltzmann constant $k_B = 1.38\cdot10^{-23}$ J/°C

[3] Represents the temperature deviation, which is associated with an acceleration/deceleration of the relevant thermally activated process by $\pm10\,\%$.

A.3. PM 1000

The following table is taken from the technical data sheets of PM 1000 and presents detailed values of physical properties [72]. The material with the number 2.4869 and the abbreviated DIN name Ni/Cr 80/20 represents typically oxide dispersoide strengthened materials.

Table A.3: Physical properties of PM 1000 at ambient temperature.

Quantity	**Unit**	**Indicative Value**
Melting point temperature	K	1681
Density	g/cm^3	8.24
Lin. coefficient of thermal expansion	10^{-6} 1/K	12.9
Young's modulus (110 textured) Young's modulus (100 textured)	GPa	210 150
Specific heat	J/kg K	440
Thermal conductivity	W/m K	12.0
Electrical Resistance	μΩm	1.00

A.4. NiAl

Table A.4: Physical properties of NiAl at ambient temperature [86, 124].

Quantity	**Unit**	**Indicative Value**
Melting Point (NiAl)	K	1955
Melting Point (β-NiAl)	K	1638
Lin. coefficient of thermal expansion	10^{-6} 1/K	13.2
Specific heat	J/kg K	640
Thermal conductivity	W/m K	76
Electrical Resistance	$\mu\Omega$m	0.08
Lattice parameter	nm	0.2887
Bonding type		Covalent/metallic
Young's modulus $\langle 100 \rangle$	GPa	100
Young's modulus $\langle 110 \rangle$		200
Young's modulus $\langle 111 \rangle$		300

All aluminising media, which form aluminides in the outer zone of the coating (60 ... 80 % of coating thickness), can be devided into high, moderate and low activities, table A.6.

Table A.5: NiAl system aluminide properties [125].

Aluminide	Cryst. structure	T_{melt}, °C	Homogen. region	Theoretical density, g/m^3	Rupture strength, MPa	Heat of formation, kJ/mol	Colour
$NiAl_3$, (ε-phase) 57.97 wt% Al	Orthorhombic a =6.611 Å b =7.367 Å c =4.812 Å	854	...	3.96	6100...7700	-38.0	...
Ni_2Al_3, (δ-phase) 40.0-44.7 wt% Al at 600...1120 °C	Rhombohedral a =4.036 Å c =4.900 Å	1132	40 − 44.7 %Al at 600...1120 °C	4.76	11200	−57.0	Violet
NiAl, (β-phase) 22.0-36.0 wt% Al at 900 °C	bcc a =2.886 Å	1638	22 − 36 %Al	5.35...6.50	5600...6200	−59.2	Blue at Al >31 % yellow at Al <31 %
Ni_3Al, (γ'-phase) 12.6-14.4 wt% Al at 20 °C	fcc a =3.589 Å	1380	12.6 − 14.4 %Al at 20 °C	7.29	4600...5600	−39.0	Pale yellow

Table A.6: Conventional classification of saturating media [82, 126].

Activity of	Aluminides forming outer coating zone	Al-concentration of the outer zone, %
High	$NiAl_3$, Ni_2Al_3	> 40 %Al
Moderate	NiAl	32-38 %Al
Low	NiAl, NiAl + Ni_3Al	< 31 %Al

B. Metallography

B.1. Overview of used etchants

Bloech and Wedl II colour etchant

For austenitic chromium-nickel steels containing high proportions of alloying elements.

Stock solution:

1 part by volume of distilled water

1 part by volume of concentrated hydrochloric acid

Etchant:

100 ml stock solution

0.1 . . . 0.2 g potassium metabisulphite

Special etchant for Nimonic, capable for SEM

Etchant:

21 ml hydrochloric acid

31 ml nitric acid

8 ml glycerine

40 ml acetic acid

Conditions:

Temperature: ≈45 °C

Time: 10 . . . 90 s

Special etchant for Ni-based superalloys and optical microscopy

Etchant:

40 ml hydrochloric acid

30 ml nitric acid

10 ml glycerine

40 ml acetic acid

Duration:

until a minute (not for preservation)

Special etchant for Ni-based superalloys, especially Hastalloy

Etchant:

50 ml distilled water

150 ml hydrochloric acid

25 g chromate (VI) oxide (toxic & carcinogenic)

40 ml acetic acid

Duration:

5 . . . 20 s

Special etchant for visualisation of slip bands and striations

This etching method based on an electrolytical etching with a current of ≈ 2 A.

Etchant:

20 g chromate (VI) oxide (toxic & carcinogenic)

1 l distilled water

Duration:

2 min

Murakami etchant

Etchant:

100 ml distilled water

10 g caustic potash

10 g potassium ferrocyanide

Duration:

30 min at room temperature

(literature: 2 . . . 30 min at roomtemperature up to 90 °C)

C. Test Rig Specifications

C.1. Thermocouple

Due to the low thermal voltage of the thermocouples, the signal has to be highly amplified and adapted for reach the desired system accuracy. It should be mentioned that every soldering point influences the thermal voltage and thus can act as a thermocouple itself. All wires and connecting points are completely shielded due to the electromagnetic field, which is induced by the induction coil's electromagnetic noise and of a significant higher magnitude than the original thermocouple signal.

Table C.1: Mostly used types of thermocouples; the range shows the absolute minimum and maximum of the thermal voltages. The marked combination was used in this test rig.

Type	**Materials**		**Temperatures**
	Positive Wire	Negative Wire	(°C)
B	Pt 30 %, Rh (Pt13Rh)	Pt 6 %, Rh (Pt6Rh)	+100 ... +1600
E	NiCr	CuNi	0 ... +800
J	NiCr	NiAl	+20 ... +700
K	Fe	CuNi	0 ... +1100
N	NiCrSi	NiSi	0 ... +1100
R	Pt 13 %, Rh (Pt13Rh)	Pt	0 ... +1600
S	*Pt 10 %, Rh (Pt10Rh)*	*Pt*	*0 ... +1550*
T	Cu	CuNi	-185 ... +300

C.2. Combination of Thermal and Mechanical System

All signal lines and their corresponding interfaces of the different components, as well as their directions are shown in figure C.1.

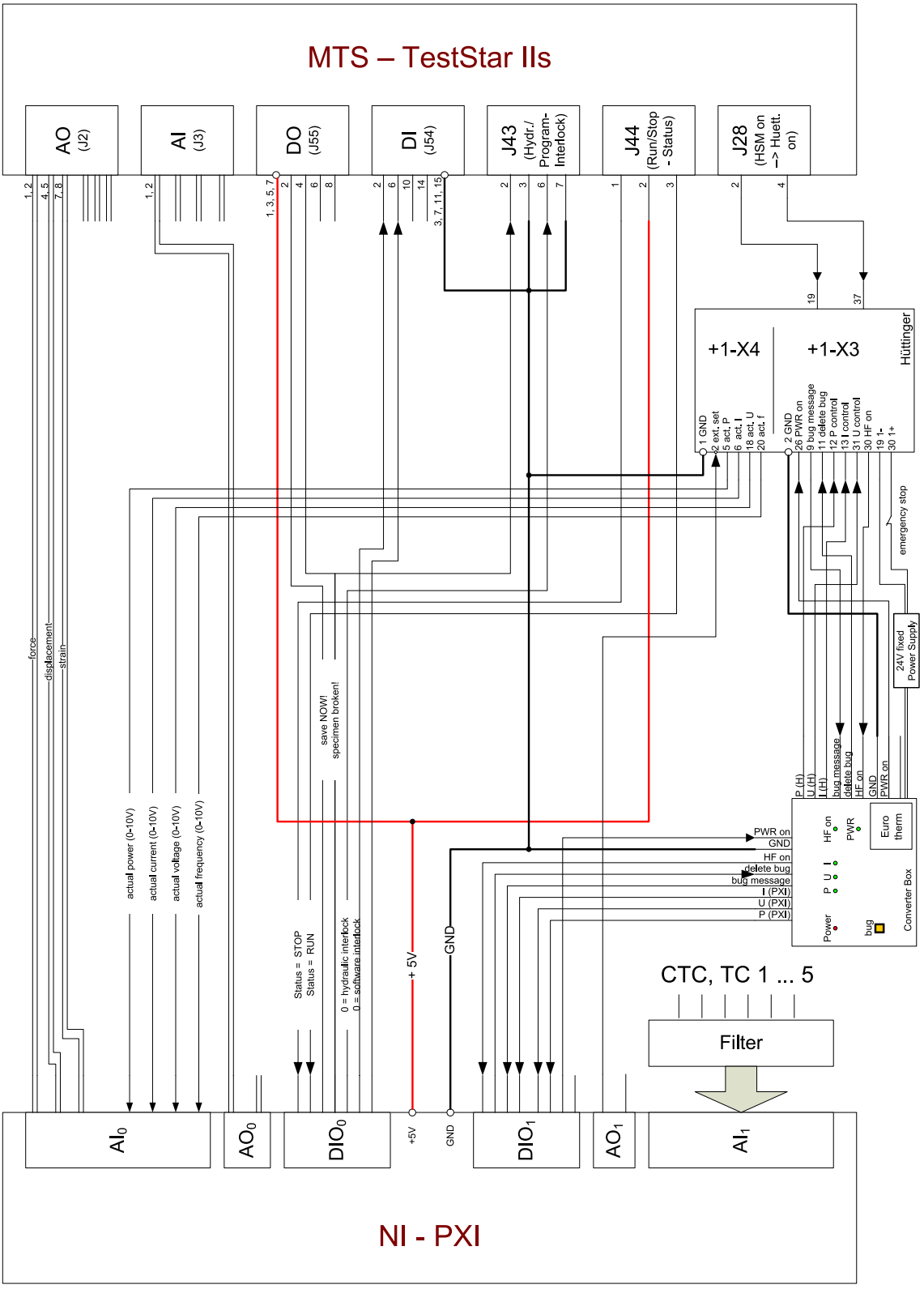

Figure C.1: Main system scheme including connected devices.